Dissertation
submitted to the
Combined Faculties for Natural Sciences and for Mathematics
of the Ruperto-Carola University of Heidelberg
for the degree of
Doctor of Natural Sciences

presented by
Diplom-Physikerin Anna Nwaada Okpara
born in Homburg(Saar), Germany

Oral examination: 19th December, 2001

Search for
Charged Higgs Bosons
at centre-of-mass Energies
of 189 - 209 GeV
at LEP

Referees: Prof. Dr. J. von Krogh
Prof. Dr. O. Nachtmann

Abstract

In dieser Arbeit wird eine Suche nach geladenen Higgs Bosonen an dem *Large Electron and Positron* Speicherring (LEP) am *CERN* präsentiert. Es wurde speziell der Zerfall des geladenen Higgs Bosons ($H^{\pm}$) in ein CP-ungerades Higgs Boson (A^0) und ein virtuelles W Boson (W^*), am *OPAL* Detektor, untersucht. In Abhängigkeit vom theoretischen Modell kann dieser Zerfallskanal sehr wichtig sein. Das A^0 Boson zerfällt in b-Quarks, während das W^* Boson in zwei Quarks oder ein Lepton und Neutrino zerfallen kann. Da geladene Higgs Bosonen am LEP Speicherring in Paaren produziert werden, kann dieser Kanal acht oder mehr Teilchenbündel im Endzustand haben. Auch ist der Zerfall eines der geladenen Higgs Bosonen in ein Tau-Lepton und sein Neutrino möglich. Dieser Kanal hat mindestens vier Teilchenbündel. Im Rahmen von Zwei-Higgs-Doublet-Modellen werden Massengrenzen als Funktion der Modellparameter, $tan\beta$, $m_{H^{\pm}}$ und m_{A^0} bestimmt. Diese Ergebnisse werden mit denen aus der Suche nach dem Zerfall eines geladenen Higgs Bosons in cs oder $\tau\nu$ kombiniert. Für $tan\beta$ =100 wird, unabhängig von m_{A^0}, eine untere Grenze von $m_{H^{\pm}}$ >60 GeV/c^2 erreicht. Die größte ausgeschlossene Higgs Masse ist 89 GeV/c^2 für $m_{A^0} \approx 45$ GeV/c^2. Des Weiteren werden die Ergebnisse der vier LEP Experimente (ALEPH, DELPHI, L3 und OPAL) kombiniert, jedoch ohne den Zerfall $H^{\pm} \rightarrow W^*A^0$. Dies ergibt eine untere Massengrenze von $m_{H^{\pm}}$ >79.8 GeV/c^2.

A search for charged Higgs bosons at the *Large Electron and Positron* Collider (LEP) at *CERN* is presented. Specifically the decay of the charged Higgs boson ($H^{\pm}$) into a CP-odd Higgs boson (A^0) and a virtual W boson (W^*) has been investigated at the *OPAL* detector. This decay channel can be very important depending on the theoretical model. The A^0 boson decays into b-quarks while the W^* boson can decay into two quarks or into a lepton and neutrino. Since charged Higgs bosons are assumed to be pair-produced at the LEP collider, the channel has at least eight jets. A decay of one of the charged Higgs bosons into a tau-lepton and its neutrino is also possible. This channel has at least four jets. Higgs boson mass limits are obtained in the context of Two-Higgs-Doublet-Models as a function of the model-parameters, $tan\beta$, $m_{H^{\pm}}$ and m_{A^0}. The results are combined with those obtained from searches in which the charged Higgs boson decays only into cs or $\tau\nu$. A lower limit of $m_{H^{\pm}}$ >60 GeV/c^2, independent of m_{A^0}, is obtained at $tan\beta$ =100. The largest excluded charged Higgs mass is 89 GeV/c^2 for $m_{A^0} \approx 45$ GeV/c^2. Furthermore, results of the charged Higgs boson search of the four LEP experiments (ALEPH, DELPHI, L3 and OPAL) are combined, excluding the decay $H^{\pm} \rightarrow W^*A^0$. A lower mass limit of $m_{H^{\pm}}$ >79.8 GeV/c^2 is thereby achieved.

Contents

Chapter 1

Introduction

Our current picture of particle physics includes four fundamental forces, the electromagnetic, the weak, the strong and the gravitational force. The gravitational force has its importance for high masses and is negligible in the mass range of particle physics. In addition to the forces and their gauge bosons the framework consists of elementary fermions, namely six quarks and six leptons grouped together in three families. The model which combines these particles and forces is called the *Standard Model* of particle physics (SM) [1]. It has been tested to a great accuracy and describes all phenomena seen in high-energy experiments today, the incorporation of finite neutrinos masses is the only change necessary due to experimental observations. Nevertheless, a particle connected to the *complex Higgs doublet field* penetrating all space and by which other particles obtain their masses through interaction, is yet to be found. In the context of this mechanism one degree of freedom remains after symmetry-breaking, giving rise to at least one neutral physical particle, the **SM Higgs boson**. Over the past years this particle has been extensively searched for.

At the e^+e^- **L**arge **E**lectron and **P**ositron (LEP) Collider at the European Laboratory for Particle Physics **CERN**, in Geneva, the four main experiments **ALEPH, DELPHI, L3** and **OPAL** have made efforts to set a combined lower bound on the mass of the neutral SM Higgs boson. Currently (September 2001), this limit is stated to be 114.1 GeV/c^2 [2].

The SM assumes the existence of only *one* doublet of complex scalar Higgs fields. The simplest extension of the SM, the Two-Higgs-Doublet-Model (2HDM), predicts two doublets of complex Higgs fields, leading to five physical Higgs bosons, three neutral Higgs ones (h^0, H^0 and A^0) and two oppositely **charged ones (H^+ and H^-)** [3]. Supersymmetric extensions of the SM predict the existence of an additional supersymmetric (SUSY) [3] partner for every particle. These models can solve certain questions open in the SM. The simplest model is the Minimal-Supersymmetric-Model (MSSM).

Although charged Higgs bosons are not allowed in the SM and are probably out of reach at LEP energies in the context of the MSSM [4], efforts have been made at LEP to search for the charged Higgs boson, which is assumed to be pair-produced at LEP energies [5]. These past analyses, however, investigate only the decay of the charged Higgs bosons to fermions because these channels are the most important ones in the MSSM. The coupling of the Higgs boson is proportional to the mass of the fermions, thus these analyses constrain the branching-ratios BR($H^\pm \to \tau\nu$) and BR($H^\pm \to c\bar{s}$) [6, 7] to fully exhaust the decay-width of the charged Higgs boson. The current LEP-combined limit is 78.6 GeV/c^2 [7], independent of the BR($H^+ \to \tau\nu$). In the context of the 2HDM's, decays of the charged Higgs boson into a virtual W boson and a CP-odd Higgs boson, A^0, are however, also possible. The W^* can decay into a pair of quarks or into a lepton plus a neutrino, while the A^0 decays into b-quarks. Many final decay states are possible with up to eight particles before fragmentation. The existence of b-quarks distinguishes these channels from the others and allows the use of tools developed especially for the search of b-quarks.

This work presents the first search for these decays. In the context of this thesis the data taken with the OPAL detector in the years 1998-2000 at centre-of-mass energies of 189-209 GeV were analysed. The results at $\sqrt{s}$ =189 GeV has been presented previously [8]. Preliminary results for the data at $\sqrt{s}$ =192-206 GeV are given in [6]. The results present the status as of September 2001.

Chapter 2

Charged Higgs Bosons

The *Standard Model* (SM) postulates one doublet of complex scalar Higgs fields with a non-zero vacuum expectation value. A physical *neutral* Higgs boson is predicted in this theory. Extensions of the SM with more than one complex scalar doublet are also plausible. In such models charged Higgs bosons are predicted. In the following an outline of the different Higgs models is given. For a more detailed review see [3, 1].

2.1 Beyond the Standard Model Higgs Theory

When constructing an extension of the Higgs sector of the SM, two main constraints have to be taken into account. The first constraint is the fact that the ρ-parameter, $\rho = \frac{m_W^2}{m_Z^2 cos^2\theta_W}$, has been found to be close to unity [9]. Any model with only doublets of complex scalar Higgs fields will satisfy this constraint automatically [3]. Secondly, there are strong experimental limits on the existence of flavour-changing-neutral-currents (FCNC's). While in the SM FCNC's are automatically absent this is not necessarily true in extended theories. An elegant theorem by Glashow and Weinberg called Natural Flavour Conservation (NFC) [10] solves the problem of FCNC's in models with more than one Higgs doublet. It states the non-existence of tree-level flavour-changing-neutral-currents mediated by Higgs bosons, if all fermions of a given electric and weak charge couple only to one Higgs doublet. The choice of couplings is constrained, but not in a unique way.

The simplest extension of the SM are models with two Higgs doublets (2HDM's). This satisfies the first constraint. There are four possibilities to satisfy the second constraint (see table 2.1). One of these is **Model I**, in which the quarks and leptons do not couple to the first Higgs doublet (ϕ_1), but couple only to the second Higgs doublet (ϕ_2). In this model the branching-ratios of the charged Higgs boson to fermions depend on fermion masses. Another possibility is **Model II** in which ϕ_1 is assumed to couple only to down-type quarks and charged leptons while ϕ_2 couples to up-type quarks and neutrinos. In this model the relative ratios of the coupling constants depend on the ratio of the vacuum expectation values of the Higgs fields and the fermion masses. Two other models are possible in which the down-type quarks and the charged leptons couple to different doublets: **Model I′** and **Model II′**.

	Model I	Model I'	Model II	Model II'
up-type quarks	ϕ_2	ϕ_2	ϕ_2	ϕ_2
down-type quarks	ϕ_2	ϕ_2	ϕ_1	ϕ_1
charged leptons	ϕ_2	ϕ_1	ϕ_1	ϕ_2

Table 2.1: *The couplings of the fermions to the two Higgs doublet fields ϕ_1 and ϕ_2 in different the models.*

2.2 Two-Higgs-Doublet-Models

In the general 2HDM model, assuming CP symmetry, the Higgs potential which spontaneously breaks $SU(2)_L \times U(1)_Y$ is given by [3]

$$\begin{aligned} V(\phi_1,\phi_2) = {} & \lambda_1(\phi_1^\dagger\phi_1 - v_1^2)^2 + \lambda_2(\phi_2^\dagger\phi_2 - v_2^2)^2 \\ & + \lambda_3[(\phi_1^\dagger\phi_1 - v_1^2) + (\phi_2^\dagger\phi_2 - v_2^2)]^2 \\ & + \lambda_4[(\phi_1^\dagger\phi_1)(\phi_2^\dagger\phi_2) - (\phi_1^\dagger\phi_2)(\phi_2^\dagger\phi_1)] \\ & + \lambda_5[Re(\phi_1^\dagger\phi_2)]^2 \\ & + \lambda_6[Im(\phi_1^\dagger\phi_2)]^2, \end{aligned} \tag{2.1}$$

where λ_i (i=1...6) are unknown real parameters and v_1 and v_2 are the vacuum expectation values of the two complex doublet scalar fields ϕ_1 and ϕ_2

$$\phi_1 = \begin{pmatrix} \phi_1^+ \\ \phi_1^0 \end{pmatrix}; \qquad \phi_2 = \begin{pmatrix} \phi_2^+ \\ \phi_2^0 \end{pmatrix}, \tag{2.2}$$

which initially give rise to four real neutral and four real charged fields. One of the neutral and two of the charged fields are absorbed to give masses to the Z^0 and the $W^\pm$, leaving five physical Higgs bosons. The mass states of the Higgs bosons are a mixture of the weak eigenstates. The physical charged Higgs bosons are given by

$$H^\pm = -\phi_1^\pm sin\beta + \phi_2^\pm cos\beta, \tag{2.3}$$

with the masses given by

$$m_{H^\pm}^2 = \lambda_4(v_1^2 + v_2^2). \tag{2.4}$$

$v_1^2 + v_2^2 \approx (246\ \mathrm{GeV}/c^2)^2$ is fixed by the m_W mass [3]. $tan\beta = v_2/v_1$ is the ratio of the vacuum expectation values of the two Higgs doublets. The imaginary and real parts of the neutral fields decouple because of the assumed CP-invariance. For the imaginary (CP-odd) sector the physical Higgs boson is denoted by A^0 and given through

$$A^0 = \sqrt{2}(-Im\phi_1^0 sin\beta + Im\phi_2^0 cos\beta), \tag{2.5}$$

with the mass given by

$$m_{A^0}^2 = \lambda_6(v_1^2 + v_2^2). \tag{2.6}$$

In addition, the real (CP-even) sector contains two physical Higgs scalars h^0 and H^0 with a mixing angle α ($m_{h^0} < m_{H^0}$ by definition)

$$\begin{aligned} h^0 &= \sqrt{2}[(Re\phi_1^0 - v_1)cos\alpha + (Re\phi_2^0 - v_2)sin\alpha)], \\ H^0 &= \sqrt{2}[-(Re\phi_1^0 - v_1)sin\alpha + (Re\phi_2^0 - v_2)cos\alpha)]. \end{aligned} \tag{2.7}$$

There is no sum rule for the masses of the charged and neutral Higgs bosons in the general 2HDM. In summary, six model parameters have to be considered: **four Higgs masses ($m_{A^0}, m_{h^0}, m_{H^0}, m_{H^\pm}$) and the two mixing angles tanβ and α** [3].

The models discussed untill now still leave some questions of the SM unsolved. Theories which extend the 2HDM's and which can solve some of these questions are based on the supersymmetric (SUSY) mechanism. The unification of the three relevant forces and their coupling constants, for example, is achieved in SUSY theories through the rise of new supersymmetric particles at a certain energy-scale [3]. The simplest one of these theories is called the Minimal-Supersymmetric-Model (MSSM) and is an extension of the 2HDM model II. Therefore the 2HDM model II has gained great attention in the past and analyses have focused on search channels favoured in this model. However, the constraint $m_{H^\pm} > 300\ GeV/c^2$ [4] exists in the 2HDM model II and the charged Higgs boson of the 2HDM model II should not be visible at LEP. This bound is imposed by precision measurements of the radiative decay $b \to s\gamma$ [11, 12], where the $H^\pm$ contributes via virtual exchange along with a top quark. Extending the 2HDM model II to the MSSM can partly compensate this effect due to contributions of new supersymmetric particles [13] and the mass limit of 300 GeV/c^2 would then be lowered. However, in the MSSM the charged Higgs boson is constrained to $m^2_{H^\pm} = m^2_W + m^2_{A^0}$ [3], at tree level. Loop corrections could lower also this mass bound but, except for an extreme choice of parameters, the $H^\pm$ of the MSSM would be out of reach at LEP. Hence, any evidence for the existence of charged Higgs bosons at LEP would most likely therefore be a sign of physics **outside** the 2HDM model II. For this reason the present investigation will focus on the 2HDM model I.

2.2.1 Production of Charged Higgs Bosons

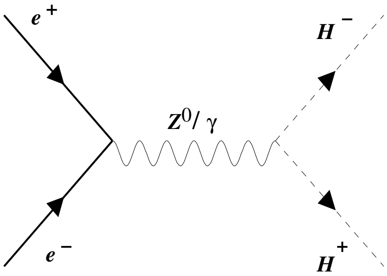

Figure 2.1: *Feynman Graph for charged Higgs boson pair-production at LEP.*

At LEP energies, the production of charged Higgs bosons in top decays, i.e. $\mathrm{e}^+\mathrm{e}^- \to (\mathrm{Z}/\gamma)^* \to t\bar{t} \to H^+H^-b\bar{b}$, in principle favoured due to the $H^\pm t\bar{t}$-coupling, is kinematically impossible. Hence, charged Higgs Bosons are assumed to be pair-produced in $\mathrm{e}^+\mathrm{e}^-$ annihilation via virtual γ^* or Z^* s-channel diagrams as shown in figure 2.1. At tree level, for a given centre-of-mass energy, the associated total cross-section depends only on the charged Higgs mass [5]

$$\sigma(\mathrm{e}^+\mathrm{e}^- \to H^+H^-) = \frac{2G_F^2 m_W^4 sin^4(\theta_W)}{3s\pi}\left(1 - \frac{2\hat{\nu}_e\hat{\nu}_H}{1-m_Z^2/s} + \hat{\nu}_H^2\frac{(\hat{\alpha}_e^2+\hat{\nu}_e^2)}{(1-m_Z^2/s)^2}]\right)\beta^3_{H^\pm} \tag{2.8}$$

where

$$\hat{\nu}_e = \frac{-1+4sin^2(\theta_W)}{4cos(\theta_W)sin(\theta_W)}; \qquad \hat{\alpha}_e = \frac{-1}{4cos(\theta_W)sin(\theta_W)}; \qquad \hat{\nu}_H = \frac{-1+2sin^2(\theta_W)}{2cos(\theta_W)sin(\theta_W)} \tag{2.9}$$

G_F being the Fermi-coupling constant, θ_W the Weinberg angle, $\sqrt{s}$ the centre-of-mass energy and m_Z (m_W) the Z^0 ($W^\pm$) mass. $\beta_{H_\pm} = \left(1 - \frac{4m^2_{H_\pm}}{s}\right)^{1/2}$ denotes the velocity of the charged Higgs boson [5].

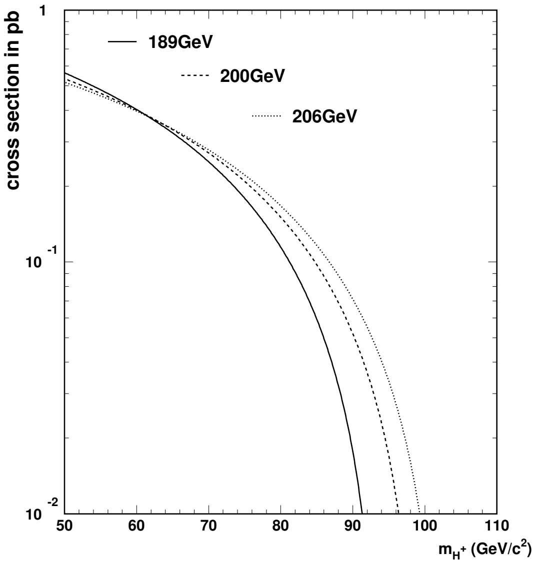

Figure 2.2: *Production cross-section of the charged Higgs boson as a function of its mass for some centre-of-mass energies of 189 GeV, 200 GeV and 206 GeV.*

The production cross-section dependency on the charged Higgs mass, for the centre-of-mass energies of 189 GeV, 200 GeV and 206 GeV, is shown in figure 2.2. The production cross-section for low Higgs masses is in the order of a few 10^{-1} picobarn but drops for higher masses due to the suppression factor $\beta^3_{H\pm}$ near the kinematical limit. Note that only the Higgs mass enters the equation of the production cross-section and no other Higgs typical characteristic.

The polar angular distribution follows a $sin(\theta)^2$ law [1], typical for a spin 0 particle pair-production (see appendix A.1 for the definition of θ)

$$\frac{d\sigma}{dcos\theta} \propto sin^2(\theta). \tag{2.10}$$

2.2.2 Decays of the Charged Higgs Boson

Direct Decays into Fermions

The charged Higgs boson can decay into a pair of fermions. The Yukawa interaction of the physical charged Higgs bosons with fermion mass eigenstates is given by [4]

$$\mathcal{L} = (2\sqrt{2}G_F)(m_{di}X\bar{u}_{Lj}V_{ji}d_{Ri} + m_{ui}Y\bar{u}_{Ri}V_{ij}d_{Lj} + m_{li}Z\bar{\nu}_{Li}e_{Ri})H^+ + h.c., \tag{2.11}$$

where G_F is the Fermi-coupling constant and u_{Lk}, u_{Rk} (d_{Lk}, d_{Rk}) denote the k-th component (k=1,2,3) of the left- and right handed up (down) type quark fields. Likewise, e_{Rk} are components of the right-handed charged lepton field. Left handed neutrino fields are denoted by ν_{Lk}. m_{dk}, m_{uk} and m_{ek} are the components of the diagonal mass matrices of down-type quarks, up-type quarks and charged leptons, respectively. H^+ denote the positively charged physical scalars. V_{kl} is the appropriate component of the CKM matrix.

	Model I	Model I'	Model II	Model II'
X	$-\cot\beta$	$-\cot\beta$	$\tan\beta$	$\tan\beta$
Y	$\cot\beta$	$\cot\beta$	$\cot\beta$	$\cot\beta$
Z	$-\cot\beta$	$\tan\beta$	$\tan\beta$	$-\cot\beta$

Table 2.2: *The values of the couplings X, Y and Z in the 2HDM's [4]*

The couplings, X, Y and Z of the fermions to the charged Higgs boson are unambiguously defined as shown in table 2.2 with $tan\beta = v_2/v_1$ and the definition of the models as shown in table 2.1.

The decay modes for the charged Higgs boson are model dependent. Since the partial decay widths of the charged Higgs boson is proportional to the squared mass of the fermions, the preferred decays are $H^+ \to t\bar{b}$ (hadronic) and $H^+ \to \tau\nu$ (leptonic). The first mode is not within the kinematic reach at LEP energies and the decay $H^+ \to c\bar{b}$ is suppressed due to the small CKM matrix element $\mid V_{cb} \mid$ [9]. This leaves $H^+ \to c\bar{s}$ as the dominant hadronic decay mode. Consequently, the dominant fermionic decay modes are $H^+ \to c\bar{s}$ and $H^+ \to \tau^+\nu$.

This leads to three direct fermionic search channels (and their charged conjugates)

1. **Direct-hadronic channel**: $c\bar{s}\bar{c}s$: $H^+ \to c\bar{s},\ H^- \to \bar{c}s$
2. **Direct-semi-leptonic-channel**: $c\bar{s}\tau\nu$: $H^+ \to c\bar{s},\ H^- \to \tau\nu$
3. **Direct-leptonic channel**: $\tau\nu\tau\nu$: $H^+ \to \tau\nu,\ H^- \to \tau\nu$

The calculation of the decay width of the direct fermionic decays, at tree level, is straightforward [14]

$$\Gamma(H^\pm \to \tau\nu) = \frac{G_F m_\tau^2 m_{H^\pm} \mid Z \mid^2}{4\pi\sqrt{2}}, \tag{2.12}$$

$$\Gamma(H^\pm \to cs) = \frac{3 G_F m_s^2 m_{H^\pm} \mid V_{cs} \mid^2 \mid X \mid^2}{4\pi\sqrt{2}} + \frac{3 G_F m_c^2 m_{H^\pm} \mid V_{cs} \mid^2 \mid Y \mid^2}{4\pi\sqrt{2}}. \tag{2.13}$$

m_τ being the tau-lepton mass and m_c (m_s) the mass of the c-quark (s-quark). $\mid V_{cs} \mid$ is the CKM matrix coefficient for the decay of the c to s quark. The other variables have been defined before. The masses of the quarks are evaluated at the scale $m_{H^\pm}$.

W^*-mediated Decays

Besides the direct decays of the charged Higgs into fermions, bosonic decays are also possible. In the 2HDM model I the charged Higgs boson decouples from fermions at high values of $tan\beta$ (see equation 2.3 and table 2.2) and bosonic decays will be very important in this limit. The bosonic decays $H^\pm \to W^\pm\gamma$ or $H^\pm \to W^\pm Z^0$ are forbidden at tree-level due to CP-conservation [3]. If kinematically allowed, the charged Higgs boson will decay into a $W^\pm$ boson and a CP-odd A^0 or the lightest CP-even h^0 boson. The W boson will be virtual at LEP. Figure 2.3 illustrates the W^*-mediated decays.

- $H^\pm \to A^0 W^* \to A^0 f\bar{f}'$
- $H^\pm \to h W^* \to h f\bar{f}'$

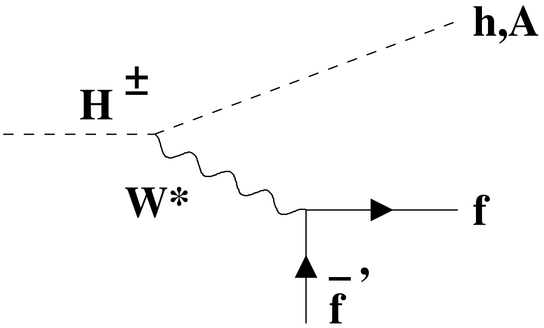

Figure 2.3: *The W^*-mediated decays of the charged Higgs bosons.*

The partial widths of the W^*-mediated decay channels are given by [15]

$$\Gamma(H^{\pm} \to hW^* \to hf\bar{f}') = \frac{9G_F^2 m_W^4}{16\pi^3} cos^2(\beta - \alpha) m_{H^{\pm}} G_{hW}, \tag{2.14}$$

$$\Gamma(H^{\pm} \to A^0 W^* \to A^0 f\bar{f}') = \frac{9G_F^2 m_W^4}{16\pi^3} m_{H^{\pm}} G_{AW}, \tag{2.15}$$

where the functions G_{hW} and G_{AW} are only dependent on the masses of the particles in the decay [4]. The other variables have been defined before. At LEP, the decay of the charged Higgs boson into a virtual W and h^0 is only possible for small h^0 masses. Such small h^0 masses should have been visible at LEP for reasonable choices of α and β, and independent of the choice of couplings, but no evidence for a small h^0 mass has been found [2, 16]. This leaves the decay into a W^* and A^0 boson to be the preferred one. Note that the decay width of $H^{\pm} \to W^* A^0$ is independent of $tan\beta$ and α, as shown in equation 2.15.

Figure 2.4(a) shows the branching-ratios of the charged Higgs into the different decay modes for 2HDM model I for fixed mass values [17]. The branching-ratio $BR(H^{\pm} \to W^* A^0)$ approaches unity in the 2HDM model I for large values of $tan\beta$. The relative values of $m_{H^{\pm}}$ and m_{A^0} will determine how far off-shell the virtual vector boson will be. The dependency on m_{A^0} is illustrated in figure 2.4(b).

The possible search channels depend also on the decay modes of the A^0 boson. The coupling-strength of the A^0 boson to the fermions can be determined with a reinterpretation of table 2.2. X here denotes the coupling-strength of the A^0 boson to down-type quarks, Y the coupling to up-type quarks and Z the coupling to charged leptons. Focusing on the 2HDM model I the couplings of A^0 to fermions are all proportional to $cot\beta$. Other decays of the A^0, like the decay into two gluons and two photons are mediated by fermion loops. Their couplings are therefore also proportional to $cot\beta$. There is a slight dependency on the A^0 mass since the partial width of the decay to fermions scales as $\Gamma \propto m_f^2 m_{A^0}$ while the gluon decay width scales as $\Gamma \propto m_{A^0}^3 \alpha(m_{A^0})^2$ [18]. Bosonic decays of the A^0 into two W or Z^0 bosons are not allowed [3]. Decays involving a h^0 boson are only possible for a very small h^0 mass which is not preferred from LEP data [2, 16]. This leaves the fermionic decays to be the only possible ones and thus the branching-ratios of the A^0 are essentially independent of $tan\beta$ because of the same $cot\beta$ factor in their decay widths. Therefore, the dominant decay modes of the A^0 will be $b\bar{b}$ ($t\bar{t}$ is kinematically not reachable) [18].

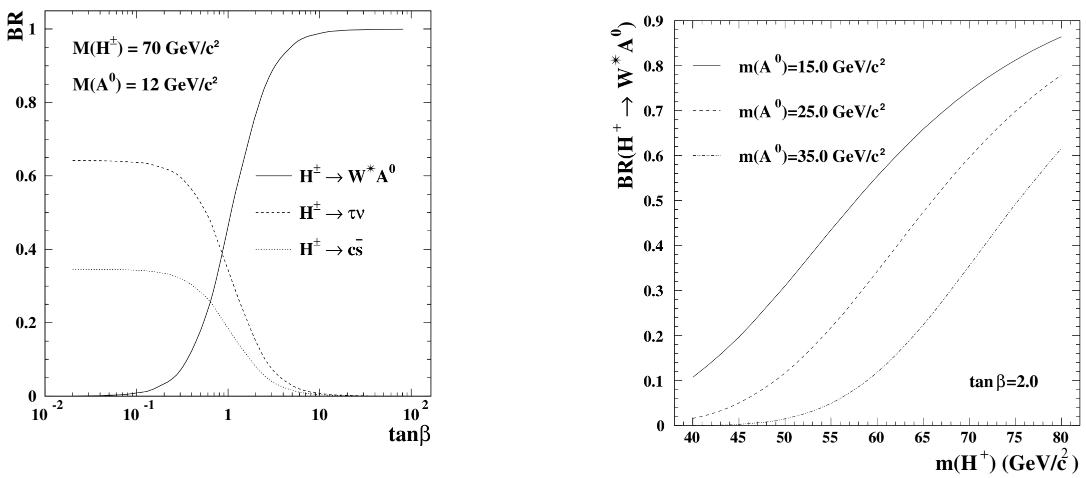

Figure 2.4: *(a) The branching-ratios of the charged Higgs boson in the 2HDM model I as a function of* $\tan\beta$ *for fixed Higgs masses.(b) The branching-ratio of the charged Higgs decay to* W^*A^0 *in the 2HDM model I as a function of the charged Higgs mass (in GeV/*c^2*) for a fixed value of* $\tan\beta$ *[17].*

Search Channels in the Context of the 2HDM Model I

Combining the direct fermionic and W^* mediated decay states one can get as much as 20 different search channels for the charged Higgs boson. Only six of these contribute in the 2HDM model I with more than 10% in any region of parameter space, above the $A^0 \to b\bar{b}$ ($\approx$ 12 GeV/c^2) threshold [17] and for $m_{H^\pm}$ >40 GeV/c^2. Constraints for new Z^0-decay modes from the Z^0-width impose the model-independent mass limit of $m_{H^\pm}$ >40 GeV/c^2 [4]. In total, we have the following direct fermionic search channels (+c.c.)

- **Direct-hadronic channel**: $c\bar{s}\bar{c}s$: $H^+ \to c\bar{s},\ H^- \to \bar{c}s$,
- **Direct-semi-leptonic-channel**: $c\bar{s}\tau\nu$: $H^+ \to c\bar{s},\ H^- \to \tau\nu$,
- **Direct-leptonic channel**: $\tau\nu\tau\nu$: $H^+ \to \tau\nu,\ H^- \to \tau\nu$,

and the following W^*-mediated search channels (+c.c.)

- **W^*-mediated hadronic channel:**
  $q\bar{q}'b\bar{b}q''\bar{q}'''b\bar{b}$: $H^+ \to q\bar{q}'A^0,\ H^- \to q''\bar{q}'''A^0,\ A^0 \to b\bar{b}$,
- **W^*-mediated leptonic channel**:
  $\ell\nu b\bar{b}q\bar{q}'b\bar{b}$: $H^+ \to \ell\nu A^0,\ H^- \to q\bar{q}'A^0,\ A^0 \to b\bar{b}$.

Furthermore, there is a mixed channel in which one charged Higgs boson decays directly into fermions while the other decay is W^*-mediated (+c.c.)

- **W^*-mediated tau channel**:
  $\tau\nu q\bar{q}'b\bar{b}$: $H^+ \to \tau\nu,\ H^- \to q\bar{q}'A^0,\ A^0 \to b\bar{b}$.

Chapter 3

The Experimental Apparatus

3.1 The LEP Collider

The European Laboratory for Particle Physics *CERN*, Geneva, Switzerland was founded in 1954. In the year 1989 the *Large Electron and Positron Collider* (LEP) was put into operation. It had a circumference of about 27 km, passing the Swiss-French border several times 100 meters beneath the ground. There are four distinct interaction points at which particle detectors (ALEPH, DELPHI, L3 and OPAL) were placed to collect the data obtained in e^+e^- collisions.

3.2 Data Sets

At the start, LEP was operated at a centre-of-mass energy of 91 GeV, the mass of the Z^0-boson. Up to the end of 1995 a total luminosity of about 175 pb^{-1} (4.5 million Z^0 decays) per experiment was collected, allowing a high precision measurement of the SM. Since 1996 an upgrade of LEP (*LEP2*) allowed a continuous increase in centre-of-mass energy up to 209 GeV in the end of 2000. The higher energies allowed the production of W-boson and Z-boson pairs. The direct search for Higgs bosons and new particles was also possible over a wider mass range. The LEP ring and its experiments were finally closed at the end of 2000. This work includes all data sets taken in the years 1998-2000. Table 3.1 shows the luminosities collected by the OPAL experiment at the different centre-of-mass energies, as used in the following analyses with the required detectors fully operational.

$\sqrt{s}$ (GeV)	int. lumi. (pb^{-1})	Year
189	175.0	1998
192	28.9	1999
196	74.8	
200	77.2	
202	36.1	
206	211.1	2000

Table 3.1: *Luminosities taken by the OPAL experiment. Although the highest centre-of-mass energy reached in the year 2000 was about 209 GeV, the data sample is denoted with 206 GeV sample throughout this work, since the luminosity-weighted mean energy was 206.1 GeV.*

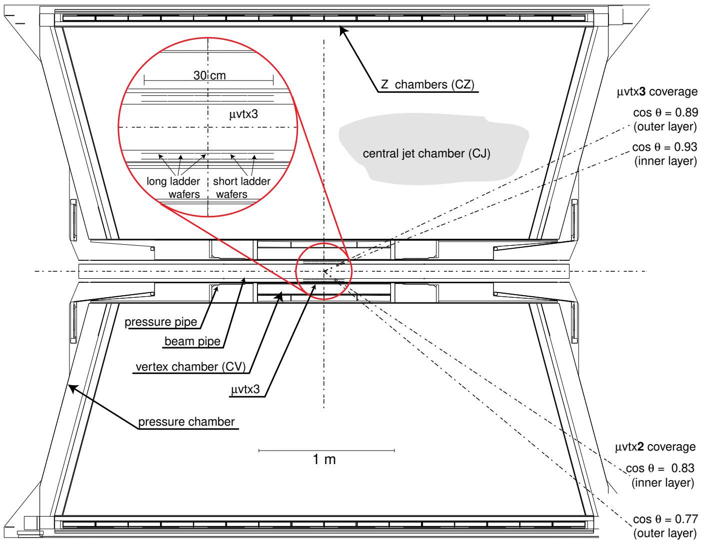

Figure 3.1: *The sub-detectors of the OPAL tracking detector [20].*

3.3 The OPAL Detector

The *Omni-Purpose Apparatus at LEP* (OPAL) detector was built with well proven technologies of its time. It is a multipurpose apparatus designed to reconstruct and identify all types of e^+e^- final states. It is a cylinder-symmetrical 4π detector, 12 m long with a diameter of 10 m. The +z direction of the right-handed coordinate system is defined by the flight direction of the electrons, the +x direction points to the centre of the ring and the point of origin falls together with the center of the detector. The azimuth angle ϕ is defined with regard to the horizontal +x-direction and the polar angle θ with regard to the +z-direction. Figure 3.2 shows an exploded view of the OPAL detector. In the following the detector is shortly explained. A more detailed review is given in [19].

The central tracking detector of the OPAL detector is a high precision tracking device reconstructing tracks from collisions at the interaction point. It is located inside a solenoid supplying a uniform axial magnetic field along the z-axis of 0.435 T. As shown in figure 3.1, the central tracking detector is build-up of the beam pipe at a radius of 5.35 cm and consists, in radially increasing order, of:

- The **Silicon Microvertex Detector** (SI) was originally installed in OPAL in 1991 and underwent several upgrades between 1993 to 1996. It is made up of two barrels of double-layered single-sided micro-strip detectors covering a polar angle of $|cos(\theta)| < 0.89$ with both layers. It reaches a high spatial resolution of 18 μm in the $r-\phi$ direction and 24 μm in the $r-z$ direction [20], important for the reconstruction of secondary vertices.

- The **Vertex Detector** (CV) is a cylindrical jet chamber. It has a length of 100 cm and a radius of 23.5 cm consisting of two layers of 36 sectors each. The inner layer contains the axial sectors each having a plane of 12 sense wires parallel to the beam direction. In the outer layer the stereo sectors contain a plane of 6 sense wires each. The axial cells reach a resolution of 50 μm, in the $r-\phi$ plane. A coarse measurement of the z coordinate, 700 μm, based on the time difference between signals at either side of the sense wires is achieved.

- The **Jet Chamber** (CJ) is a cylindrical drift chamber, with a length of 400 cm and divided into 24 identical sectors. In the $r-\phi$ plane the coordinates of the wire hits are determined from a drift time measurement while the z coordinate is measured using a charge division technique and summing over the charges revived at the end of each wire. The overall spatial resolution for the jet chamber in the $r-\phi$ plane is 135 μm and 6 cm in z direction.

- The **z-Chambers** (CZ) measure the z-coordinate of tracks leaving the barrel region of the jet chamber. They consist of a layer of 24 drift chambers 400 cm long. They cover 94% of the azimuthal angle and have a polar angle range $|cos\theta| < 0.72$. The spatial resolution of the chamber is typically between 100 μm and 350 μm in the z direction and 15 mm in the $r-\phi$ plane.

After the central tracking detector the next sub-detectors that follow are

- The **Time-of-Flight Counters** (TOF). The barrel time-of-flight (TB) system provides trigger signals and charged particle identification in the mass range of 0.6-2.5 GeV/c^2. Moreover, it rejects effectively cosmic rays covering the barrel region with $|cos(\theta)| < 0.82$. It consists of scintillation counters forming a barrel layer. In 1996 the Tile Endcap (TE) was added to increase the trigger information available from the forward region [21].

The electromagnetic calorimeter identifies and detects electrons, positrons and photons and measures their deposited energy. It has an acceptance for electrons and photons of almost 99% of the solid angle and consists of

- The **Presampler**. The barrel electromagnetic presampler (PB) covers a polar angle range of $|cos(\theta)| < 0.81$. It consists of 16 chambers, each made up of two layers of limited streamer drift tubes with anode wires running axially. The endcap electromagnetic presampler (PE) is a multi-wire proportional counter. It has a polar angle range of $0.83 < |cos(\theta)| < 0.95$. Both presamplers are located just before the electromagnetic calorimeter and are used to identify pre-showering of particles before the calorimeter.

- The **Electromagnetic Calorimeter** is divided into a barrel part (EB) and the endcap part (EE). The barrel part consists of 9440 lead glass blocks with a radiation length (X_0) of 24.6 each. It has a coverage in the polar angle of $|cos(\theta)| < 0.81$. The endcap consists of 1132 lead glass blocks of about 22 X_0 and covers the full azimuthal angle and $0.81 < |cos(\theta)| < 0.98$. The electromagnetic calorimeter achieves a spatial resolution of 2-5 mm, together with the presamplers. The Cerenkov-light of the showering particles in the calorimeter, used for the energy-measurement, is read out by phototubes at the base of each block. A cluster is then defined as a combination of neighbouring blocks in which the energy deposition is observed. The barrel region has a resolution of

  $$\sigma_E/E = 0.2\% + 6.3\%/\sqrt{E/GeV}. \qquad (3.1)$$

  The resolution of the endcap region is

  $$\sigma_E/E = 5\%/\sqrt{E/GeV}. \qquad (3.2)$$

- The **Hadronic Calorimeter** measures the energy of the hadrons in an event and, essentially, allows only muons to pass into the muon detectors. It is divided into three parts, the barrel part (HB), the endcap part (HE) and the pole-tips (HP) and is made up of alternately iron and limited streamer tubes for the barrel and endcaps and multi-wire proportional chambers for the pole-tips. The hadron calorimeter provides at least 4 interaction lengths of iron absorber for particles emerging from the electromagnetic calorimeter. The resolution of the hadron calorimeter is $120\%/\sqrt{E(GeV)}$ for all parts and nearly all hadrons are absorbed in it.

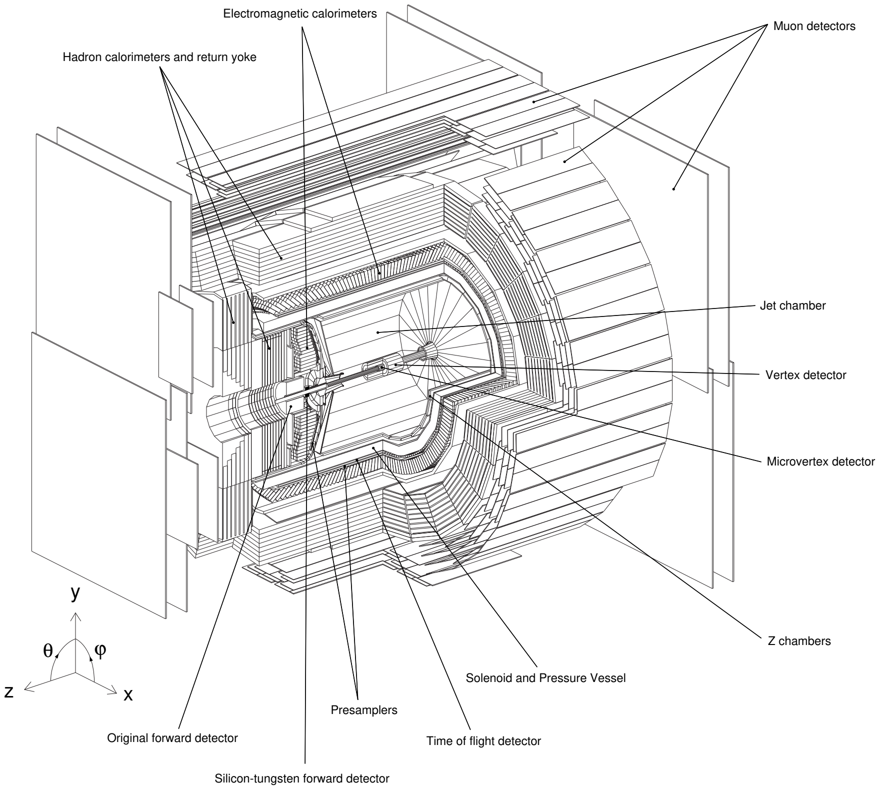

Figure 3.2: *The OPAL detector and its sub-detectors.*

- The **Muon Chambers** separate hadrons from muons which were able to pass the hadron calorimeter. It consists of a barrel (MB) and an endcap part (ME). The barrel part consists of drift chambers and the endcaps are made up of limited streamer tubes. The amount of material, particles have to pass, exceeds 1.3 m of iron equivalent. A spatial resolution of 1.5 mm in ϕ and 2 mm in z is reached in the barrel part.

In addition, a system of different detectors near the beam pipe detects particles which scatter at low angle and therefore cannot be seen by the other previously described detectors:

- The **Forward Detectors** (FD) are positioned in the endcap region and consist of proportional tube chambers and sampling layers of lead-scintillator sandwich calorimeters.
- The **Gamma Catcher** (GC) is a ring of lead scintillator sandwich sections of 7 radiation length thickness.
- The **Silicon Tungsten Luminometer** (SW) is a sampling calorimeter constructed to detect low angle Bhabha scattering events and is used to measure the luminosity at OPAL. It is build-up of layers of silicon detectors and layers of tungsten and was added in 1993 [22].
- The **MIP-Plug** (MIP: Minimum Ionising Particle) (MIP-Plug) was added in 1997 [21] and covers a region of 43-200 mrad. It consists of a system of scintillating tiles detecting minimally ionising particles especially muons.

Chapter 4

The Event Simulation

The strategy in the search for new particles is to select, from experimental data, those events which have a high probability of containing new particles and to reject those with a low probability. Events containing new particles (*signal events*) are simulated as well as the expected SM events originating from processes without new physics (*background events*).

The energy/momentum four-vectors of the corresponding partons are produced by event generators and the quarks of the events undergo fragmentation/hadronisation leading to colour-neutral particles. The OPAL detector is simulated with the GOPAL processor [23], which is based on the general GEANT package [24]. The correct simulation of the detector is based on the geometry and the characteristics of the different sub-detector components. The passage of the particles through the detector, their decay in the detector and the interaction with the material, e.g. ionization of the gas in the tracking chambers or showering in the calorimeters are taken into account. Experimental resolution effects of the energy, momentum and tracks measurements, based on the detector geometry and characteristics are also considered. The ROPE package then reconstructs events from digital information produced by the GOPAL package[1].

4.1 Event Generators

- **PYTHIA** [25] is a multi purpose event generator. A number of physics aspects, like $e^+e^- \to f\bar{f}$, with final state parton showers, fragmentation and decay, are included in the event generator. The string fragmentation is used in the PYTHIA package for the hadronisation. It was originally divided into the JETSET and the PYTHIA packages. As of 1996 both packages were combined to PYTHIA.

- **HERWIG** [26] is a general purpose event generator, which includes the simulation of lepton-lepton scattering. The parton shower approach is used for final state QCD radiation, including colour coherence effects and azimuthal correlations both within and between jets (particle bundles). It uses the cluster model for the hadronisation.

- **GRC4F** [27] is the standard four-fermion event generator. It is based on the GRACE package [28], an automatic Feynman diagram computation system. Fermion masses are non-zero and helicity information can be traced down to the final particles. The hadronisation is performed through the string mechanism as implemented in PYTHIA.

- **EXCALIBUR** [29] computes all four-fermion processes in e^+e^-annihilation and is used as an alternative four-fermion event generator for systematic cross-checks. QED initial state corrections and QCD contributions are included. Fermions are taken to

---

[1] The ROPE package is also used to reconstruct events based on digital information in experimental data from the OPAL detector.

be massless. In the scope of this work the fragmentation and hadronisation was done with PYTHIA.

- **KK2F** [30] simulates the two-fermion processes, $e^+e^- \to f\bar{f}n\gamma$. Photon emissions are calculated within the Coherent Exclusived Exponentiation (CEEX) [31]. Final state hadronisation is done with PYTHIA.
- **PHOJET** [32] is used to simulate hadronic photon-photon interactions in the framework of the two-component Dual Parton Model.
- **KORALZ** [33] is an event generator for lepton and quark pair production. Complete $\mathcal{O}(\alpha)$ QED corrections are included in the leptonic channels.
- **VERMASEREN** [34] is the standard generator for $e^+e^- \to e^+e^-f\bar{f}$ events in $\gamma\gamma$ collisions.
- **HZHA** [35] is an event-generator which simulates Higgs production and decay processes for various models. The fragmentation is done via PYTHIA.

4.2 Simulation of the Signal

The number of possible search channels based on the the W^*-mediated decay of the charged Higgs bosons have been discussed in chapter 2. The possible decays of the charged Higgs boson in the channels are shown in figures 4.1 and 4.2.

In the signal events of the hadronic channel, both W^* bosons decay into a pair of quarks (left diagram of figure 4.1). The events are characterised by eight quarks of which four are b-flavoured and a high multiplicity.

The leptonic decay of *one* of the W^* is shown in the right diagram of figure 4.1. The signal events of the leptonic channel are characterised by six quarks, of which four are b-flavoured, and a lepton plus a neutrino (missing energy).

One charged Higgs boson decays directly into a tau-lepton and a tau-neutrino in the signal events of the tau channel, as shown in figure 4.2, while the other decays according to the left diagram in figure 4.1. The events are characterised by a tau-lepton, energy missing due to the associated neutrino of the tau-lepton, four quarks, of which two are b-flavoured and a lower multiplicity than in the other two search channels.

The signal events were generated using HZHA with version 2.7. The events were generated for the centre-of-mass energies of 189 GeV, 192 GeV, 196 GeV, 200 GeV and 202 GeV, which corresponds to the energies of the data sets for the years 1998-1999 (see table 3.1). In the year 2000, the centre-of-mass energies ranged from 200 GeV to 209 GeV, with a

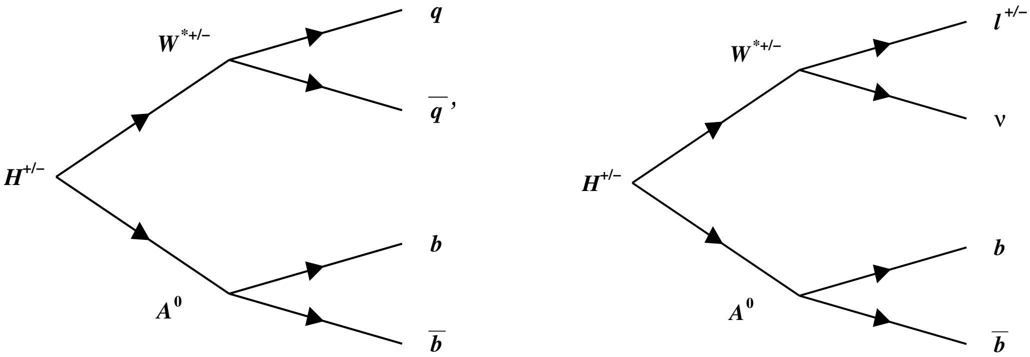

Figure 4.1: *Feynman diagrams for the W^* mediated decay of the charged Higgs boson. Left: The W^* decays into a quark pair, right: the W^* decays into a lepton and neutrino. The A^0 boson decays into a b-quark pair in both cases.*

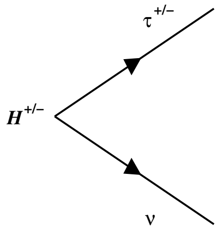

Figure 4.2: *Feynman diagram for the decay* $H^{\pm} \to \tau\nu$.

luminosity-weighted mean energy of 206.1 GeV. For the analyses based on this data set, the signal events were generated for the centre-of-mass energy of 206 GeV.

The characteristics of the signal events, like kinematics and angular distributions, depend on both masses $m_{H^{\pm}}$ and m_{A^0}. Hence, the signal events were generated for various masses with a mass range of $40\,\mathrm{GeV/c^2} \leq m_{H^{\pm}} \lessapprox \frac{\sqrt{s}}{2}$ (in 5 GeV/c^2 steps) and $12\,\mathrm{GeV/c^2} \leq m_{A^0} \leq m_{H^{\pm}} - 5$ GeV/c^2 (with three to five mass points per $m_{H^{\pm}}$). The lower limit is defined by a model-independent bound from constraints on visible decays of new particles contributing to the Z^0 width [4] and the $A^0 \to b\bar{b}$ threshold respectively [17]. $m_{H^{\pm}}$ reaches its maximum if the charged Higgs bosons are produced at rest. For the upper limit, the maximum $m_{H^{\pm}} = \sqrt{s}/2$, was reduced by a few GeV/c^2 in order not to hit the kinematical boundary. Likewise, an upper limit of $m_{A^0} = m_{H^{\pm}} - 5$ GeV/c^2 was chosen. The number of mass points varies from about 30 at $\sqrt{s}$ =189 GeV to about 50 at $\sqrt{s}$ =206 GeV. 500 events[2] were generated, per search channel and mass point ($m_{H^{\pm}}$;m_{A^0}).

Figure 4.3 shows a simulated hadronic signal event at $\sqrt{s}$ =189 GeV with $m_{H^{\pm}}$ =40 GeV/c^2 and m_{A^0} =12 GeV/c^2, as simulated in the OPAL detector. The multi-hadronic structure of the event is visible.

---

[2] All number of events quoted in the following denote the number of events available after ROPE.

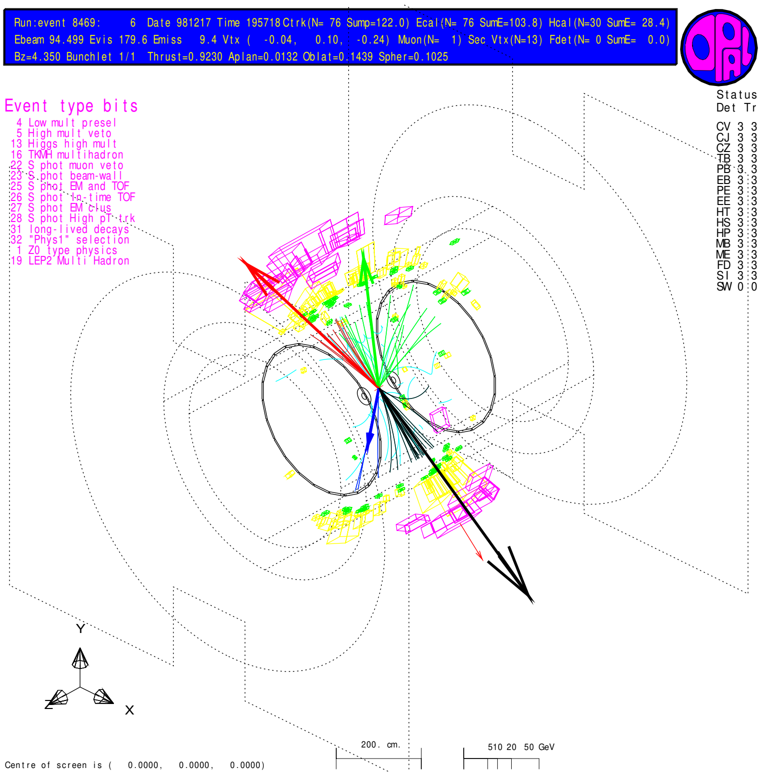

Figure 4.3: *The event-display of the decay of a hadronic event at 189 GeV for* $m_{H^\pm}$ *=40 GeV/*c^2 *and* m_{A^0} *=12 GeV/*c^2 *as simulated in the OPAL detector. The four arrows indicate the jets if the event is forced into a four jet state using the Durham algorithm. The size of the three-dimensional light (dark) open grey boxes represent the deposited energy of the associated track in the electromagnetic (hadron) calorimeter.*

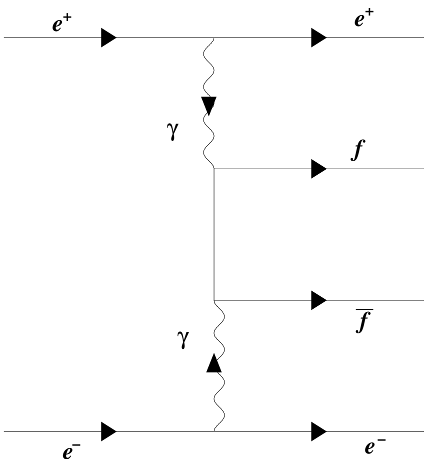

Figure 4.4: *The Feynman diagram for the two-photon background events.*

4.3 Simulation of the Background

The background events originating from SM processes are split up accordingly to two-photon events, two-fermion events and four-fermion events[3].

Two-Photon Processes

Two photons, originating from the electron and the positron, are exchanged in a t-channel diagram to produce two fermions (figure 4.4). The primary electron and positron are scattered under small angles, escaping mostly along the beam-pipe. A sizeable amount of missing energy, a small multiplicity and two fermions is therefore characteristic for these events.

The $e^+e^- \rightarrow e^+e^- hadrons$ final states were generated with PYTHIA, PHOJET and HERWIG. The VERMASEREN generator was used for all $e^+e^- \rightarrow e^+e^-\ell^+\ell^-$ final states. PYTHIA and HERWIG were used for the fragmentation. The number of produced events ranges from 10^3-10^6, depending on the final state. This corresponds to about 0.5-85 times the data luminosity.

Two-Fermion Processes

Two-fermion events originate from the annihilation of the electron and positron into a virtual Z^0 boson or a γ, decaying into a fermion anti-fermion pair. Gluon radiation in the final state is possible, leading to a multi-jet event, (left diagram in figure 4.5). A photon can also be radiated in the initial state (*initial state radiation; ISR*), (right diagram of figure 4.5). The photon then typically enters the beam pipe and remains undetected.

The generators PYTHIA and KK2f were used for the production of the four-vectors in the quark-pair sample for $\sqrt{s}$ =189 GeV and $\sqrt{s}$ =192-206 GeV, respectively. KORALZ and KK2F were used for the lepton pair generation for $\sqrt{s}$ =189 GeV and $\sqrt{s}$ =192-206 GeV, respectively. The fragmentation was done with PYTHIA. Alternatively HERWIG was used for two-fermion generation, for systematic checks. Typically, 250×10^3 - 500×10^3 of quark-pairs and 50×10^3 - 100×10^3 of lepton-pairs were generated. This corresponds to about 15-90 and 50-215 times the data luminosity for the quark-pairs and the lepton-pairs, respectively.

---

[3] The standard OPAL generator choice is used for the background samples.

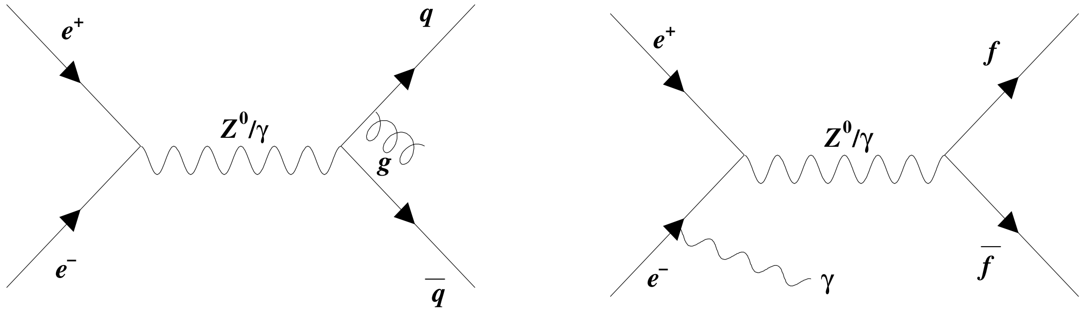

Figure 4.5: *The annihilation of the electron and the positron two-fermion final state. The left diagram shows gluon radiation in the final state. The right one shows initial state radiation.*

Four-Fermion Processes

Four-fermion events are classified as those SM events containing four fermions in the final state, other than those originating from two-photon events. The processes mainly contain pair-produced W or Z^0 bosons as illustrated in figure 4.6. There can be additional gluon radiation leading to high multiplicity events.

The event-generator GRC4F was used for the generation of the partons' four-vectors. The fragmentation was done with PYTHIA. The generator EXCALIBUR was alternatively used for systematic cross-checks. The four-fermion background events were typically generated with $20{\times}10^3$ - $200{\times}10^3$ events per final state. This corresponds to about 25-170 times the data luminosity.

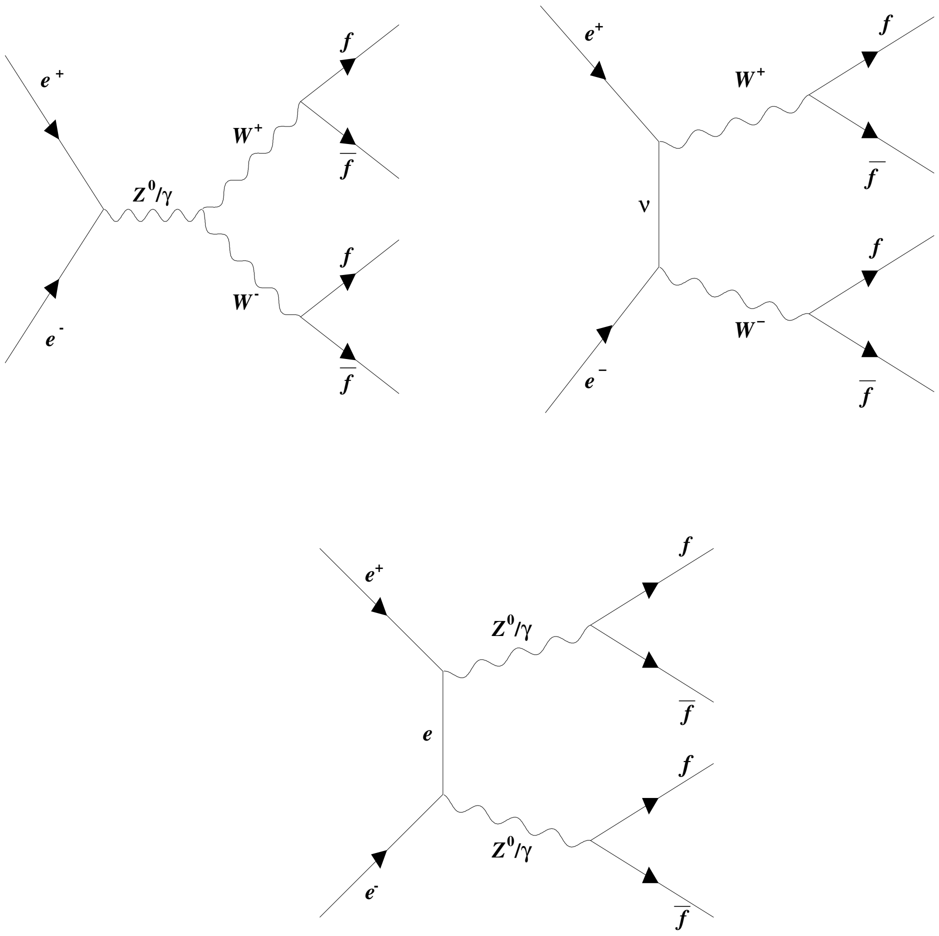

Figure 4.6: *Some Feynman diagrams of important SM four fermion processes. Top row: W pair production. Bottom row: Z^0 pair production.*

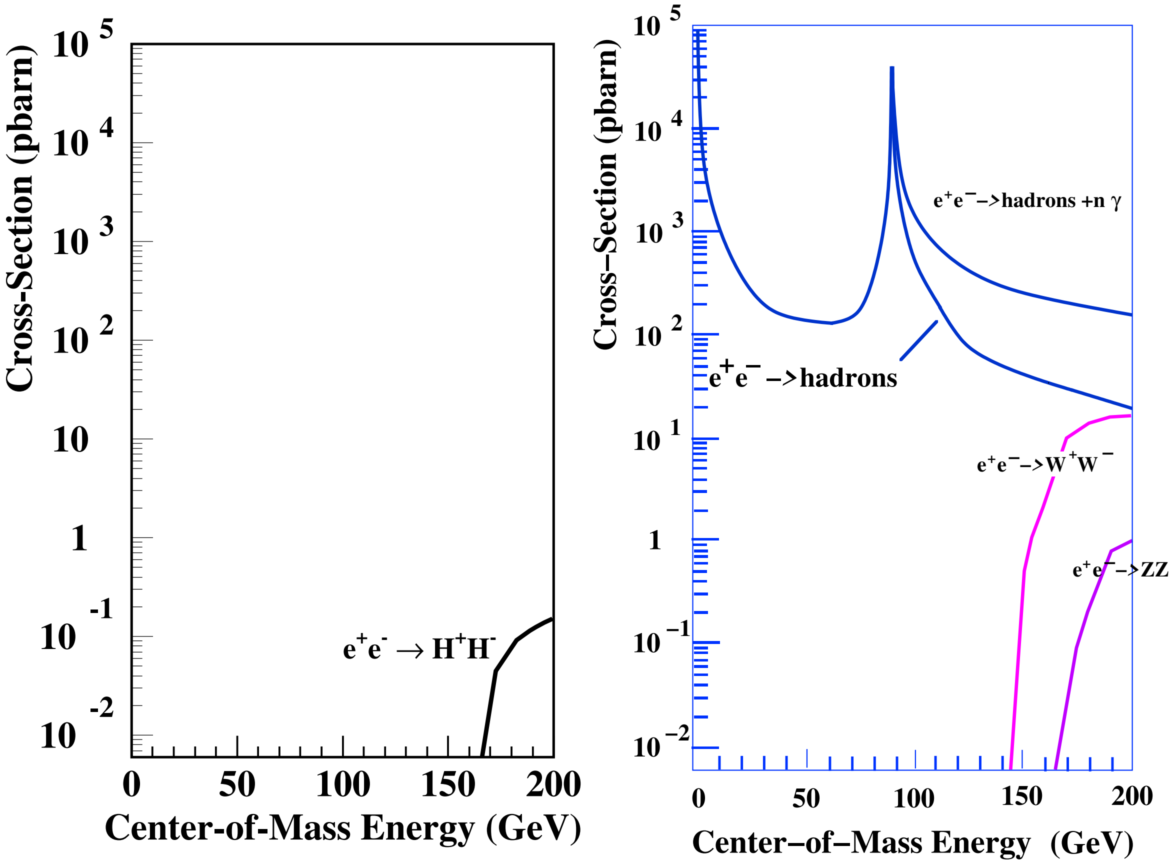

Figure 4.7: *The cross-section against the centre-of-mass energy for; Left diagram: Pair-produced charged Higgs bosons with* $m_{H^\pm}$ *=80 GeV/*c^2*. Right diagram: Typical SM processes.*

4.4 Event Properties

4.4.1 Signal Properties

The signal events originating from the W^*-mediated channels are characterised by a high probability of containing b-hadrons, many jets and a high multiplicity. Hence, b-tagging methods are used to enhance the signal events.

The signal events in the hadronic channel should furthermore obey energy and momentum conservation before fragmentation and those of both the hadronic and leptonic channel tend to be spherical. Kinematic fits and event-shape variables exploit this fact. The signal events of the leptonic channel should have a certain amount of energy missing due to the neutrino of the W^*-decay. Although the events contain a lepton and a neutrino they resembles the signal events of the hadronic channel a lot because of their high multiplicity and high number of b-hadrons. Therefore, no direct tagging of the lepton was made, but rather variables sensitive to the energy missing in the event were used. The tau channel is characterised by a tau-lepton and missing energy due to the associated neutrino of the tau-lepton. The tau-lepton is tagged in the events. This channel also has a lower multiplicity than the other two search channels.

4.4.2 Background Properties

The production of the different background processes have been discussed in section 4.3. The production cross-section of the charged Higgs bosons is only in the order of 10^{-1} picobarn, as illustrated in the left diagram of figure 4.7, while the background events can have cross-sections in the order of a few 10^4 picobarn, as shown in the right diagram of figure 4.7. Thus, in order to be sensitive to the signal, the background events have to be suppressed.

- The two-photon processes, $\mathrm{e}^+\mathrm{e}^- \to \mathrm{e}^+\mathrm{e}^- f\bar{f}$, are characterised by missing energy, a small multiplicity and two fermions, which can lead to jets, if the fermions are quarks. Although, they have a high cross-section (in the order of 10 pb above $\sqrt{s}$ =100 GeV), they can be easily suppressed by simple cuts on the energy and multiplicity and do not pose an important background source.

- The two-fermion processes resulting in a lepton-pair, $\mathrm{e}^+\mathrm{e}^- \to \ell^+\ell^-$, can be easily suppressed due to the lack of quarks in the final state. The hadronic decays $\mathrm{e}^+\mathrm{e}^- \to q\bar{q}$ can undergo gluon radiation leading to a relative high multiplicity. Initial state radiation can also occur. These events then tend to have an effective centre-of-mass energy close to the Z^0-mass. As illustrated in the right diagram of figure 4.7, these events have high cross-sections. A cut on the effective centre-of-mass energy of 100 GeV or higher and the demand for a multi-jet structure, effectively suppresses this two-fermion background sample. Furthermore, the use of b-tagging tools helps to suppress the two-fermion background, by exploiting the high number of b-hadrons in the signal, and the low branching-ratio of 3.07×10^{-3} for $g \to b\bar{b}$ [36] and the relative low branching-ratio of about 15% for $Z^0 \to b\bar{b}$ [9].

- The four-fermion processes ($\mathrm{e}^+\mathrm{e}^- \to f\bar{f}f\bar{f}$) containing pair-produced W or Z^0 bosons are problematic and difficult to suppress. They resemble those events containing pair-produced charged Higgs bosons in structure and kinematics. Additional gluon radiation can furthermore simulate multi-jet events. The use of b-tagging tools helps to suppress events arising from W-pair-production because the branching-ratio of $W \to b + X$ is small at LEP2 energies. Events containing a Z^0-pair present an irreducible background type.

Chapter 5

Variables and Methods used in the Selection of Events

The variables used in the selections need energy and momentum information of the charged and neutral particles of an event. Some variables are based on flavour-identification methods or on information from bundle of particles (jets) in an event. In some cases, kinematic fits are applied, based on energy and momentum conservation. Ultimately, the final selection is based on a likelihood-method which uses different variables as input depending on the search channel. The variables and methods used are discussed in the following.

5.1 Reconstruction Methods

5.1.1 Measurement of Energy and Momentum

The energy and momentum information of the charged and neutral particles in an event is needed for the selection. In case of the charged particles, this information is derived from momentum-measurement in the tracking chamber using particle identification methods. For the neutral particles, on the other hand, the information can only be derived from the calorimeter system. Since charged particles also contribute to the energy deposition in a calorimeter cluster, one has a double-counting of energy. A matching algorithm, implemented in the *MT package* [37], corrects this over-counting. The measured energy of a cluster in the calorimeter is reduced by the sum of energies of charged particles pointing to it. The cluster is then called *a neutral cluster*. If the energy is smaller than a cut-off value, the cluster is discarded and only the track information is used in the event. If the remaining energy of the neutral cluster is higher than a cut-off value, the cluster is kept assuming a photon-hypothesis. Neutral clusters without associated tracks are considered photons. The energy and momentum information of photons is derived by the energy and angular information of the associated cluster.

5.1.2 Jet Reconstruction

The charged tracks and neutral clusters[1] of an event are then grouped together to *jets* using the DURHAM [38, 39, 40, 41] algorithm. It is based on a transverse momentum minimisation algorithm. It starts by calculating for every pair of final-state objects(k,l) the scaled transverse momentum of the less energetic particle compared to the more energetic one, defined as

$$Y_{kl} = \frac{2 * min(E_k^2, E_l^2)(1 - cos(\theta_{kl}))}{E_{vis}^2}, \tag{5.1}$$

---

[1] Charged tracks and neutral clusters are often also referred to as particles in the following.

where θ_{kl} is the angle between the momentum vectors of the two particles, E_k and E_l are the energies of the two particles and E_{vis} is the total energy of all final state particles.

The two particles (i,j) with the smallest Y_{ij} value are combined to form a new *pseudo-particle* with a 4-momentum $p_{ij} = p_i + p_j$. Then Y_{kl} is again calculated for all particles and pseudo-particles. This procedure is repeated until all pairs of objects satisfy $Y_{kl} > Y_{cut}$, where Y_{cut} is a predefined cut-value. The objects remaining at this stage are called jets. Instead of choosing a certain Y_{cut} on can also chose a number of n jets to be reached. In this case the procedure is repeated until the number of required jets is reached. The Y_{cut} value at which an event classification changes from an n-jet event to an (n+1)-jet event is called $Y_{n,n+1}$. In this work the logarithm, $log_{10}Y_{ij}$ was used as selection variable because it shows good distinguishing power between the signal and background.

5.1.3 Kinematic Fits

Kinematic fits are used to exploit all kinematic information in an event. In the hadronic and leptonic search channels, the events are forced to four jets and hypotheses are formed based on event kinematics, e.g. the amount of missing energy or momentum conservation. This hypotheses lead to *constraints* imposed on the event. The measured jet momenta are adjusted within their errors to fulfil these constraints. Minimising

$$\chi^2 = \sum_i (\vec{p_i} - \vec{p_i}')^t V^{-1}(\vec{p_i})(\vec{p_i} - \vec{p_i}') \tag{5.2}$$

while considering the constraints leads to the best corrected values for the corrected jet momenta, $\vec{p_i}'$. $V^{-1}(\vec{p_i})$ is the covariance-matrix of the measured jet momenta. The parametrisation of the momenta is done in $1/|\vec{p}|$, θ and ϕ because their errors are considered uncorrelated (see [42] for the exact parametrisation). The minimisation of χ^2 is done with an iterative gradient-method which incorporates the constraints through Lagrange-factors [43]. The value of the minimised χ^2 is an indication for the goodness of the hypothesis. A χ^2 probability, $P_{\chi^2}(N_{DOF})$, is then defined [43]. It is distributed uniformly between 0 and 1 for those events which fulfil the hypothesis. Events not fulfilling the hypothesis accumulate at small values. $P_{\chi^2}(N_{DOF})$ is therefore a good discriminator between signal and background events with constraints based on the characteristics of the signal. Hypotheses used in this work are

- A **four constraint kinematic fit** requiring energy and momentum conservation. An event, after being forced into four jets ($e^+e^- \rightarrow j_1j_2j_3j_4$) should fulfil four constraints (**4C-fit**):

  $$\sum_i^4 E_i = \sqrt{s}; \quad \sum_i^4 \vec{p_i} = \vec{0}, \tag{5.3}$$

  where i runs over the number of jets.

- A **five constraint kinematic fit**. In addition to the energy and momentum conservation one can require that, in a four-jet event ($e^+e^- \rightarrow j_1j_2j_3j_4$) the invariant mass of two jets equals the invariant mass of the other two jets. There are three possibilities to form two pair of jets (j_1j_2;j_3j_4), (j_1j_3;j_2j_4), (j_1j_4;j_2j_3). The one with the highest $P_{\chi^2}(N_{DOF})$ is chosen as the correct pairing. (**5C-fit**).

5.1.4 Identification of Leptons

The electrons and muons of the event are not directly tagged for. However the missing energy of their associated neutrinos is exploited in the selections. An artificial neural network (ANN) [44, 45, 46] is used to identify tau candidates from charged Higgs decays. The algorithm is based on track information, and distinguishes tracks from tau-decays from those of the hadronic system, by exploiting the higher momenta and relative isolation of the tau-leptons compared to fake ones [44]. Tau-leptons with an ANN-output greater than 0.5 are considered possible candidates. If more than one candidate exists per event, the candidate with the highest ANN-output is selected. It is then removed to investigate the remaining hadronic system (*rest-of-the-event*) which is forced into two jets.

5.1.5 Identification of b-Flavour

A b-tagging algorithm is used to distinguish between signal from background events. It is based on three independent identification algorithms [46, 47, 48, 49, 50].

- *Lifetime ANN:* b-Hadrons have a long lifetime (about 10^{-12} s), a high decay multiplicity and a high mass. Exploiting this, a lifetime tag based on an artificial neural network is formed using quantities calculated from the tracks and clusters of the jet.
- *Jet-Kinematics ANN:* The jet shape for b-flavoured jets is more spherical than for lighter flavoured jets, due to the large decay multiplicity and higher mass of the b-flavoured hadrons. Three variables are used for the jet shape tag: 1) the number of energy-flow objects around the central part of the jet, 2) the angle between the jet axis and the boosted sphericity and 3) the C-parameter for the jet boosted back to its rest frame[2].
- *High p_t lepton tag:* The semi-leptonic decays of the b-quarks are identified by lepton tagging. The transverse momentum p_t of the lepton, calculated with respect to the direction of a sub-jet in which the lepton track is included is used as a b-tag variable (see [46, 47, 48, 49]).

The lifetime ANN, the jet-kinematics ANN and the high-p_t lepton tag are combined with an unbinned likelihood as described in [46]. A combined $\mathcal{B}$ output is then computed per jet:

$$B_i = \frac{w_b}{w_b + w_c \cdot f^i_{c/b} + w_{uds} \cdot f^i_{uds/b}}, \tag{5.4}$$

w_i are weight factors, taking into account the different background compositions for the different search channels. The sensitivity however does not depend strongly on the choice of these weight factors [46]. For every jet, $f^i_{q/b}$ is the ratio of the jet probability to be q=c,uds flavoured, with respect to its probability of being b flavoured and derived from the combination of the lifetime ANN, the jet-kinematic ANN and the high-p_t lepton tag [46]. Equation 5.4 can be rewritten as

$$B_i = \frac{1}{1 + \alpha \cdot f^i_{c/b} + \beta \cdot f^i_{uds/b}}, \tag{5.5}$$

where α and β are free parameters and can be fitted to the analyses based on efficiency and purity requirements.

Figure 5.1 shows the b-tagging performance for calibration data taken at $\sqrt{s} = m_Z$ in the year 2000 (a–b) and at $\sqrt{s}$ between 200–209 GeV in the year 2000 (c–d). A comparison of the $\mathcal{B}_{jet}$ variable in data to expected background is shown in the left diagrams. The

---

[2] see section 5.2 for the definition of sphericity and C-parameter

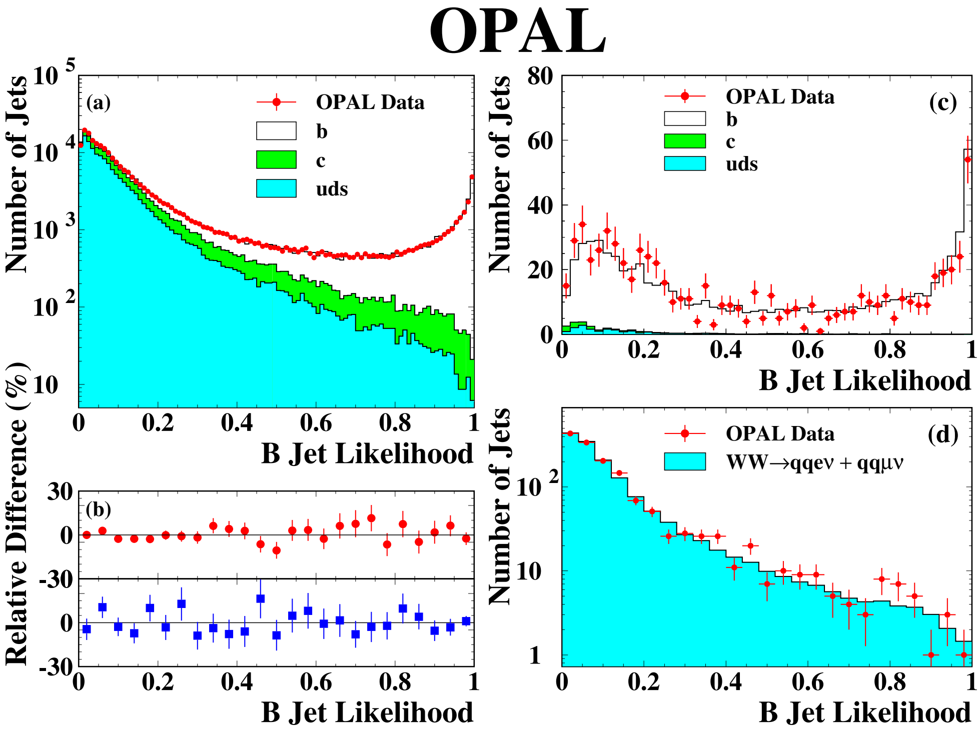

Figure 5.1: *The b-tagging performance and modelling for (a–b) calibration data taken at* $\sqrt{s} = m_{\mathrm{Z}}$ *in 2000, and (c–d) at* $\sqrt{s}$ *between 200–209 GeV in 2000. (a) The distribution of the b-tagging variable* $\mathcal{B}$ *for jets in data compared to the Monte Carlo expectation. (b) The bin-by-bin difference between data and Monte Carlo simulation for jets opposite non b-tagged jets (circles) and for jets opposite b-tagged jets (squares). (c) The b-tagging output,* $\mathcal{B}$*, for jets opposite b-tagged jets in a sample of* $\mathrm{q\bar{q}}\gamma$ *events, and (d) for jets in a sample of* $\mathrm{W^+W^-} \to \mathrm{q\bar{q}e^-}\overline{\nu}_{\mathrm{e}}$ *and* $\mathrm{W^+W^-} \to \mathrm{q\bar{q}}\mu^-\overline{\nu}_\mu$ *events (and charge conjugates). The histogram in (d) shows the distribution from the four-fermion Monte Carlo sample [50].*

tagging efficiency of b-flavoured (udsc-flavoured) jets is modelled by the background within an accuracy of 2%(5%) [50]. The performance of the b-tagging for $qq\gamma$ events is checked in the upper right diagram of figure 5.1. The lower right diagram shows the performance for tagging udsc flavours in the four fermion sample. Good agreement between data and background can be seen.

5.2 Variables

In the following, different variables used in the analysis are described.

- **Multi-hadronic event character:** An event is selected as a multi-hadronic event if it passes requirements based on track and cluster information. These are listed in appendix A.3. This suppresses mainly the two-photon background events.

The following variables are used, based on the energy and momentum information seen in the detector. Some are sensitive on a photon escaping along the beam pipe therefore suppressing the two-fermion and two-photon background.

- The effective centre-of-mass energy, $\sqrt{\mathbf{s}'}$, of the e^-e^+ collision after initial state photon radiation. This variable is used to suppress radiative background processes such as $e^+e^- \rightarrow (Z^0/\gamma)^* \rightarrow q\bar{q}\gamma$ in which a photon is radiated in the initial state and the event is left with energy close to the Z^0 mass. The calculation of $\sqrt{s'}$ is as follows: The photon is directly searched for in the electromagnetic calorimeter. The biggest electromagnetic cluster, which does not have a track assigned to it, is assumed to be the photon from initial state radiation with the energy E_γ. Another alternative procedure is used by performing a kinematic fit to a system of jets with a constraint on energy and momentum conservation considering an unmeasured photon along the beam direction [51]. The photon energy E_γ, is then the larger of the two energies derived by the two methods. $s' = s - 2E_\gamma\sqrt{s}$ is the effective centre-of-mass energy.
- $\mathbf{E_{vis}}/\sqrt{\mathbf{s}}$ and $\mathbf{E_{miss}}/\sqrt{\mathbf{s}}$. The visible and missing energy scaled by $\sqrt{s}$, where the visible energy is the sum over the energies of all particles in an event. The missing energy is defined as $\sqrt{s} - E_{vis}$.
- The energy deposited in the forward detectors, $\mathbf{E_{forward}}$.
- $|\cos\theta(\mathbf{P_{miss}})|$, of the missing momentum, where $|\cos\theta(P_{miss})| = |P^z_{miss}/P_{miss}|$ with $\vec{P}_{miss} = -\sum\vec{p}_i$. The sum runs over all particles in an event and p_i is the momentum of the particle i.
- The transverse momentum of the event, $\mathbf{P_{transverse}}$, with respect to the direction of the beam.

5.2.1 Event Shape Variables

Variables exploiting the differences in the event shapes for signal and background:

- The **C-parameter**:

$$C = 3(e_1e_2 + e_2e_3 + e_3e_1), \tag{5.6}$$

  where e_1, e_2, and e_3 are the eigenvalues of the normalised momentum tensor [52, 53] of the event. C is a measure of the *circularity* of the event which ranges from 0 for back to back jets to 1 for spherical events.

- The **sphericity**, S:

$$S = 3/2 \min_{|\vec{n}|=1} (\sum_i \vec{p}_{iT}{}^2 / \sum_i \vec{p}_i{}^2). \tag{5.7}$$

  The sum goes over all particles. $\vec{p}_i$ is the momentum of particle i. $\vec{p}_{iT}$ is the transverse momentum of particle i relative to a unit vector $\vec{n}$. The vector $\vec{n}$ is varied in space until the minimum of S is obtained. The sphericity is about 0 for a two-jet event and about 1 for an isotropic event.

- The **oblateness**, O:

$$O = T_{major} - T_{minor}. \tag{5.8}$$

T_{major} and T_{minor} are values defined with respect to the quantity *thrust*

$$T = \max_{|\vec{n}|=1} \frac{\sum_i |\vec{n} \cdot \vec{p_i}|}{\sum_i |\vec{p_i}|}. \tag{5.9}$$

The sum goes over all particles. The vector $\vec{n}$ is varied in space until the maximum of $\vec{T}$ is achieved and defines its direction. $\vec{p_i}$ are the momenta of the particles. $\vec{T}_{major}$ satisfies equation 5.9 and in addition lies in the plane perpendicular to the thrust-axis. $\vec{T}_{minor}$ also satisfies equation 5.9 and is perpendicular to both the $\vec{T}$- and $\vec{T}_{major}$-axis. The oblateness is about 0 for an event symmetrical around the thrust axis and high for a planar event.

5.2.2 Variables based on Flavour Identification

In the tau search channel the tau-lepton from the charged Higgs boson is tagged and the remaining hadronic event is defined as the rest-of-the event after the tau-lepton has been removed.

- The output of an artificial neural network is used to identify tau candidates. The number of candidates is used as a selection variable, $\mathbf{N^{\tau}_{ANN}}$.
- The momentum of the tau-lepton, $\mathbf{P}_{\tau}$.
- A variable, $\mathcal{B}_{\mathbf{evt}}$, based on the b-flavour of an event is applied, as described in section 5.1.5

$$\mathcal{B}_{\mathbf{evt}} = \frac{1}{1 + \alpha \prod_i^N f^i_{c/b} + \beta \prod_i^N f^i_{uds/b}}. \tag{5.10}$$

The product runs over the number of jets in an event. This variable approaches unity for events with b-quarks. Events containing jets with a low probability to contain b-quarks and high probability to contain c or uds-quarks, have a low $\mathcal{B}_{evt}$. In the hadronic and leptonic search channel the events are forced to four jets to obtain this variable. In the tau search channel, the rest of the event after removal of the tau-lepton is forced into two jets. The factors α and β were chosen to maximise the signal to background discriminating power of $\mathcal{B}_{evt}$, similar to [54]. $\alpha = 0.1$ and $\beta = 0.7$ was chosen for the hadronic and leptonic search channel and $\alpha = \beta = 1.0$ for the tau search channel. Although, the b-tagging algorithm was optimised for jets containing only one b-quark the correct modelling of the signal events, which can have more than one b-quark per jet, is assumed.

5.2.3 Jet Variables

The following jet resolution parameters are used:

- The logarithm of the jet resolution parameters where the number of resolved jets changes from i to j, $\mathbf{log_{10}(Y_{ij})}$. A number of logarithm of the different jet resolution parameters are used in the analyses. These variables are partly correlated but still contain different information.

In the hadronic and leptonic analyses the events are forced to four jets. In the tau analyses the events are forced to two jets after the removal of the tau-lepton with the highest ANN output. For each jet following variables are then calculated.

- The number of charged tracks of the jet with the lowest multiplicity, $\mathbf{N_{jet}^{ch}}$. Signal events tend to have a high charged track multiplicity per jet. In the tau channel this variable is calculated for the hadronic system, after τ removal.

For the hadronic and leptonic search channel.

- The maximum jet energy, $\mathbf{E_{jet}^{max}}$, after forcing the event to four jets. This discriminates against two-fermion events since in these events one expects two high-energetic jets.
- The maximum opening angle of the sub-jet containing 68% of the jet's total energy, among the reconstructed four jets, $\mathbf{max(cos\theta_{jet}^{68\%})}$. In an multi-jet event which has been forced to four jets, this opening angle which contains 68% of the jet's total energy is bigger because the tracks are more spread in space. For four-fermion events and two-fermion events the opening angle is smaller.

For the tau search channel.

- In the hadronic system after the tau-lepton is removed, the cosine of the angle between the two jets, $\mathbf{cos(q\bar{q} - angle)}$.
- The cosine of the angle between the tau-lepton and the nearest jet, **cos(τ-to-nearest-jet angle)**
- The polar angle of the rest-of-the-event after the tau-lepton has been removed, multiplied by the opposite tau charge[3], $\mathbf{-Q_\tau cos\theta(P_{rest})}$. This angular distribution is forward peaked for W decays but is transversely peaked for scalar particles like the charged Higgs boson.

5.2.4 Kinematic Fit Variables

Furthermore, some variables based on the kinematic fit information are used:

- The product of the di-jet charge and the cosine of the di-jet decay angle is calculated, $Q_{dijet} \cdot cos\theta_{dijet}$, for the jet pairing in the four jet assumption $(j_i j_j; j_k j_l)$, which gives the best five constraint fit[4]. This quantity, **W decay angle**, discriminates between scalar Higgs decays and vector boson (W) decays.
- The **rest-of-event mass** after the tau-lepton is removed. A 1C fit is performed asking for $e^+e^- \to j_1 j_2 \tau\nu$ processes. The mass of the rest-of-event system is the mean of the fitted masses of the two jets, if the fit probability is greater than 10^{-5}. If the fit probability is smaller than 10^{-5} the rest-of-event mass is calculated simply through the masses of the two forced jets, of the hadronic system, after tau removal and the beam energy.

---

[3] Opposite denotes -Q_τ. The charged is defined by the tracks associated to the tau-lepton in the ANN.

[4] For more than one charged track per jet, the jet–charge is calculated as $\Sigma q^{(i)} p_{\mathrm{L}}^{(i)0.5} / \Sigma p_{\mathrm{L}}^{(i)0.5}$. The sum goes over each track within the jet, $q^{(i)}$ is the track charge and $p_{\mathrm{L}}^{(i)}$ is the track momentum parallel to the jet direction. The charge of the di–jet system with the larger sum of the two individual jet charges is set to +1, and the charge of the other di–jet system is set to −1.

5.3 The Likelihood-Method

The simplest way to select data events that are signal-like from the observed data is a cut-based method. Cuts are applied in variables which differ for signal and background. The data events that have passed all the required cuts remain. The drawback of this is that events which might be signal-like in many variables might be thrown away, simply because they do not pass one *single* variable's cut. The solution would be to give each event a probability of being signal-like taking into consideration *all* selection variables. The two most common methods used in high-energy physics today are artificial neural networks [55] and likelihood methods [56]. In this work a likelihood method was used for the final selection which is applied after a cut-based preselection distinguishing very roughly between signal and background.

Considering N_{class} different event classes each originating from a different physics process with N_{var} selection variables for each event. The normalised distribution for an event from the class j to have the value x_i is $f_i^j(x_i)$. The probability for this event to belong to one of the event-classes j, for the discriminating variable x_i, is then given by

$$p_i^j(x_i) = \frac{f_i^j(x_i)}{\sum_{k=1}^{N_{class}} f_i^k(x_i)}. \tag{5.11}$$

With the selection variables written as a vector $\overrightarrow{x} = (x_1, x_2, ...)$, the likelihood for the event to belong to the event class j is given by

$$P^j(\overrightarrow{x}) = \frac{\prod_{i=1}^{N_{var}} p_i^j(x_i)}{\sum_{k=1}^{N_{class}} \prod_{i=1}^{N_{var}} p_i^k(x_i)}. \tag{5.12}$$

$P^j(\overrightarrow{x})$ is the joint likelihood for an event to belong to class j. Its value lies between 0 and 1. Events which pass a certain cut value P_{cut}^j pass the final selection. This cut was optimised for the analyses using the *PC package* [57, 58]. This package used for studying and optimising likelihood sections at OPAL, aiming at good signal efficiency for the signal event sample and good background reduction. Note that the assumed probability interpretation no longer holds if there are correlations between the selection variables. But $P^j(\overrightarrow{x})$ still discriminates between the different classes.

The correlations between two variables x and y can be described by a correlation coefficient defined as

$$\rho = \frac{cov(x,y)}{\sigma_x \sigma_y}, \tag{5.13}$$

where the covariance cov(x,y) is given by

$$\begin{aligned} cov(x,y) &= \frac{1}{N}\sum_i (x_i - \overline{x})(y_i - \overline{y}), \\ &= \overline{(x-\overline{x})(y-\overline{y})}, \\ &= \overline{xy} - \overline{y}\,\overline{x}. \end{aligned} \tag{5.14}$$

The covariance cov(x,y) is greater than zero, if values of x, which are greater than $\overline{x}$, tend to occur together with values of y which are also greater $\overline{y}$. Likewise if large x value are correlated with small y values the covariance is negative. cov(x,y) should be zero, if there is no connection between the behaviour of the x values and the y values. In order to be independent of the dimensions the covariance is divided by the standard deviation on x and on y to obtain the correlation coefficient.

Chapter 6

The Hadronic Search Channel

The W^*-mediated **hadronic** channel, $\mathrm{e^+e^-} \to \mathrm{H^+H^-} \to W^{*+}A^0W^{*-}A^0 \to q\bar{q}'\mathrm{b\bar{b}}q''\bar{q}'''\mathrm{b\bar{b}}$, is the first and the most important channel, considering the branching ratios in the 2HDM model I. It is characterised by both charged Higgs bosons decaying into a virtual W boson which in turn decays into a pair of quarks, and an A^0 boson which decays into two b-quarks. The A^0 boson is constrained to be lighter than the charged Higgs boson and it has to be heavier than a pair of b-quarks. The W boson, being virtual, is not constrained to the mass of a real W boson. The outstanding features of this channel are eight quarks in the event, leading to eight jets in the final state. The correct resolution into eight jets is difficult due to fluctuations in the fragmentation process and due to ambiguities in the jet assignment and is beyond the scope of this analysis. Therefore, for the calculation of the jet variables the event is forced into four jets making no assumption about the particle assignment of the jets.

In summary, the hadronic channel is characterised by having a high multiplicity, many jets and a high b-probability. Although the event shape of the hadronic channel depends on the mass of the A^0 boson, no optimisation of the search as a function of m_{A^0} is carried out. Instead, the search at $\sqrt{s}$ =189 GeV is done for two regions in $m_{H^\pm}$, a low and a high-mass-region. For the data at 192-206 GeV, on the other hand, only one analysis is retained focusing on the parameter space that was not already excluded with the $\sqrt{s}$ =189 GeV analysis. First, the analysis at $\sqrt{s}$ =189 GeV is presented, then the combined analyses for 192-202 GeV (192, 196, 200 and 202 GeV; data taken in the year 1999) and 206 GeV (which corresponds to the centre-of-mass energy at which the MC (Monte-Carlo) events were generated; the data was taken in the year 2000 and energy range was 200-209 GeV).

6.1 The Search at $\sqrt{s}$ =189 GeV

A cut-based preselection is done considering outstanding differences in signal and background. Then a likelihood selection is applied to the events passing the preselection, based on more subtle differences in the selected variables between signal and background events.

6.1.1 The Preselection

The following variables are used in the hadronic event preselection (see chapter 5 for the definition of the variables).

1. The event has to meet the requirement of a multi-hadronic event. This mainly suppresses the two-photon background sample.

2. $\sqrt{s'} > 155\ GeV$, which reduces the two-fermion background.

3. $log_{10}(Y_{34}) > -3.0$ requires a multi-jet event.

Hadronic Channel $\sqrt{s}$ =189 GeV						
Cut	Data	Total bkg.	2-fermi.	4-fermi.	2-photon	Signal Eff. (%) $m_{\mathrm{H}} = 60$ GeV/c^2 $m_{\mathrm{A}} = 30$ GeV/c^2
(1)	18815	18518.8	15005.5	3259.8	253.5	100.0
(2)	6134	6202.2	4276.3	1907.4	18.5	97.2
(3)	3446	3360.2	1686.0	1661.0	13.2	97.2
(4)	2339	2218.4	942.7	1268.3	7.4	97.2
(5)	2158	2045.1	880.2	1162.0	2.9	97.2
(6)	1947	1835.7	718.3	1115.2	2.2	87.4
(7)	1811	1720.4	606.8	1111.4	2.2	87.4
(8)	**238**	**211.6**	116.7	94.9	0.0	**73.6**

Table 6.1: *The number of data and Monte Carlo events at each stage of the preselection for the hadronic channel at a centre-of-mass energy of 189 GeV, and the efficiency for the hadronic signal events with* $m_{H^+} = 60$ *GeV/*c^2 *and* $m_{A^0} = 30$ *GeV/*c^2*.*

4. Likewise $log_{10}(Y_{45}) > -3.2$.

5. A four constraint kinematic fit requiring energy and momentum conservation must converge with a probability of $log_{10}P(\chi^2)_{4C} > -12$. Due to the lack of neutrinos at the beginning of the decay chain in the signal events, there should be no significant energy missing in the event.

6. A five constraint kinematic fit which additionally requires that the event is consistent with the decay of two particles of equal mass must yield $log_{10}P(\chi^2)_{5C} > -12$.

7. C-parameter > 0.25. A multi-jet signal event is more spherical than a two-fermion event.

8. $\mathcal{B}_{evt} > 0.4$. The high number of b-hadrons in the signal is exploited in this cut.

As shown in table 6.1, the preselection is efficient for the signal at each preselection step, while achieving excellent background suppression. The signal at the mass point $m_{\mathrm{H}}{}^{\pm} =$ 60 GeV/c^2 and $m_{\mathrm{A}}{}^{0} = 30$ GeV/c^2 is chosen as an example for the efficiency. The good background to data agreement, at each stage of the preselection, is illustrated in figure 6.1. No two-photon event survives the preselection.

6.1.2 The Likelihood-Selection

After the preselection a likelihood-selection is performed using three different classes: a) the signal class, b) the four-fermion background class and c) the two-fermion background class. The generated events surviving the preselection are used to produce normalised reference distributions for each class in selected variables. From these reference distributions an overall likelihood for an event to belong to the signal class is computed, according to equation 5.12. The selection is divided into two analyses, optimised for two Higgs mass regions, by using selected charged Higgs masses for the reference distributions. Charged Higgs masses of 40 and 50 GeV/c^2 were combined to produce the low mass reference histograms and masses between 60 and 80 GeV/c^2 were used for the high mass reference histograms. For the clarity of presentation only the low mass distributions are shown here because these results are used to obtained the final combined results with the other centre-of-mass energies. The high mass analysis is given in [8].

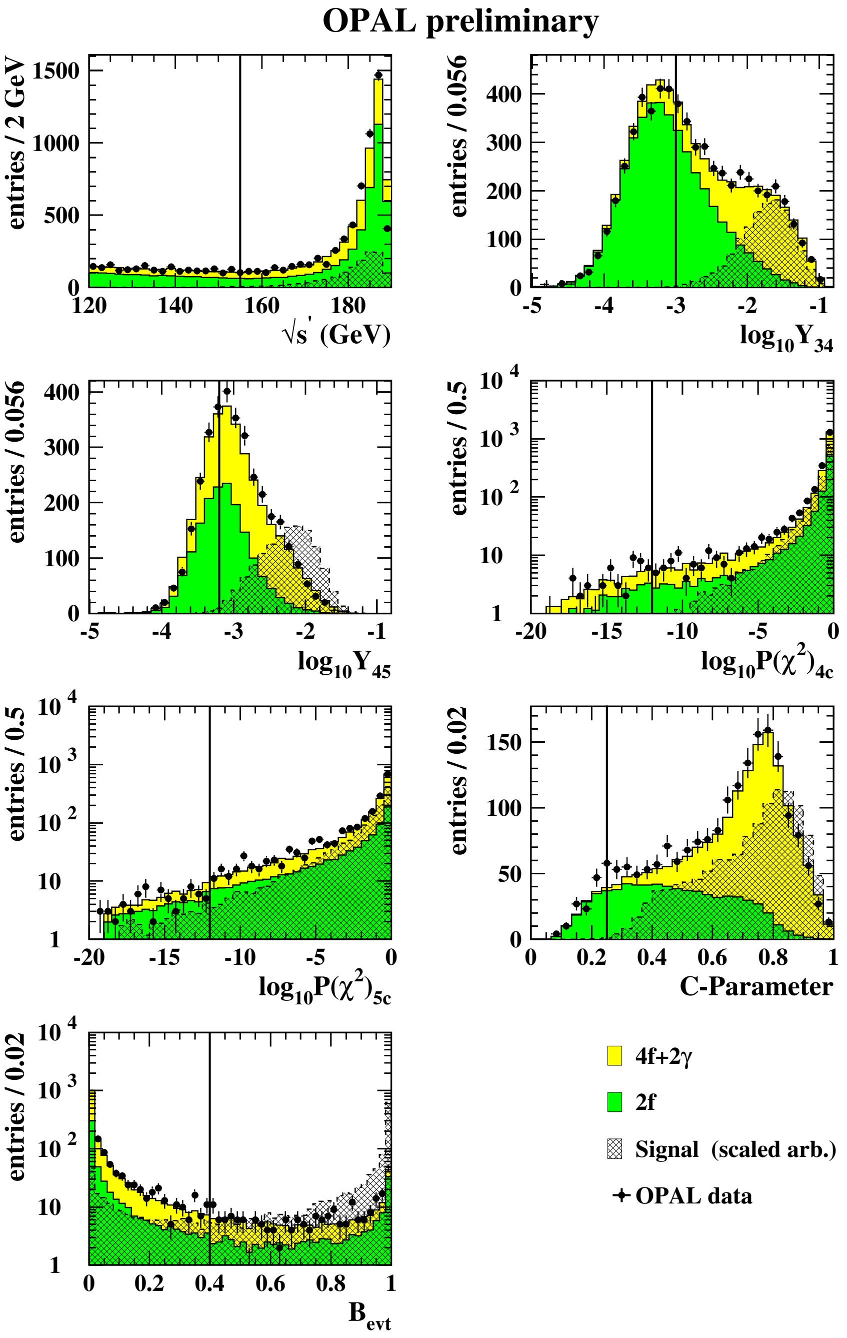

Figure 6.1: *A comparison of the distribution of data (filled circles) and Monte Carlo simulation at each stage of the hadronic channel preselection at a centre-of-mass energy of 189 GeV. The total background is resolved into two fermion (dark shaded) and four fermion (light shaded) components. The hatched area shows the superposition of simulated signal distributions scaled up for visibility. The vertical lines show the applied cuts.*

The following variables are used in the likelihood analysis for the **low mass** analysis (see section 5 for their definition). Their choice was optimised using the PC package [57, 58], developed at OPAL especially for the optimisation of likelihood selections.

1. The logarithm of the jet resolution parameters, $log_{10}(Y_{23})$, $log_{10}(Y_{34})$, $log_{10}(Y_{56})$, $log_{10}(Y_{45})$ and $log_{10}(Y_{67})$. These variables focus on the multi-jet character of the events.
2. The sphericity.
3. The maximum jet energy, E_{jet}^{max}, after forcing the event to four jets.
4. The maximum opening angle of the sub-jet containing 68% of the jet's total energy after forcing the event to four jets, $max(cos\theta_{jet}^{68\%})$.
5. The W decay angle.
6. The B event likelihood, $\mathcal{B}_{evt}$.

Figure 6.2 shows a comparison of data and background for the reference variables used in the low mass selection. Some slight fluctuations of the data to the background can be seen but no outstanding mismodelling is visible. Some variables, e.g. the *maximal jet energy*, show their discriminating power only if the background is split into two classes. The total background shows the same distribution as the signal and therefore would have no discriminating power.

A combined signal likelihood distribution for an event of the data, the two-fermion, the four-fermion and the signal event sample to belong to the signal class is calculated, according to equation 5.12 from the reference distributions. The background events are normalised according to their cross-section and the data luminosity. Events with a signal-likelihood close to one have a high probability of being signal-like while events with a signal-likelihood close to zero are more background-like[1]. Ideally the likelihood distribution for the signal events should peak at one while the distributions of the background events should peak at zero and vanish for one. However, the behaviour of the likelihood distributions for the background depends on the amount of irreducible background and on the distinguishing power of the analysis. The good selection power of the variables of the analyses can be seen in the likelihood distribution in figure 6.3. A likelihood cut of 0.9 (optimised with the PC package [57, 58]) is chosen for the final likelihood selection, giving good signal efficiency and good background suppression. This yields a final number of 8 data events and 7.18 background events. For $m_{\mathrm{H}}{}^{\pm} = 60$ GeV/c^2 and $m_{\mathrm{A}}{}^{0} = 30$ GeV/c^2 the analysis yields a signal efficiency of 21%.

The signal efficiency after the likelihood selection is computed for every mass point ($m_{\mathrm{H}}{}^{\pm}$;$m_{\mathrm{A}}{}^{0}$) at which events were generated. To calculate the signal efficiency for arbitrary Higgs masses, interpolation functions are determined with the use of spline fits. This function is shown in figure 6.4 against $m_{H^{\pm}}$ and m_{A^0}. The efficiencies are zero in the upper left corner of the three-dimensional plot because this is out of kinematic reach. The efficiency function also demonstrates the regions for which the analysis was optimised for.

---

[1] In the following the combined likelihood for an event to belong to the signal class is denoted simply as *combined likelihood value* or *likelihood*. There is of course also a likelihood value for each event to belong to the four-fermion and the two-fermion class.

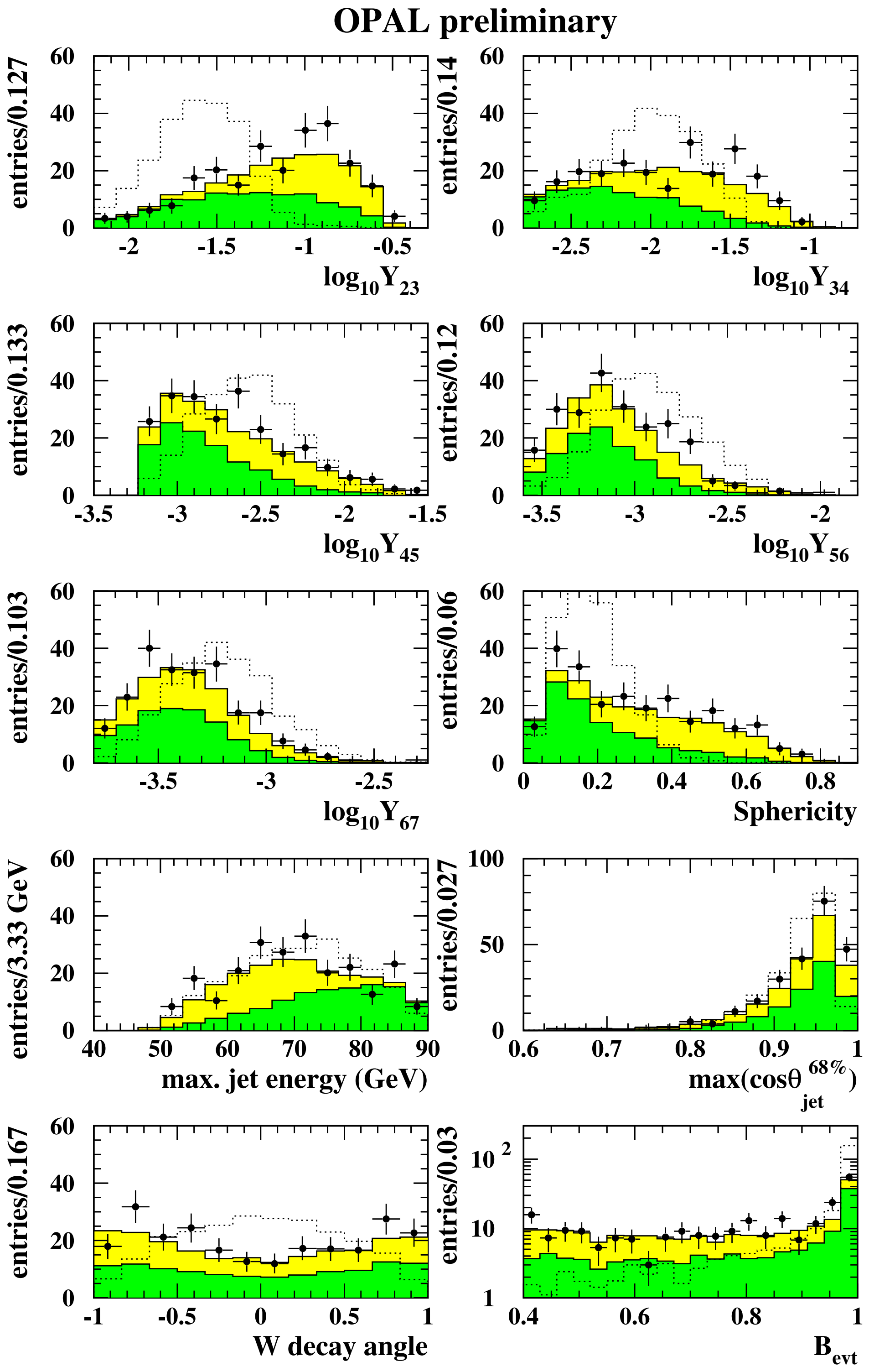

Figure 6.2: *The distribution of reference variables used in the low mass hadronic likelihood at a centre-of-mass energy of 189 GeV. The total background is resolved into two fermion (dark shaded) and four fermion (light shaded) components. The dashed line shows the superposition of simulated signal distributions scaled up for visibility.*

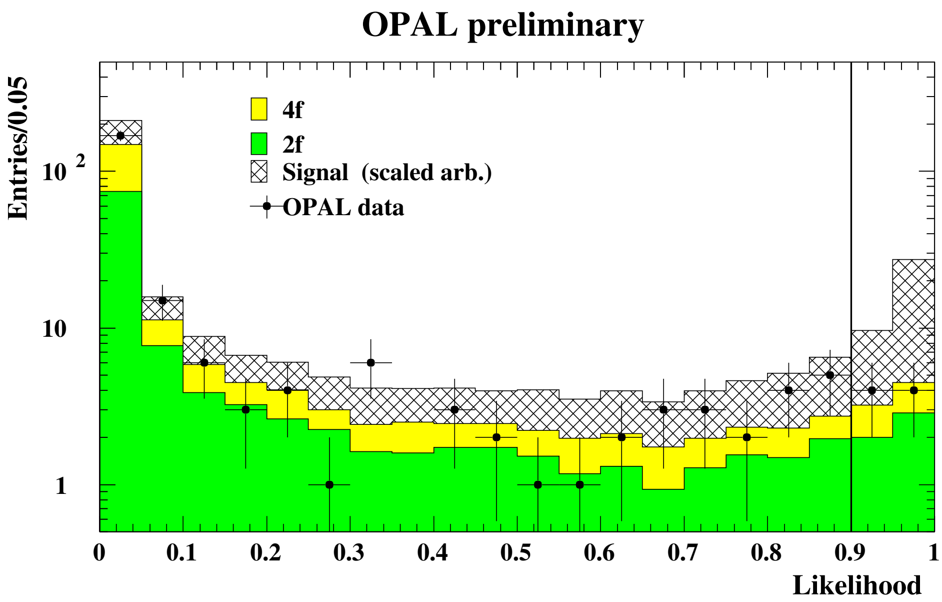

Figure 6.3: *The likelihood distribution for the low mass hadronic analysis at a centre-of-mass energy of 189 GeV. The dark shaded region is the two-fermion likelihood, the light shaded region is the four-fermion likelihood and the hatched region is the likelihood distribution expected for signal which is scaled arbitrarily. The points show the data. The vertical line shows the applied cut.*

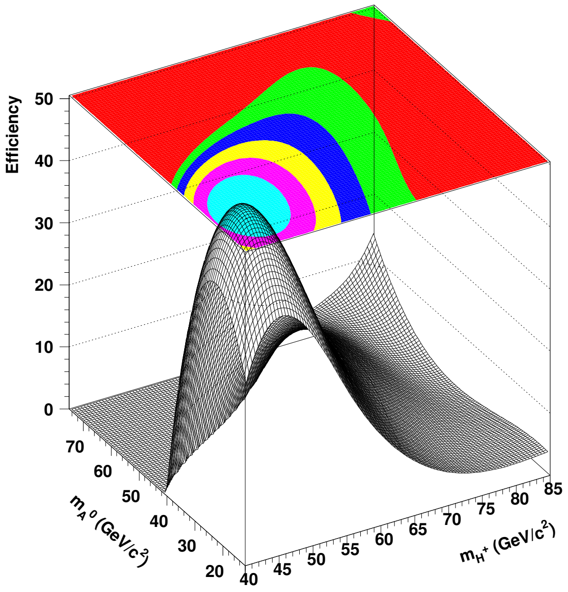

Figure 6.4: *The efficiencies (in percent) for the hadronic signal events in the low mass hadronic event selection at a centre-of-mass energy of 189 GeV against* $m_{H^\pm}$ *and* m_{A^0}*. The grey bands in the top plane demonstrate qualitatively the regions of equal efficiency.*

6.2 Search at $\sqrt{s}$ =192-206 GeV

6.2.1 The Preselection

The preselection at the centre-of-mass energies of 192-206 GeV is changed slightly with respect to the search at $\sqrt{s}$ =189 GeV. Cuts on variables with little selection power were dropped (C-parameter, $log_{10}(Y_{45})$ and the five constraint fit) and some cuts on the remaining variables were tightened.

1. The event has to meet the requirement of a multi-hadronic event.
2. A cut of $\sqrt{s'} > 155\ GeV$ is used.
3. $log_{10}(Y_{34}) > -2.5$.
4. The number of charged tracks of the jet with the lowest multiplicity, N^{ch}_{jet}, should be greater or equal to two. In the $\sqrt{s}$ =189 GeV analysis there is an indirect cut, in the $\mathcal{B}_{evt}$, on the number of charged tracks per jet to be greater than one.
5. A four constraint kinematic fit requiring energy and momentum conservation must converge with a probability of $log_{10}P(\chi^2)_{4C} > -8$.
6. $\mathcal{B}_{evt} > 0.4$.

A data to background comparison of the variables used in the preselection are shown in figures 6.5 and 6.6 for $\sqrt{s}$ =192-202 GeV and $\sqrt{s}$ =206 GeV, respectively. As demonstrated in tables 6.2 and 6.3 the background to data comparison agrees for the different preselection steps. There is a slight excess in the data after the last preselection cut.

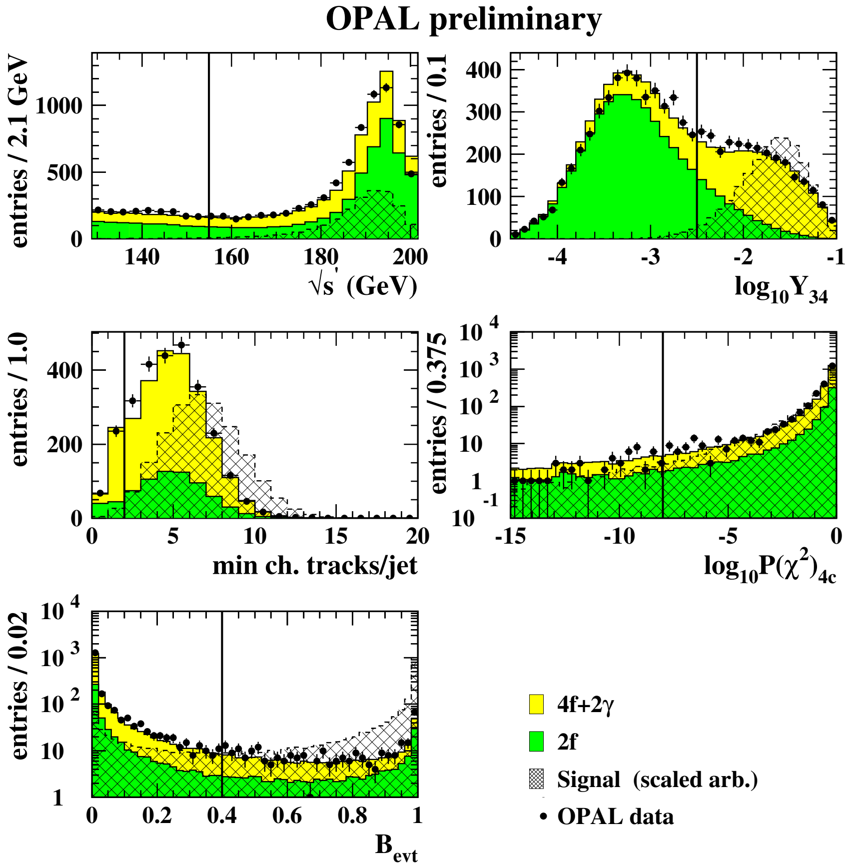

Figure 6.5: *A comparison of the distribution of data (filled circles) and Monte Carlo simulation at each stage of the hadronic channel preselection at a centre-of-mass energy of 192-202 GeV. The total background is resolved into two fermion (dark shaded) and four fermion (light shaded) components. The hatched area shows the superposition of simulated signal distributions scaled up for visibility. The vertical lines show the applied cuts.*

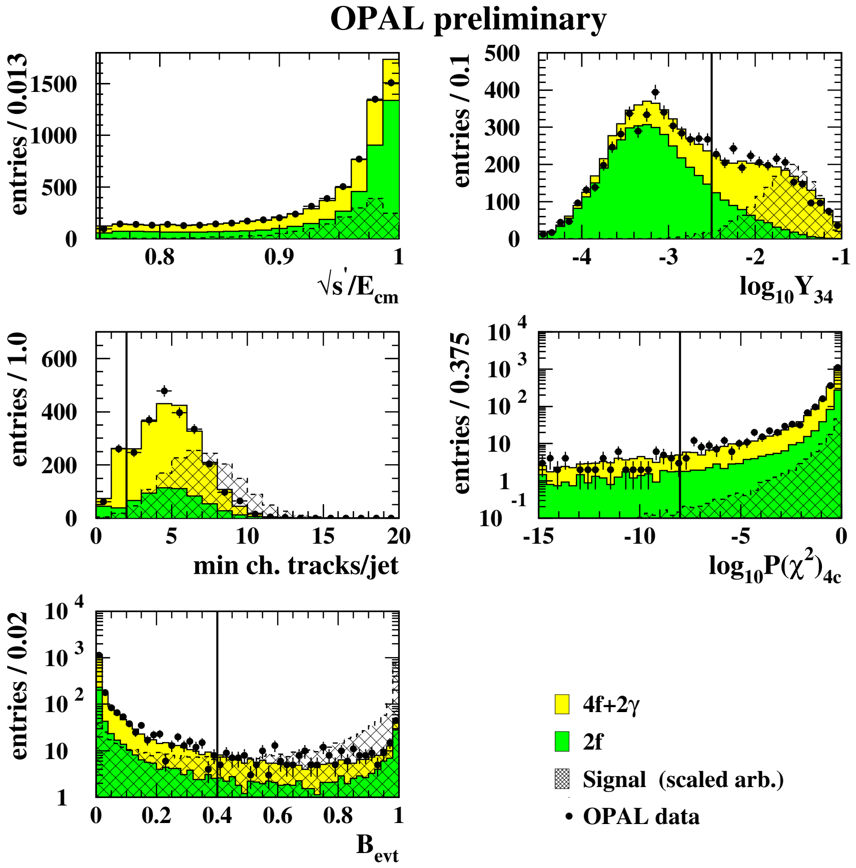

Figure 6.6: *A comparison of the distribution of data (filled circles) and Monte Carlo simulation at each stage of the hadronic channel preselection at a centre-of-mass energy of 206 GeV. The total background is resolved into two fermion (dark shaded) and four fermion (light shaded) components. The hatched area shows the superposition of simulated signal distributions scaled up for visibility. The vertical lines show the applied cuts.*

Hadronic Channel $\sqrt{s}$ =192 GeV - 202 GeV						
Cut	Data	Total bkg.	2-fermi	4-fermi.	2-photon	Signal Eff. (%) $m_{\mathrm{H}} = 60$ GeV/c^2 $m_{\mathrm{A}} = 30$ GeV/c^2
hadronic event	20831	20765.2	16254.2	4228.4	282.6	99.6
$\sqrt{s'}$	7332	7342.9	4713.4	2607.5	22.0	97.6
$\log_{10} Y_{34} > -2.5$	2710	2591.5	714.4	1873.8	3.3	96.6
$N^{ch}_{jet} \geq 2.$	2407	2280.5	631.1	1648.5	0.9	96.0
$log_{10} P(\chi^2)_{4C}$	2271	2125.2	575.7	1549.2	0.3	93.8
B_{evt} >0.4	**297**	**245.9**	116.1	129.8	0.0	**80.2**

Table 6.2: *The number of data and Monte Carlo events at each stage of the preselection for the hadronic channel for $\sqrt{s}$ =192-202 GeV, and the efficiency for the hadronic signal events with $m_{H^+} = 60$ GeV/c^2 and $m_{A^0} = 30$ GeV/c^2 (for $\sqrt{s}$ =200 GeV).*

Hadronic Channel $\sqrt{s}$ =206 GeV						
Cut	Data	Total bkg.	2-fermi	4-fermi.	2-photon	Signal Eff. (%) $m_{\mathrm{H}} = 60$ GeV/c^2 $m_{\mathrm{A}} = 30$ GeV/c^2
hadronic event	18135	18453.5	13988.2	4172.4	292.9	100.0
$\sqrt{s'}$	6860	7033.7	4299.1	2707.6	27.0	98.0
$\log_{10} Y_{34} > -2.5$	2532	2526.4	648.5	1871.0	6.9	97.0
$N^{ch}_{jet} \geq 2.$	2210	2190.8	566.4	1622.1	2.3	95.0
$log_{10} P(\chi^2)_{4C}$	2032	2007.0	500.8	1505.4	0.8	92.2
B_{evt} >0.4	**265**	**230.7**	100.8	129.9	0.0	**80.0**

Table 6.3: *The number of data and Monte Carlo events at each stage of the preselection for the hadronic channel for $\sqrt{s}$ =206 GeV, and the efficiency for the hadronic signal events with $m_{H^+} = 60$ GeV/c^2 and $m_{A^0} = 30$ GeV/c^2.*

6.2.2 The Likelihood-selection

The likelihood-selection is not split into a low and high charged Higgs mass region as for $\sqrt{s}$ =189 GeV. The results of all centre-of-mass energies are used in the calculation of the excluded regions in the 2HDM model I, including those of the low mass selections at $\sqrt{s}$ =189 GeV. Since a good coverage is obtained for low charged Higgs masses from the analysis at $\sqrt{s}$ =189 GeV, the analyses at 192-206 GeV focus on the higher charged Higgs masses. Only one analysis is used and no optimisation for a specific mass range is necessary. A choice of variables similar to the high-mass selection choice at $\sqrt{s}$ =189 GeV (described in [8]) are used. The *oblateness* against $log_{10}(Y_{23})$ is illustrated in figure 6.7 for the observed data events at $\sqrt{s}$ =206 GeV (after the preselection). $log_{10}(Y_{23})$ is a variable used in the $\sqrt{s}$ =189 GeV analysis. The correlation between the two variables is visible. In the improved analyses, at 192-206 GeV, the likelihood variables which had a high correlation coefficient with others or which showed differences in the correlation coefficient in observed data and background events were no longer used in the likelihood selection (see section 5.3). The following variables are used in the likelihood selection.

1. The jet resolution parameters $log_{10}(Y_{34})$ and $log_{10}(Y_{56})$.
2. The oblateness.
3. The maximum opening angle of the sub-jet containing 68% of the jet's total energy after forcing the event to four jets.
4. The W decay angle.
5. $\mathcal{B}_{evt}$.

The corresponding distributions are shown in figure 6.8. The slight excess in the observed data after the preselection is visible in the distributions.

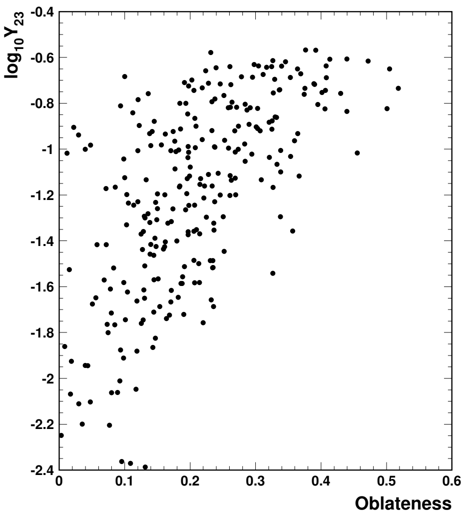

Figure 6.7: *The jet-resolution parameter* $log_{10}(Y_{23})$ *against the oblateness in the* $\sqrt{s}$ *=206 GeV observed data after the preselection.*

A cut of 0.6 is applied in the likelihood distribution, as shown in figure 6.9, gaining good signal to background rejection. After the likelihood selection 33 data events remain for the $\sqrt{s}$ =192-202 GeV selection and 22.8 expected background events. The signal efficiency for $m_{H^\pm} = 60$ GeV/c^2 and $m_{A^0} = 30$ GeV/c^2 is 66% (at $\sqrt{s} = 200$ GeV). For the

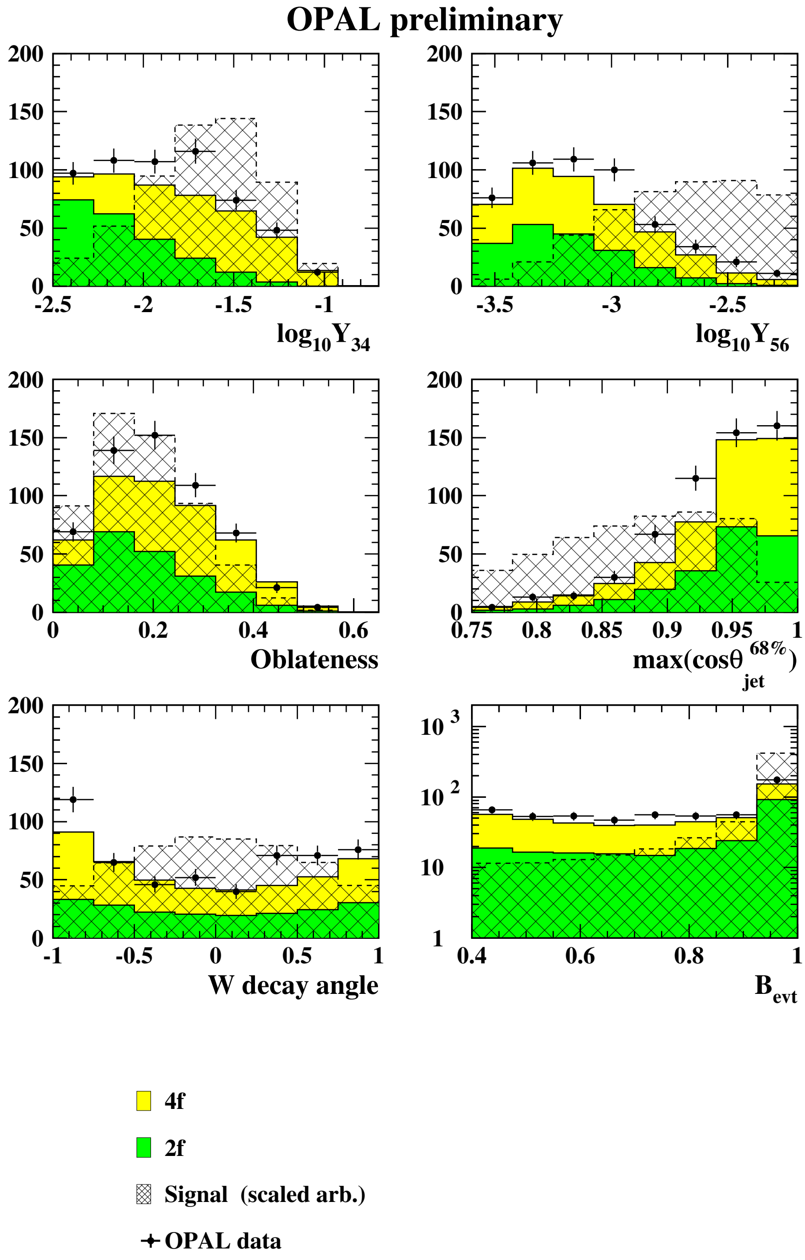

Figure 6.8: *The distribution of reference variables used in the hadronic likelihood at a centre-of-mass energies of 192-206 GeV. The total background is resolved into two fermion (dark shaded) and four fermion (light shaded) components. The dashed line shows the superposition of simulated signal distributions scaled up for visibility.*

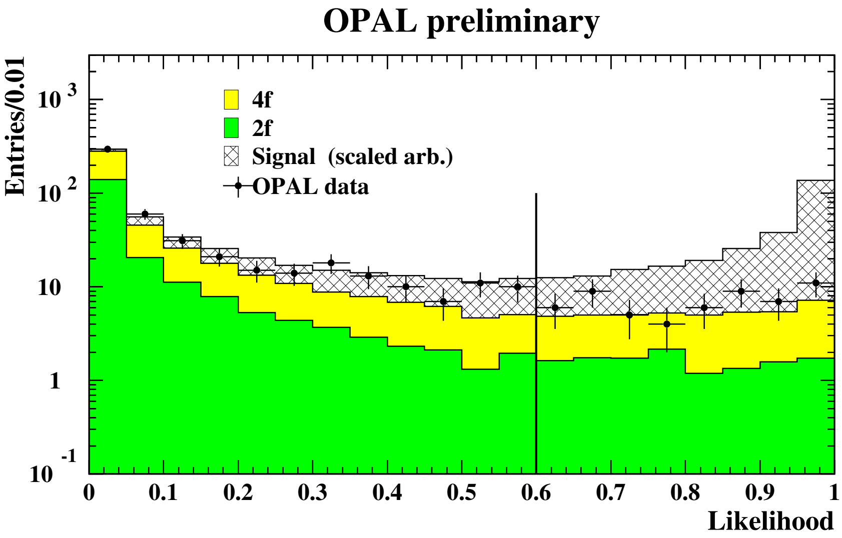

Figure 6.9: *The likelihood distribution for the hadronic analysis at a centre-of-mass energy of 192-206 GeV. The dark shaded region is the two-fermion likelihood, the light shaded region is the four-fermion likelihood and the hatched region is the likelihood distribution expected for signal which is scaled arbitrarily. The points show the data. The vertical line shows the applied cut.*

Hadronic Channel $\sqrt{s}$ =192 GeV - 206 GeV					
$\sqrt{s}$ in GeV	Data	Total bkg.	2-fermi	4-fermi.	Signal Eff. (%) $m_{\mathrm{H}} = 60$ GeV/c^2 $m_{\mathrm{A}} = 30$ GeV/c^2
192-202	33	22.9	7.5	15.4	**65.8** at $\sqrt{s}$ =200 GeV
206 (200-209)	24	20.6	5.7	14.9	**58.2** at $\sqrt{s}$ =206 GeV
total	**57**	**43.5**	13.2	30.3	

Table 6.4: *The number of data and Monte Carlo events after the likelihood selection for the hadronic channel and the efficiency for the hadronic signal events with $m_{H^+} = 60$ GeV/c^2 and $m_{A^0} = 30$ GeV/c^2 for $\sqrt{s}$ =192-202 GeV (data taken in the year 1999 between 192-202 GeV) and 206 GeV (data taken in the year 2000 for 200-209 GeV with a luminosity weighted mean of 206 GeV).*

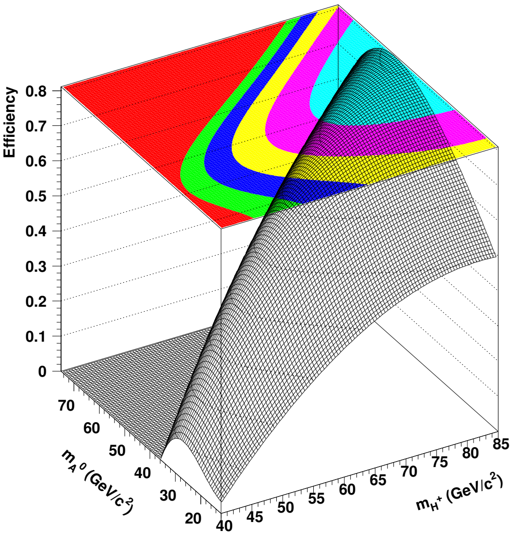

Figure 6.10: *The efficiencies of the hadronic signal events in the hadronic event selection at a centre-of-mass energy of 206 GeV against* $m_{H^\pm}$ *and* m_{A^0}*. The grey bands in the top plane demonstrate qualitatively the regions of equal efficiency.*

$\sqrt{s}$ =206 GeV selection 24 data candidates remain and 20.6 expected background events. The signal efficiency for $m_{\mathrm{H}}{}^{\pm} = 60$ GeV/c^2 and $m_{\mathrm{A}}{}^{0} = 30$ GeV/c^2 is 58%. Table 6.4 summarises the results. The two-dimensional function of the efficiency is shown in figure 6.10 at $\sqrt{s}$ =206 GeV against $m_{H^\pm}$ and m_{A^0}. The best efficiencies are achieved at high $m_{H^\pm}$.

Chapter 7

The Leptonic Search Channel

7.1 Search at $\sqrt{s}$ =189 GeV

7.1.1 The Preselection

The W^*-mediated leptonic channel, $\mathrm{e^+e^-} \to \mathrm{H^+H^-} \to W^{*+}A^0W^{*-}A^0 \to \ell\nu\mathrm{b\bar{b}q\bar{q}'b\bar{b}}$ +c.c., resulting from the decay of both charged Higgs bosons into a virtual W^* and a A^0 boson, differs from the hadronic channel because *one* of the virtual W bosons decays leptonically. Therefore, its topology is similar to the hadronic channel but with a certain amount of energy missing because of the neutrino. A similar preselection is used. The variables used are:

1. The event has to pass the multi-hadronic event selection.
2. $\sqrt{s'} > 120$ GeV.
3. $log_{10}(Y_{34}) > -3.0$.
4. $log_{10}(Y_{45}) > -3.2$.
5. C-parameter> 0.25.
6. $\mathcal{B}_{evt} > 0.4$.

Table 7.1 shows the number of background and data events after each preselection cut together with the signal efficiency for $m_{H^\pm} = 60$ GeV$/c^2$ and $m_{A^0} = 30$ GeV$/c^2$. After the preselection the number of background events has been reduced to a great extent retaining good signal efficiency. The correct modelling of the background to data distribution is shown in Figure 7.1, as well as the distributions for the signal events. There is a slight excess in data events after the last preselection cut.

Leptonic Channel $\sqrt{s}$ =189 GeV						
Cut	Data	Total bkg.	2-fermi	4-fermi.	2-photon	Signal Eff. (%) $m_{\mathrm{H}} = 60$ GeV$/c^2$ $m_{\mathrm{A}} = 30$ GeV$/c^2$
(1)	18815	18518.8	15005.5	3259.8	253.5	99.6
(2)	8344	8395.8	5709.8	2611.8	74.2	99.4
(3)	4755	4638.9	2472.7	2118.0	48.2	99.4
(4)	3206	3053.2	1472.7	1550.5	30.0	99.2
(5)	2955	2825.1	1259.2	1540.4	25.5	99.2
(6)	**358**	**316.2**	201.6	112.7	1.9	**82.2**

Table 7.1: *The number of data and Monte Carlo events at each stage of the preselection for the leptonic channel at a centre-of-mass energy of 189 GeV, and the efficiency for the leptonic signal events with* $m_{H^+} = 60$ *GeV*$/c^2$ *and* $m_{A^0} = 30$ *GeV*$/c^2$.

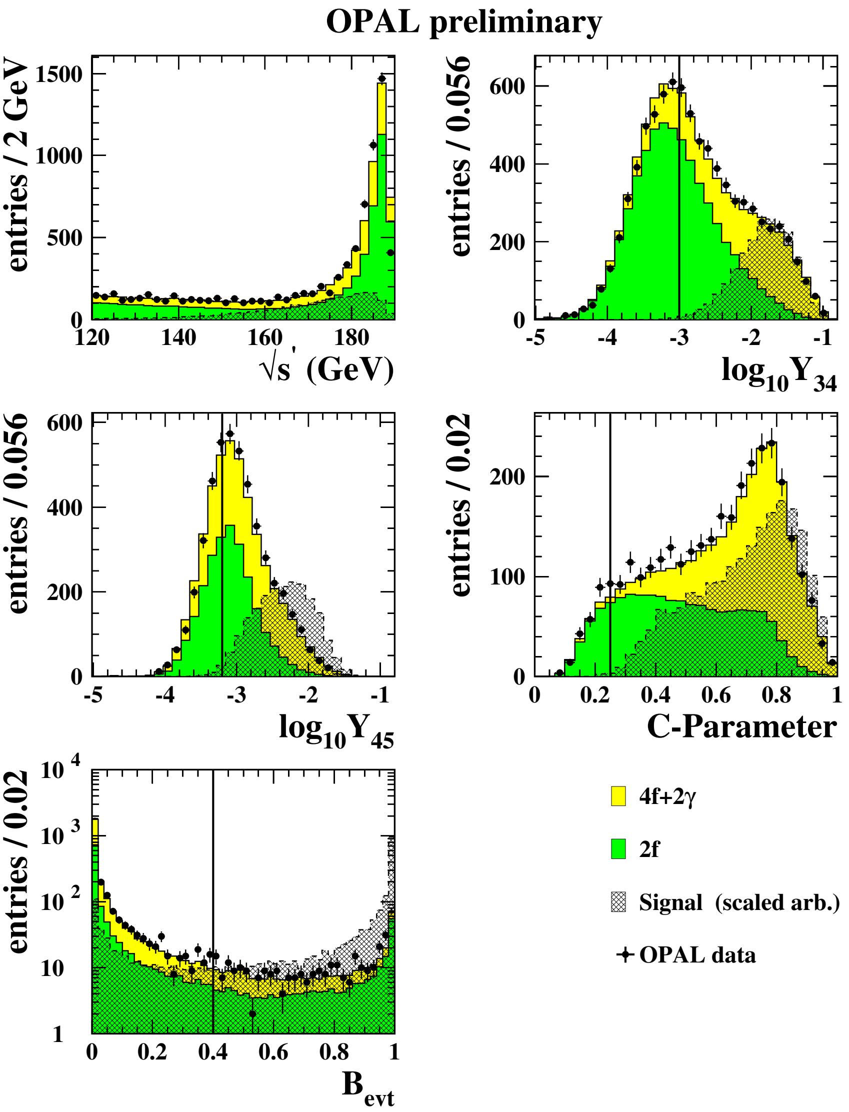

Figure 7.1: *A comparison of the distribution of data (filled circles) and Monte Carlo simulation at each stage of the leptonic channel preselection at a centre-of-mass energy of 189 GeV. The total background is resolved into two fermion (dark shaded) and four fermion (light shaded) components. The hatched area shows the superposition of simulated signal distributions scaled up for visibility. The vertical lines show the applied cuts.*

7.1.2 The Likelihood-Selection

As in the hadronic channel, signal events surviving the preselection with charged Higgs masses of 40 and 50 GeV/c^2 were combined to produce the low mass reference histograms and masses between 60 and 80 GeV/c^2 were used for the high mass reference histograms. Only the results of the results of the low mass selection are shown here because these are combined with those at higher centre-of-mass energies, just as for the hadronic channel (see [8] for details of the high mass analysis). The following variables were chosen for the likelihood selection.

1. $log_{10}(Y_{23})$, $log_{10}(Y_{34})$ and $log_{10}(Y_{56})$.
2. $E_{miss}/\sqrt{s}$. This variable accounts for the energy missing in the event due to the neutrino in the final state.
3. The sphericity and oblateness. The use of both variables gave the best signal-to-background separation.
4. E_{jet}^{max}.
5. $\mathcal{B}_{evt}$.

The distributions of the variables for the data, the expected background and the expected signal events used as input to the low mass likelihood selection are shown in figure 7.2. Good agreement between the data and background events can be seen. Figure 7.3 illustrates the combined likelihood distributions for the low mass selection for data, the background and signal events.

A cut on the likelihood distribution of 0.7 was chosen which gives good efficiency as shown in figure 7.4. After the likelihood selection 32 data candidate remain and 26.2 background events for the low mass analysis. The efficiency of a signal with $m_{\mathrm{H}^{\pm}}$ = 60 GeV/c^2 and m_{A^0} = 30 GeV/c^2 is 39%. The efficiency of the signal events is 48% with $m_{\mathrm{H}^{\pm}}$ = 60 GeV/c^2 and m_{A^0} = 30 GeV/c^2.

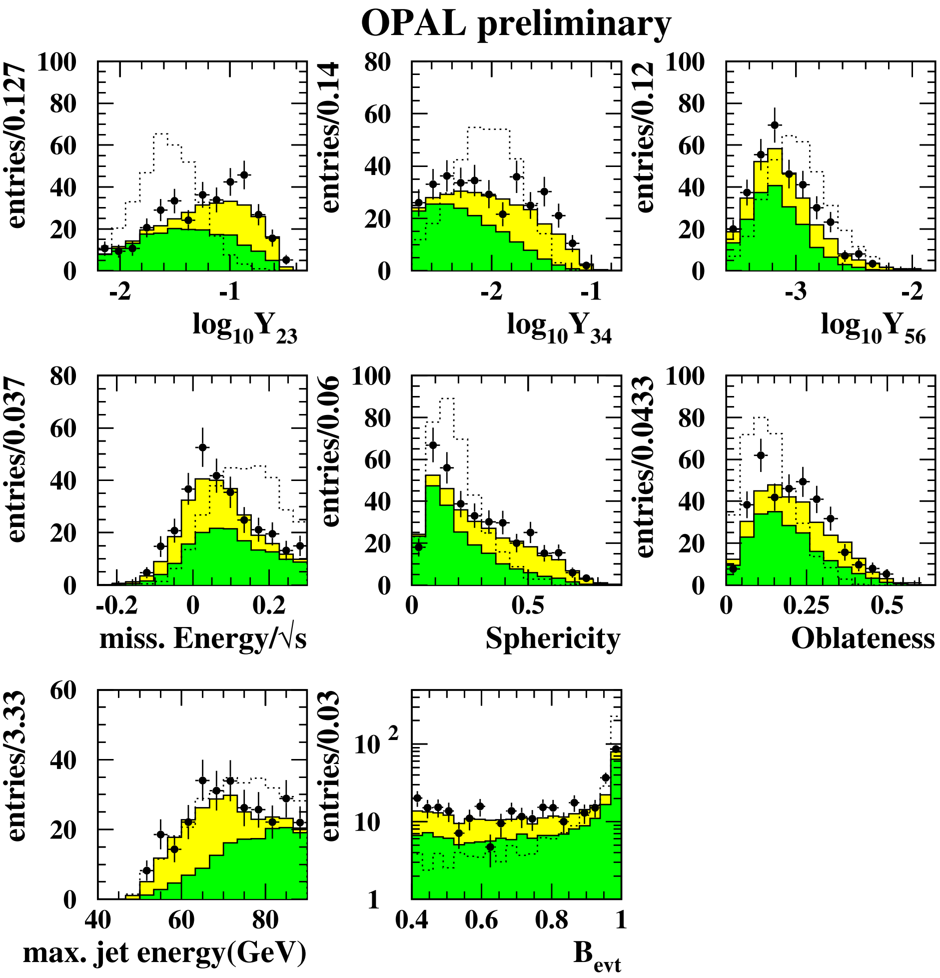

Figure 7.2: *The distribution of reference variables used in the low mass leptonic likelihood at a centre-of-mass energy of 189 GeV. The total background is resolved into two fermion (dark shaded) and four fermion (light shaded) components. The dashed line shows the superposition of simulated signal distributions scaled up for visibility.*

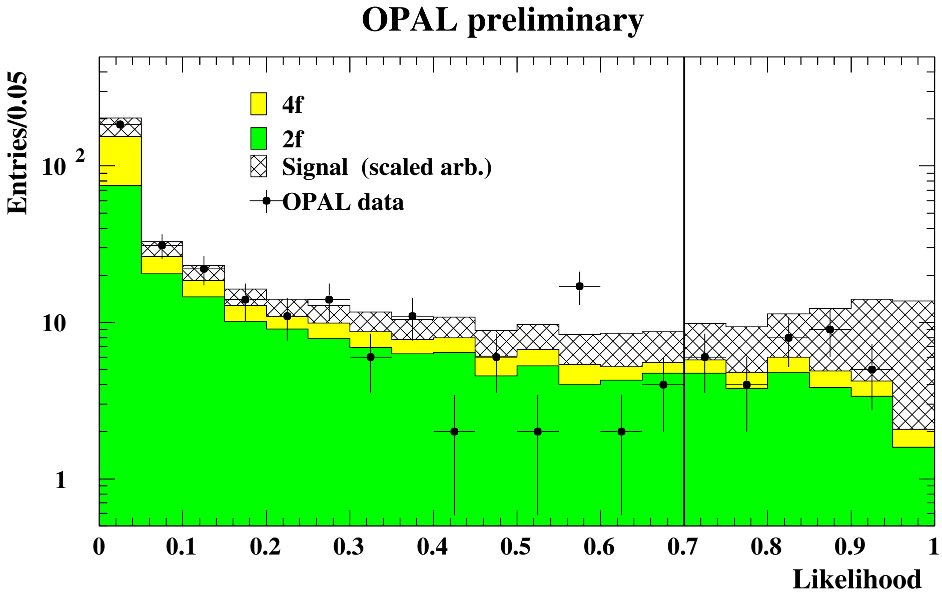

Figure 7.3: *The likelihood distribution for the low mass leptonic analysis at a centre-of-mass energy of 189 GeV. The dark shaded region is the two-fermion likelihood, the light shaded region is the four-fermion likelihood and the hatched region is the likelihood distribution expected for signal which is scaled arbitrarily. The points show the data. The vertical line shows the applied cut.*

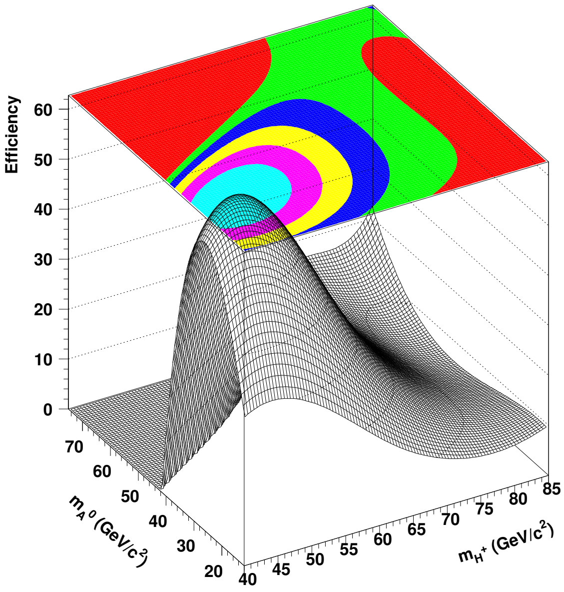

Figure 7.4: *The efficiencies (in percent) for the leptonic signal events in the low mass leptonic event selection at a centre-of-mass energy of 189 GeV against* $m_{H^\pm}$ *and* m_{A^0}*. The grey bands in the top plane demonstrate qualitatively the regions of equal efficiency.*

7.2 Search at $\sqrt{s}$ =192-206 GeV

7.2.1 The Preselection

At preselection level some variables with less selection power were dropped (C-parameter and $log_{10}(Y_{45})$) and the following variables were used. Again the aim is to increase the sensitivity of the analysis:

1. The event has to meet the requirement of a multi-hadronic event.
2. $\sqrt{s'} > 155\ GeV$.
3. $log_{10}(Y_{34}) > -2.5$.
4. The number of charged tracks of the jet with the lowest multiplicity, N^{ch}_{jet}, should be greater or equal to two. In the $\sqrt{s}$ =189 GeV analysis there is an indirect cut on the number of charged tracks per jet to be greater than one in the $\mathcal{B}_{evt}$.
5. $\mathcal{B}_{evt} > 0.4$.

A data-to-background comparison of the variables used in the preselection are shown in figures 7.5 and 7.6 for $\sqrt{s}$ =192-202 GeV and $\sqrt{s}$ =206 GeV, respectively. As illustrated in tables 7.2 and 7.3 the background to data comparison agrees, for the different preselection steps. Although there is a small excess in data events visible especially after the last preselection step.

Leptonic Channel $\sqrt{s}$ =192 GeV - 202 GeV						
Cut	Data	Total bkg.	2-fermi	4-fermi.	2-photon	Signal Eff. (%) $m_{\mathrm{H}} = 60$ GeV/c^2 $m_{\mathrm{A}} = 30$ GeV/c^2
hadronic event	20831	20765.2	16254.2	4228.4	282.6	99.8
$\sqrt{s'}$ GeV	7332	7342.9	4713.4	2607.5	22.0	92.4
$\log_{10} Y_{34} > -2.5$	2710	2591.5	714.4	1873.8	3.3	89.6
$N^{ch}_{jet} \geq 2.$	2407	2280.5	631.1	1648.5	0.9	80.0
B_{evt} >0.4	**310**	**259.3**	125.9	133.4	0.0	**66.2**

Table 7.2: *The number of data and Monte Carlo events at each stage of the preselection for the leptonic channel for $\sqrt{s}$ =192-202 GeV, and the efficiency for the leptonic signal events with $m_{H^+} = 60$ GeV/c^2 and $m_{A^0} = 30$ GeV/c^2 (for $\sqrt{s} = 200$ GeV).*

Leptonic Channel $\sqrt{s}$ =206 GeV						
Cut	Data	Total bkg.	2-fermi	4-fermi.	2-photon	Signal Eff. (%) $m_{\mathrm{H}} = 60$ GeV/c^2 $m_{\mathrm{A}} = 30$ GeV/c^2
hadronic event	18135	18453.5	13988.2	4172.4	292.9	100.0
$\sqrt{s'}$ GeV	6860	7033.7	4299.1	2707.6	27.0	95.6
$\log_{10} Y_{34} > -2.5$	2532	2526.4	648.5	1871.0	6.9	93.4
$N^{ch}_{jet} \geq 2.$	2210	2190.8	566.4	1622.1	2.3	85.0
B_{evt} >0.4	**281**	**247.4**	112.1	135.3	0.0	**72.2**

Table 7.3: *The number of data and Monte Carlo events at each stage of the preselection for the leptonic channel for $\sqrt{s}$ =206 GeV, and the efficiency for the leptonic signal events with $m_{H^+} = 60$ GeV/c^2 and $m_{A^0} = 30$ GeV/c^2.*

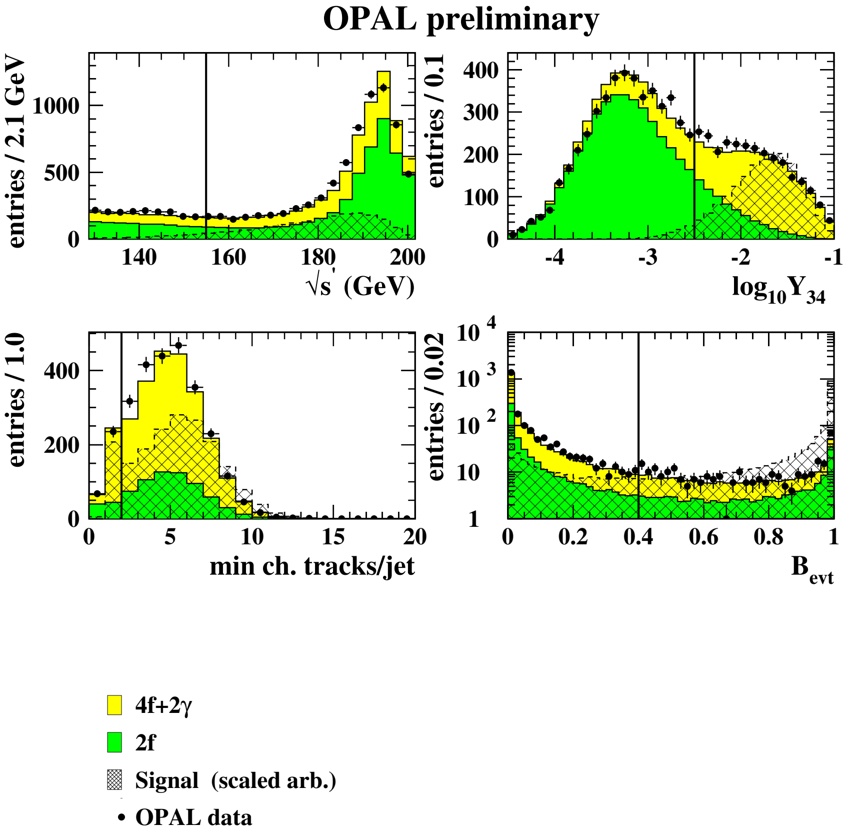

Figure 7.5: *A comparison of the distribution of data (filled circles) and Monte Carlo simulation at each stage of the leptonic channel preselection at a centre-of-mass energy of 192-202 GeV. The total background is resolved into two fermion (dark shaded) and four fermion (light shaded) components. The hatched area shows the superposition of simulated signal distributions scaled up for visibility. The vertical lines show the applied cuts.*

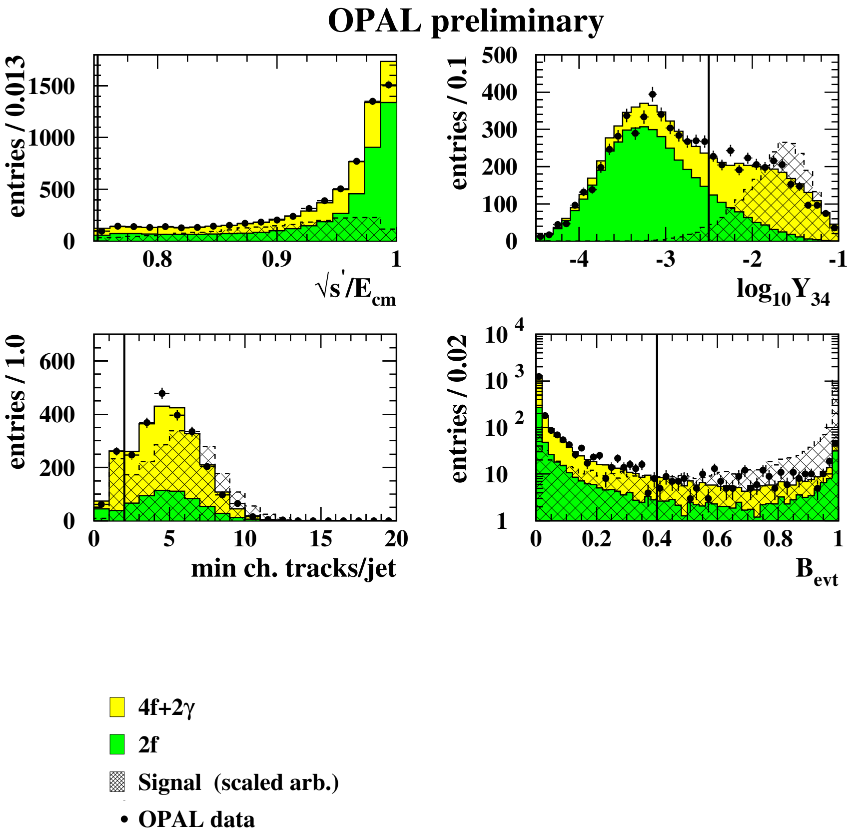

Figure 7.6: *A comparison of the distribution of data (filled circles) and Monte Carlo simulation at each stage of the leptonic channel preselection at a centre-of-mass energy of 206 GeV. The total background is resolved into two fermion (dark shaded) and four fermion (light shaded) components. The hatched area shows the superposition of simulated signal distributions scaled up for visibility. The vertical lines show the applied cuts.*

7.2.2 The Likelihood-Selection

Similar to the hadronic event selection, the number of likelihood variables is reduced for the $\sqrt{s}$ =192-206 GeV likelihood selection to lower possible correlations effects between the variables and variables with small impact on the selection are dropped. The following variables are used.

1. $log_{10}(Y_{34})$
2. $log_{10}(Y_{56})$
3. $E_{miss}/\sqrt{s}$
4. The oblateness.
5. $\mathcal{B}_{evt}$

The distributions of the reference variables are shown in figure 7.7. A slight excess in data events after the preselection can be seen in the distributions but no outstanding mismodelling is visible.

A cut of 0.6 was placed on the likelihood distribution shown in figure 7.8, optimised to give good efficiency for the signal and good background suppression. For the $\sqrt{s}$ =192-202 GeV selection, 33 data candidates remain with 19.8 expected background events, while 23 data candidates with 18.8 expected background survive for the $\sqrt{s}$ =206 GeV selection. The efficiency for $\sqrt{s}$ =192-202 GeV is 47% for $m_{H^\pm}$=60 GeV/c^2 and $m_{\mathrm{A}}{}^0$ = 30 GeV/c^2 and 49% for the $\sqrt{s}$ =206 GeV analysis. The results are summarised in table 7.4 which also show excess in data events especially for the $\sqrt{s}$ =192-202 GeV results. Possible effects which can lead to such an effect are going to be discussed in the context of the systematic error evaluation.

Figure 7.9 shows the efficiency function for the $\sqrt{s}$ =206 GeV selection. Again, the best efficiency is gained for high charged Higgs and intermediate m_{A^0}.

Leptonic Channel $\sqrt{s}$ =192 GeV - 206 GeV					
$\sqrt{s}$ in GeV	Data	Total bkg.	2-fermi	4-fermi.	Signal Eff. (%) m_{H} = 60 GeV/c^2 m_{A} = 30 GeV/c^2
192-202	33	19.8	8.7	11.1	**46.8** at $\sqrt{s}$ =200 GeV
206 (200-209)	23	18.8	6.6	12.2	**49.0** at $\sqrt{s}$ =206 GeV
total	**56**	**38.6**	15.3	23.3	

Table 7.4: *The number of data and Monte Carlo events after the likelihood selection for the leptonic channel and the efficiency for the leptonic signal events with* m_{H^+} = 60 *GeV/*c^2 *and* m_{A^0} = 30 *GeV/*c^2 *for* $\sqrt{s}$ *=192-202 GeV (data taken in the year 1999 between 192-202 GeV) and 206 GeV (data taken in the year 2000 for 200-209 GeV with a luminosity weighted mean of 206 GeV).*

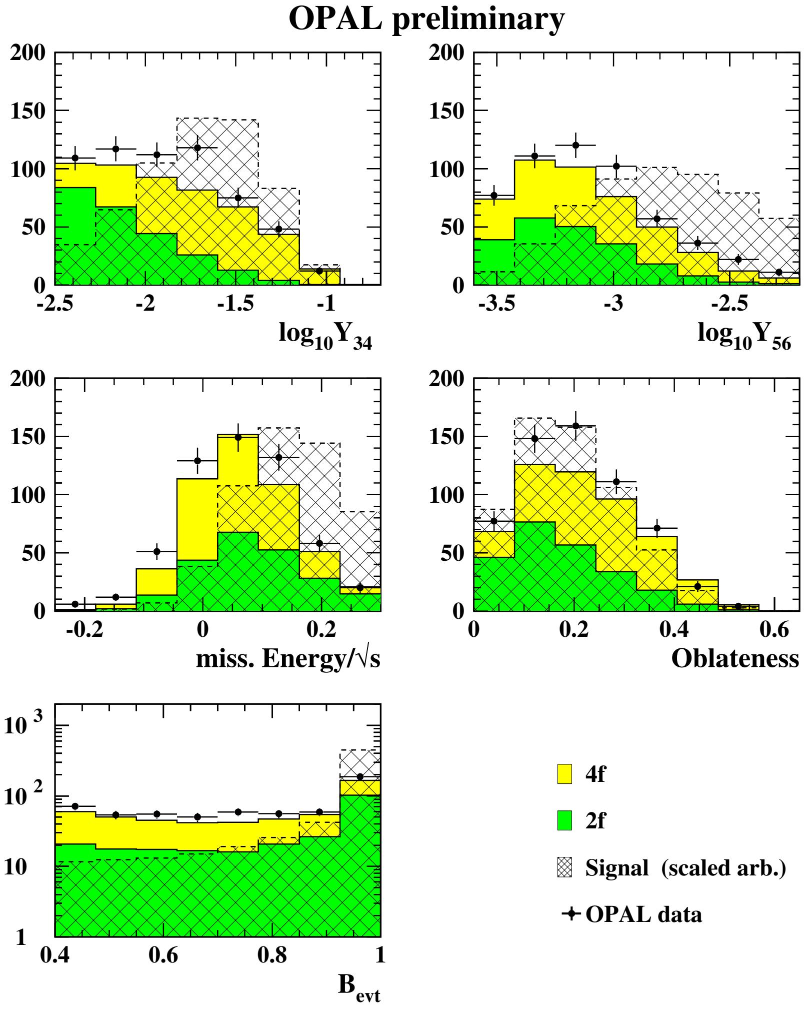

Figure 7.7: *The distribution of reference variables used in the leptonic likelihood at a centre-of-mass energy for* $\sqrt{s}$ *=192-206 GeV data. The total background is resolved into two fermion (dark shaded) and four fermion (light shaded) components. The dashed line shows the superposition of simulated signal distributions scaled up for visibility.*

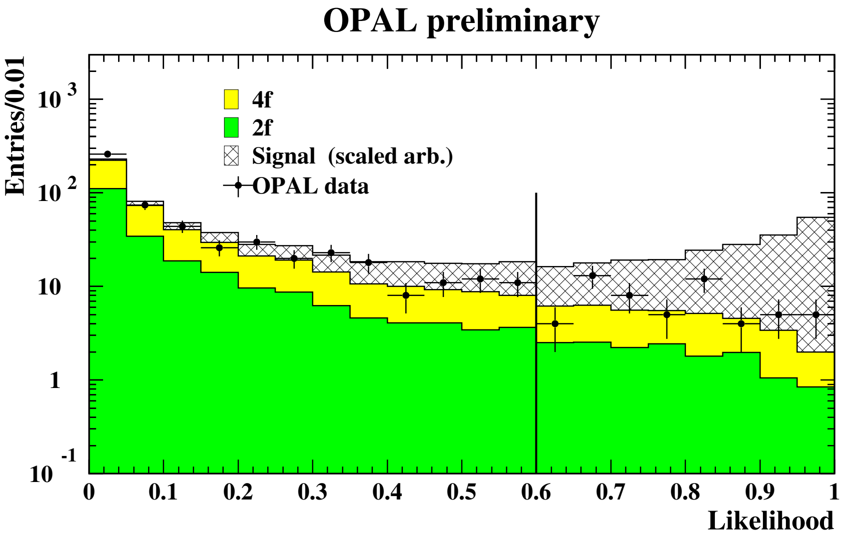

Figure 7.8: *The likelihood distribution for the leptonic analysis for $\sqrt{s}$ =192-206 GeV. The dark shaded region is the two-fermion likelihood, the light shaded region is the four-fermion likelihood and the hatched region is the likelihood distribution expected for signal which is scaled arbitrarily. The points show the data. The vertical line shows the applied cut.*

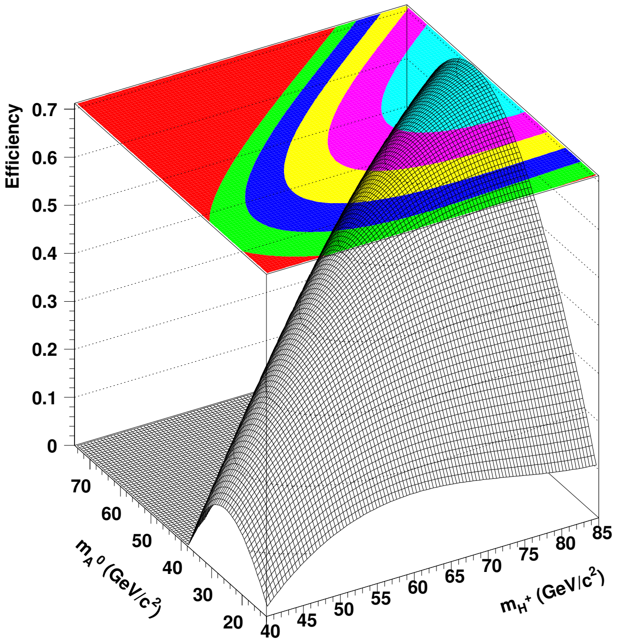

Figure 7.9: *The efficiencies of the leptonic signal events in the leptonic event selection at a centre-of-mass energy of 206 GeV against $m_{H^\pm}$ and m_{A^0}. The grey bands in the top plane demonstrate qualitatively the regions of equal efficiency.*

Chapter 8

The Tau Search Channel

8.1 Search at $\sqrt{s}$ =189 GeV

8.1.1 The Preselection

In the W^*-mediated tau channel, $\mathrm{e^+e^-} \rightarrow \mathrm{H^+H^-} \rightarrow \tau\nu W^{*-}A^0 \rightarrow \tau\nu \mathrm{q\bar{q}'b\bar{b}}$ +c.c., only *one* of the charged Higgs bosons decays via $H^\pm \rightarrow W^* A^0$. The other one decays leptonically into a tau-lepton and an associated neutrino. The tau-lepton is tagged using an artificial neural net algorithm (see section 5.1.4). Contrary to the hadronic and leptonic event selection, the low (40 GeV/c^2 $< m_{H^\pm} <$ 70 GeV/c^2) and high mass separation (70 GeV/c^2 $< m_{H^\pm} <$ 80 GeV/c^2) is already made at preselection level. The selections of the tau search channel show a greater dependency on the charged Higgs mass than the other two channels. This is caused by the reduced number of particles in the event and the direct dependency of the tau-tagging on $m_{H^\pm}$. Again only the **low mass analysis** is shown here (see [8] for details of the high mass analysis and also [59] for the likelihood distribution used). The variables used are:

- The event has to meet the requirement of a multi-hadronic event.
- $N^\tau_{ANN} \geq 1$. There should be at least one τ candidate with an ANN output of 0.5 or higher.
- $E_{vis}/\sqrt{s} < 0.85$. The visible energy should not be greater than 85% of the centre-of-mass energy $\sqrt{s}$ due to the missing energy associated with neutrino of the tau-lepton.
- $|\cos\theta(P_{miss})| < 0.9$.
- $-Q_\tau cos\theta(P_{rest}) > -0.8$.
- The jet resolution parameters of the remaining hadronic system after the tau-lepton is removed. $log_{10}(Y_{12}) < -0.4$ and $log_{10}(Y_{23}) > -2.76$ is required[1], as the charged Higgs boson decay is expected to be more isotropic than a two body (W boson) decay.
- $P_{transverse} > 14$ GeV/c.
- $E_{forward} < 20$ GeV.

A data and background comparison, for the low mass preselection is shown in table 8.1. After the preselection an efficiency of 64% for $m_{\mathrm{H}^\pm} = 50$ GeV/c^2 and $m_{\mathrm{A}^0} = 25$ GeV/c^2 is achieved. The corresponding distributions are shown in figure 8.1.

---

[1] The choice of the somewhat *crooked* 2.76 value is based on an early binning used in the presentation of the preselection variables.

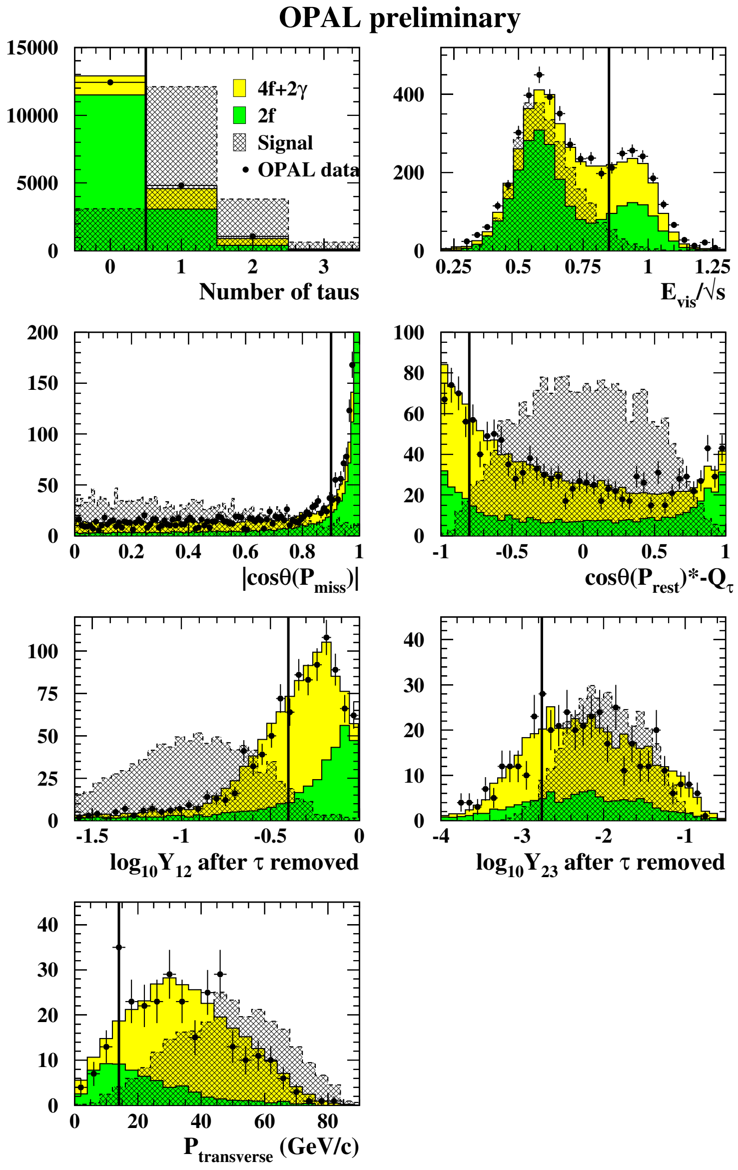

Figure 8.1: *A comparison of the distribution of data (filled circles) and Monte Carlo simulation at each stage of the low mass tau channel preselection at a centre-of-mass energy of 189 GeV. The total background is resolved into two fermion (dark) and four fermion (light) components. The hatched histogram area shows the superposition of simulated signal distributions scaled up for visibility. The vertical lines show the applied cuts.*

Tau Channel $\sqrt{s}$ =189 GeV						
Cut	Data	Total bkg.	2-fermi	4-fermi.	2-photon	Signal Eff. (%) $m_{\mathrm{H}} = 50$ GeV/c^2 $m_{\mathrm{A}} = 25$ GeV/c^2
hadronic event	18491	18671	15008	3260	214	99.7
≥ 1 τ candidate	4686	4345	2524	1742	79	77.2
$E_{vis}/\sqrt{s} < 0.85$	3309	3114	1895	1145	74	73.2
$\lvert\cos\theta(P_{miss})\rvert < 0.9$	1335	1383	462	903	18	71.4
$-Q_\tau \cdot \cos\theta(P) > -0.8$						
after τ removal	1068	1090	367	710	14	69.4
$\log_{10} Y_{12} < -0.4$						
after τ removal	433	441	114	318	10	67.6
$\log_{10} Y_{23} > -2.76$						
after τ removal	321	332	81	243	8	66.8
$P_T > 14$ GeV/c	263	274	45	226	4	64.6
$E_{forward} < 20$ GeV	**257**	**268**	41	223	4	**64.0**

Table 8.1: *The number of data and Monte Carlo events at each stage of the low mass preselection for the tau channel, and the efficiency for the tau signal events with* $m_{H^\pm} = 50$ *GeV/*c^2 *and* $m_{A^0} = 25$ *GeV/*c^2*.*

8.1.2 The Likelihood-Selection

After the preselection a likelihood selection is performed with the following variables for the low mass analysis:

- The momentum of the tau-lepton, P_τ.
- $cos(\tau - to - nearest - jet - angle)$.
- The jet resolution parameter $log_{10}(Y_{12})$, of the hadronic system after the tau-lepton is removed.
- $cos(q\bar{q} - angle)$ for the hadronic system after the tau-lepton is removed.
- $-Q_\tau cos\theta(P_{rest})$.
- The rest-of-event mass after the tau-lepton has been removed.
- $\mathcal{B}_{evt}$.

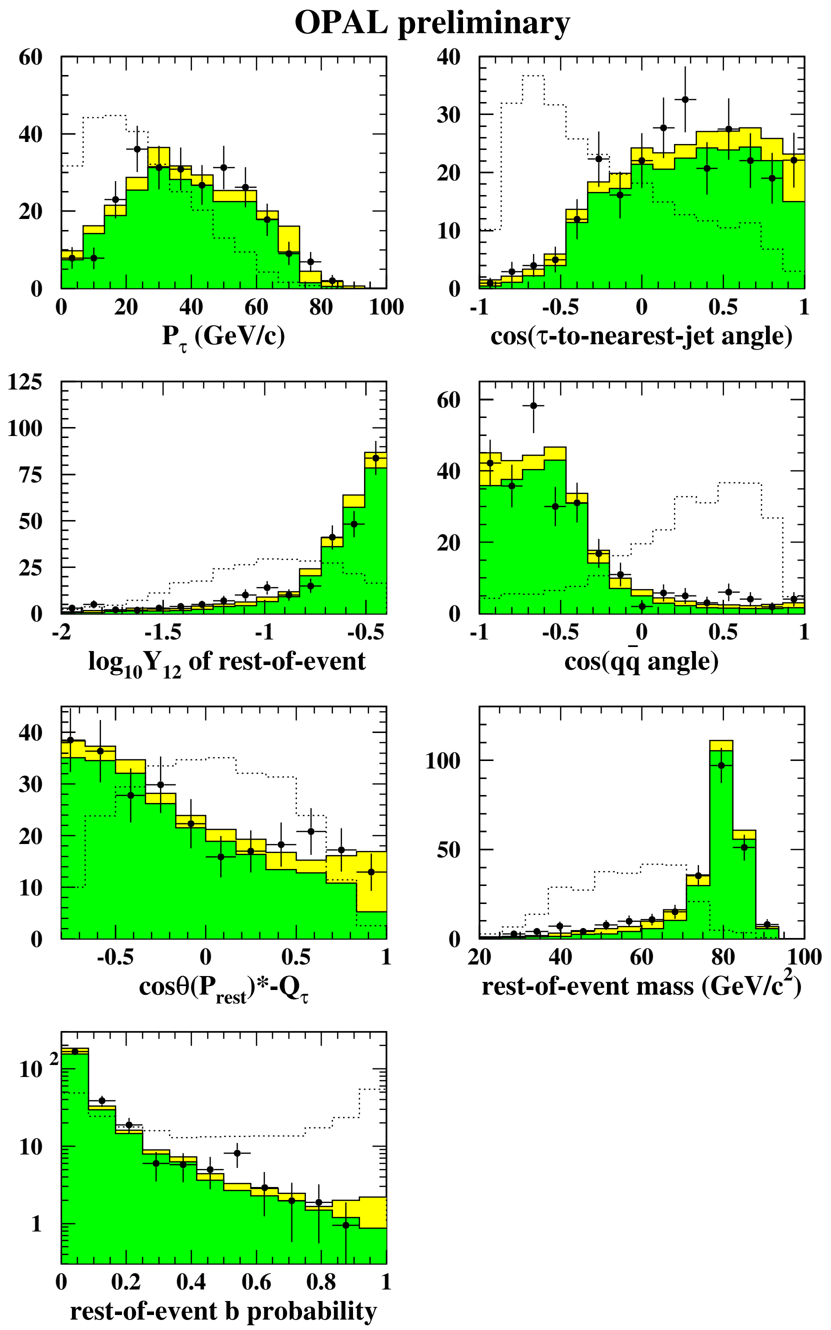

Figure 8.2: *The distribution of reference variables used in the low mass tau likelihood at a centre-of-mass energy of 189 GeV. The total background is resolved into four fermion (dark shaded) and two fermion (light shaded) components. The dotted line shows the superposition of simulated signal distributions scaled up for visibility.*

Figure 8.2 shows the reference distributions for the $\sqrt{s}$ =189 GeV low mass tau analysis and in figure 8.3 the final likelihood distribution is shown. A likelihood cut of 0.9 is used retaining 13 candidates and 6.1 background events after the likelihood cut. A slight excess is obtained after the final likelihood selection. An efficiency of 52% is achieved for a $m_{\mathrm{H}}{}^{\pm} =$ 60 GeV/c^2 and $m_{\mathrm{A}}{}^0 =$ 30 GeV/c^2. The efficiency function is shown in figure 8.4.

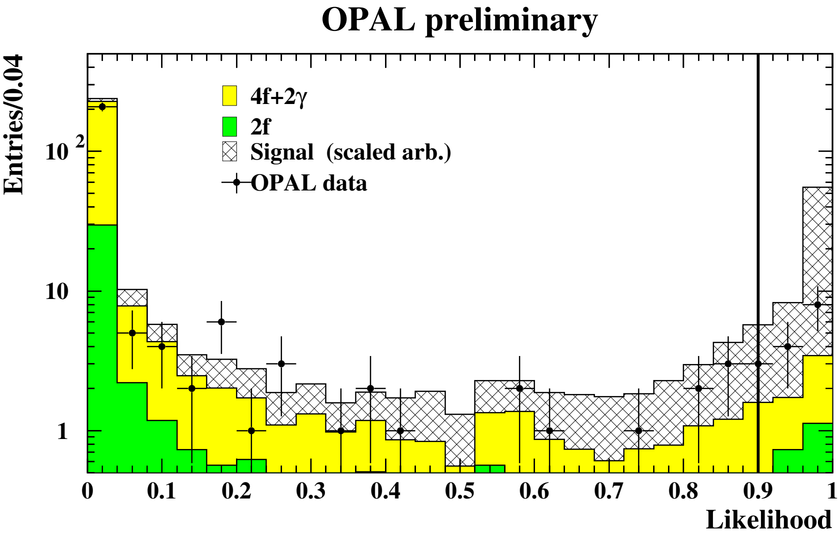

Figure 8.3: *The likelihood distribution for the low mass tau analysis at a centre-of-mass energy of 189 GeV. The dark shaded region is the two fermion likelihood, the light shaded region is the four fermion likelihood and the hatched region is the likelihood distribution expected for signal which is scaled arbitrarily. The points show the data. The vertical line shows the applied cut.*

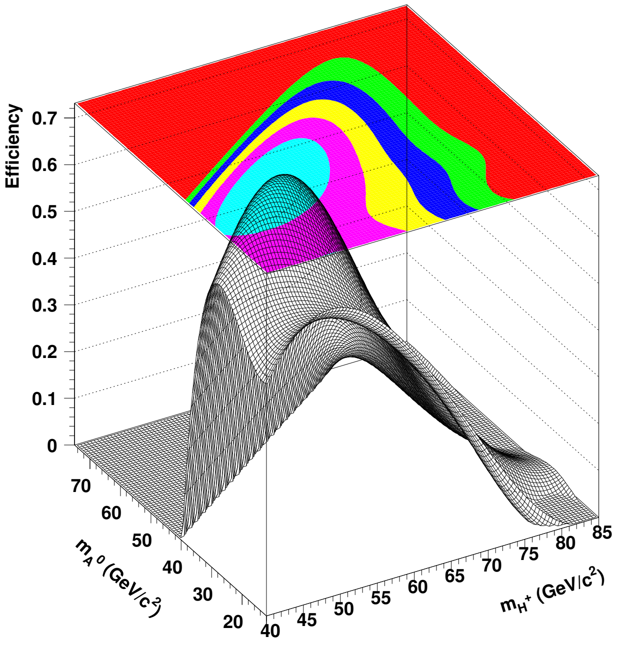

Figure 8.4: *The efficiencies of the tau signal in the low mass tau event selection at a centre-of-mass energy of 189 GeV against* $m_{H^\pm}$ *and* m_{A^0}. *The grey bands in the top plane demonstrate qualitatively the regions of equal efficiency.*

8.2 Search at $\sqrt{s}$ =192-206 GeV

8.2.1 The Preselection

The low mass regions are sufficiently covered by the analyses at $\sqrt{s}$ =189 GeV for the calculation of lower mass bounds of the charged Higgs bosons. Therefore, the analyses at higher centre-of-mass energies focus more on regions for intermediate and high $m_{H^\pm}$. Considering the branching-ratios in the 2HDM model I, the hadronic and leptonic search channels are important for the exclusion of intermediate and high $m_{H^\pm}$ regions, while the tau search channel is important for low and intermediate $m_{H^\pm}$ regions. Therefore, in the tau search channel at $\sqrt{s}$ =192-206 GeV, only one analysis was kept just as for the other two channels. However, most variables of the low mass analysis at $\sqrt{s}$ =189 GeV analysis are used, instead of those the high-mass analyses as in the other two channels and the analysis was optimised for $m_{H^\pm}$ >60 GeV/c^2. Furthermore, the cut on $E_{forward}$ is no longer used as the discriminating power was not outstanding in the $\sqrt{s}$ =189 GeV analysis (see table 8.1) and a cut on $\sqrt{s'}$ was added to be more sensitive on two-fermion events with initial-state-radiation. The following variables were used:

- The event has to meet the requirement of a multi-hadronic event.
- $\sqrt{s'}$ >120 GeV for $\sqrt{s}$ =192-202 GeV and $\sqrt{s'/s}$ >0.55×206 GeV for $\sqrt{s}$ =206 GeV.
- $N^{\tau}_{ANN} \geq 1$.
- $E_{vis}/\sqrt{s} < 0.85$.
- $|\cos\theta(P_{miss})| < 0.9$.
- $-Q_{\tau} cos\theta(P_{rest}) >$ -0.8.
- $log_{10}(Y_{23}) > -2.76$
- $N^{ch}_{jet} \geq 1$, after τ removal.
- $P_{transverse} > 14$ GeV/c.

A data to background comparison at each stage of the preselection is shown in tables 8.2 and 8.3. Good agreement between data and background events is achieved with efficiencies of 60% for $m_{H^\pm}$ = 60 GeV/c^2 and m_{A^0} = 30 GeV/c^2. The distributions of the variables are shown in figure 8.5 and 8.6 for $\sqrt{s}$ =192-202 GeV and $\sqrt{s}$ =206 GeV, respectively.

Tau Channel $\sqrt{s}$ =192-202 GeV						
Cut	Data	Total bkg.	2-fermi	4-fermi.	2-photon	Signal Eff. (%) $m_{\mathrm{H}} = 60$ GeV/c^2 $m_{\mathrm{A}} = 30$ GeV/c^2
hadronic event	20831	20765.2	16254.2	4228.4	282.6	97.6
$\sqrt{s'}$	9981	9846.8	6311.0	3453.5	82.3	83.2
≥ 1 τ candidate	3072	2764.9	882.7	1839.0	43.2	70.6
$E_{vis}/\sqrt{s} < 0.85$	1695	1586.3	422.3	1125.4	38.6	65.6
$\lvert\cos\theta(P_{miss})\rvert < 0.9$	1184	1143.9	171.2	963.4	9.3	63.2
$-Q_\tau \cdot \cos\theta(P) > -0.8$						
after τ removal	957	907.2	139.2	760.4	7.6	62.4
$\log_{10} Y_{23} > -2.76$						
after τ removal	762	697.0	107.5	582.3	7.2	62.0
$P_T > 14$ GeV/c	**626**	**578.9**	50.7	528.0	0.2	**60.2**

Table 8.2: *The number of data and Monte Carlo events at each stage of the preselection for the tau channel for $\sqrt{s}$ =192-202 GeV and the efficiency for the tau signal events with $m_{H^\pm} = 60$ GeV/c^2 and $m_{A^0} = 30$ GeV/c^2 (for $\sqrt{s} = 200$ GeV).*

Tau Channel $\sqrt{s}$ =206 GeV						
Cut	Data	Total bkg.	2-fermi	4-fermi.	2-photon	Signal Eff. (%) $m_{\mathrm{H}} = 60$ GeV/c^2 $m_{\mathrm{A}} = 30$ GeV/c^2
hadronic event	18135	18446.1	13978.4	4172.4	295.3	95.8
$\sqrt{s'}$	9512	9650.5	5959.3	3574.1	117.1	86.4
≥ 1 τ candidate	2961	2806.5	839.4	1914.5	52.6	73.8
$E_{vis}/\sqrt{s} < 0.85$	1723	1698.5	444.4	1205.8	48.3	70.2
$\lvert\cos\theta(P_{miss})\rvert < 0.9$	1150	1177.5	163.7	1001.2	12.6	67.2
$-Q_\tau \cdot \cos\theta(P) > -0.8$						
after τ removal	892	908.1	128.5	771.0	8.6	67.0
$\log_{10} Y_{23} > -2.76$						
after τ removal	706	683.8	97.9	578.5	7.4	67.0
#ch. tracks/jet						
after τ removal	680	659.6	85.7	568.6	5.3	65.8
$P_T > 14$ GeV/c	**579**	**573.3**	48.8	523.2	1.3	**65.4**

Table 8.3: *The number of data and Monte Carlo events at each stage of the preselection for the tau channel for $\sqrt{s}$ =206 GeV, and the efficiency for the tau signal events with $m_{H^\pm} = 60$ GeV/c^2 and $m_{A^0} = 30$ GeV/c^2.*

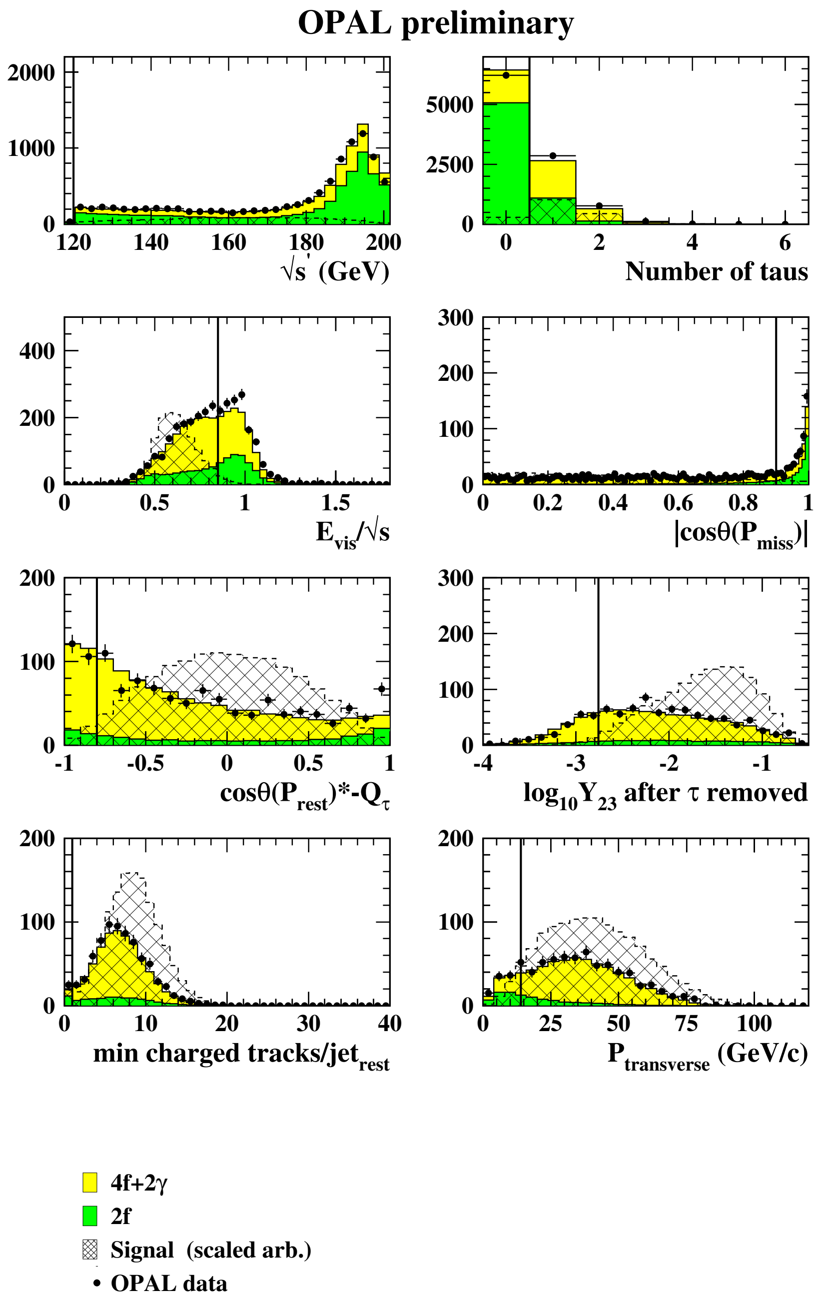

Figure 8.5: *A comparison of the distribution of data (filled circles) and Monte Carlo simulation at each stage of the tau channel preselection for* $\sqrt{s}$ *=192-202 GeV. The total background is resolved into two fermion (dark shaded) and four fermion (light shaded) components. The hatched area shows the superposition of simulated signal distributions scaled up for visibility. The vertical lines show the applied cuts.*

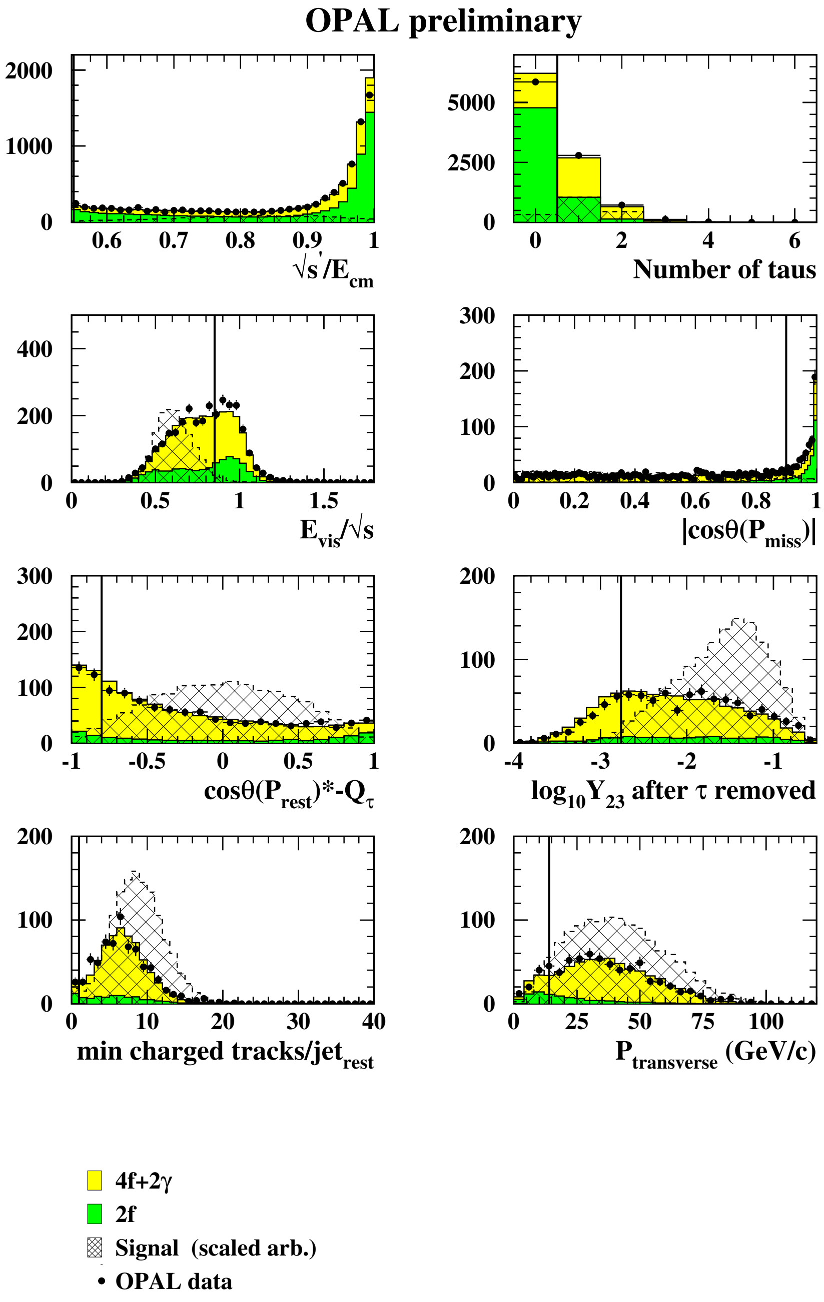

Figure 8.6: *A comparison of the distribution of data (filled circles) and Monte Carlo simulation at each stage of the tau channel preselection* $\sqrt{s}$ *=206 GeV. The total background is resolved into two fermion (dark shaded) and four fermion (light shaded) components. The hatched area shows the superposition of simulated signal distributions scaled up for visibility. The vertical lines show the applied cuts.*

8.2.2 The Likelihood-Selection

The following variables are used in the likelihood selection.

- The momentum of the tau-lepton, P_{τ}.
- $cos(\tau - to - nearest - jet - angle)$.
- $log_{10}(Y_{12})$, of the hadronic system after the tau-lepton is removed.
- $cos(q\bar{q} - angle)$ for the hadronic system after the tau-lepton is removed.
- $-Q_{\tau}cos\theta(P_{rest})$.
- The rest-of-event mass after the tau-lepton is removed.
- $\mathcal{B}_{evt}$.

The distributions of the reference variables are shown in figure 8.7 and figure 8.8 for $\sqrt{s}$ =192-202 GeV and $\sqrt{s}$ =206 GeV, respectively. An overall agreement between data and background distributions is achieved. The likelihood distributions are shown in figure 8.9(a) and 8.9(b) at $\sqrt{s}$ =192-202 GeV and $\sqrt{s}$ =206 GeV, respectively. 9 data candidates survive the selection with 8.9 expected background events at $\sqrt{s}$ =192-202 GeV, while 6 data candidates were selected with 5.9 expected background events for $\sqrt{s}$ =206 GeV.

A signal efficiency of 41% is achieved for $m_{H^{\pm}}$ = 60 GeV/c^2 and m_{A^0} = 30 GeV/c^2 of 41% at $\sqrt{s}$ =200 GeV and 43% at $\sqrt{s}$ =206 GeV. The efficiency function of the analysis at $\sqrt{s}$ =206 GeV is shown in figure 8.10. The results are summarised in table 8.4.

Tau Channel $\sqrt{s}$ =192-206 GeV					
$\sqrt{s}$ in GeV	Data	Total bkg.	2-fermi	4-fermi.	Signal Eff. (%) m_{H} = 60 GeV/c^2 m_{A} = 30 GeV/c^2
192-202	9	8.9	0.9	8.0	**40.8** at $\sqrt{s}$ =200 GeV
206 (200-209)	6	5.9	0.6	5.3	**42.8** at $\sqrt{s}$ =206 GeV
total	**15**	**14.8**	1.5	13.3	

Table 8.4: *The number of data and Monte Carlo events after the likelihood selection for the tau channel and the efficiency for the tau signal events with* m_{H^+} = 60 *GeV/*c^2 *and* m_{A^0} = 30 *GeV/*c^2 *for* $\sqrt{s}$ *=192-202 GeV (data taken in the year 1999 between 192-202 GeV) and 206 GeV (data taken in the year 2000 for 200-209 GeV with a luminosity weighted mean of 206 GeV).*

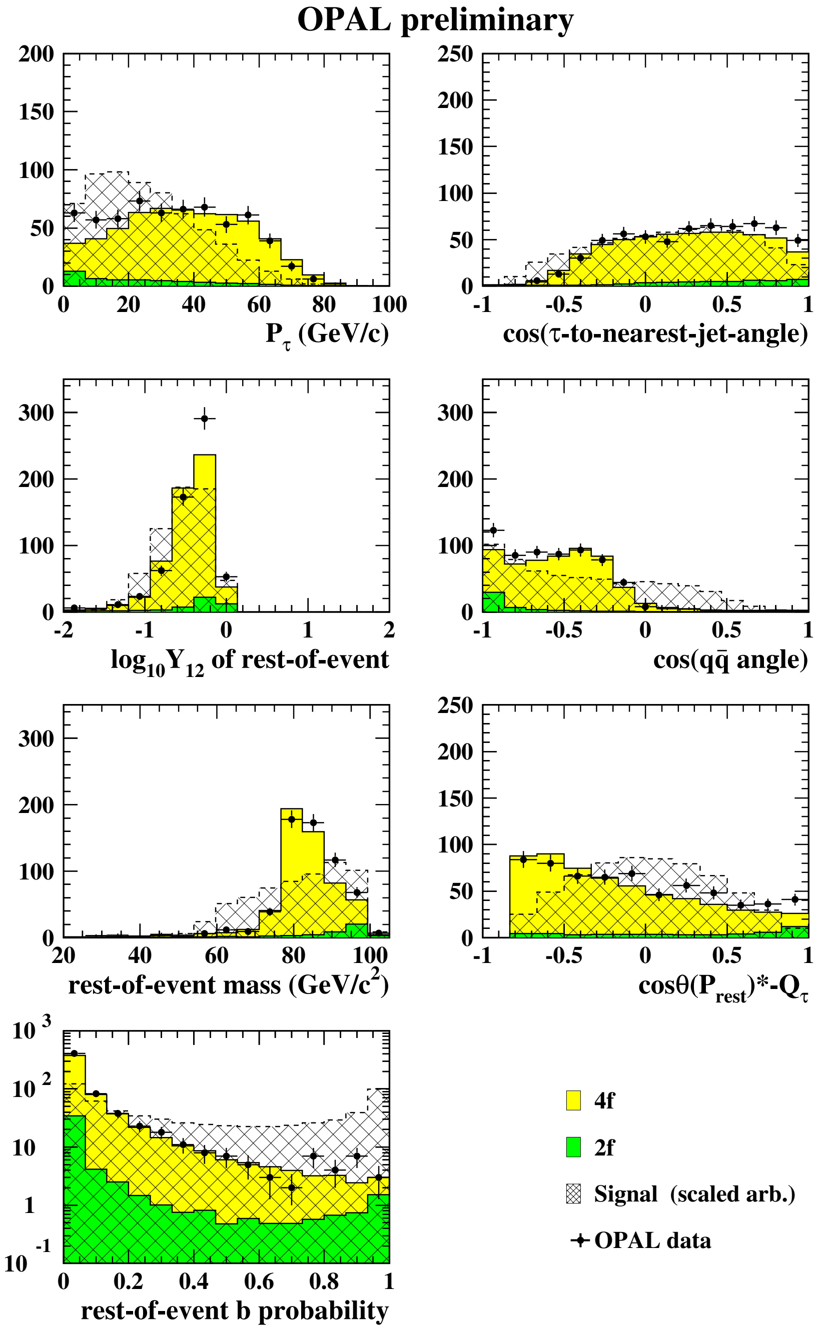

Figure 8.7: *The distribution of reference variables used in the tau likelihood for* $\sqrt{s}$ *=192-202 GeV. The total background is resolved into two fermion (dark shaded) and four fermion (light shaded) components. The dashed line shows the superposition of simulated signal distributions scaled up for visibility.*

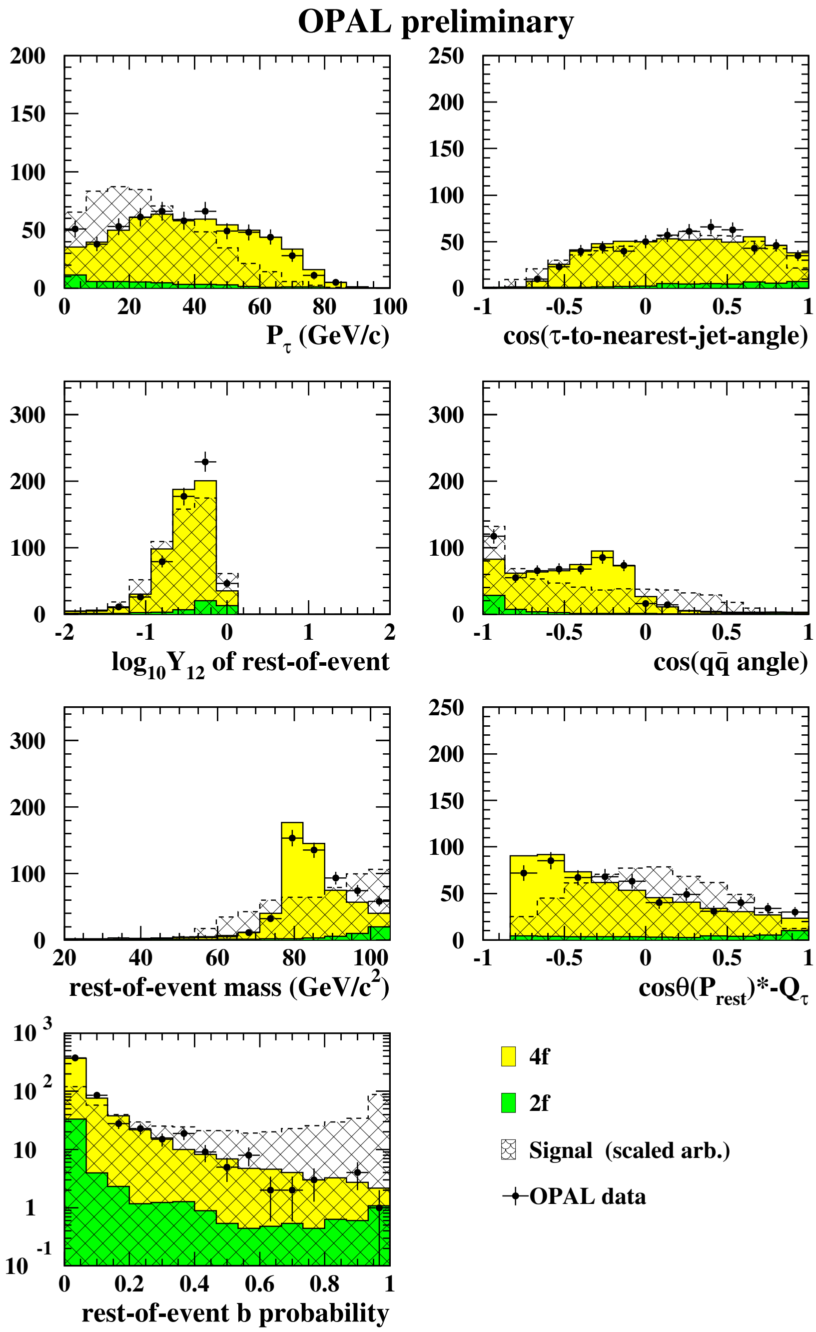

Figure 8.8: *The distribution of reference variables used in the tau likelihood for* $\sqrt{s}$ *=206 GeV. The total background is resolved into two fermion (dark shaded) and four fermion (light shaded) components. The dashed line shows the superposition of simulated signal distributions scaled up for visibility.*

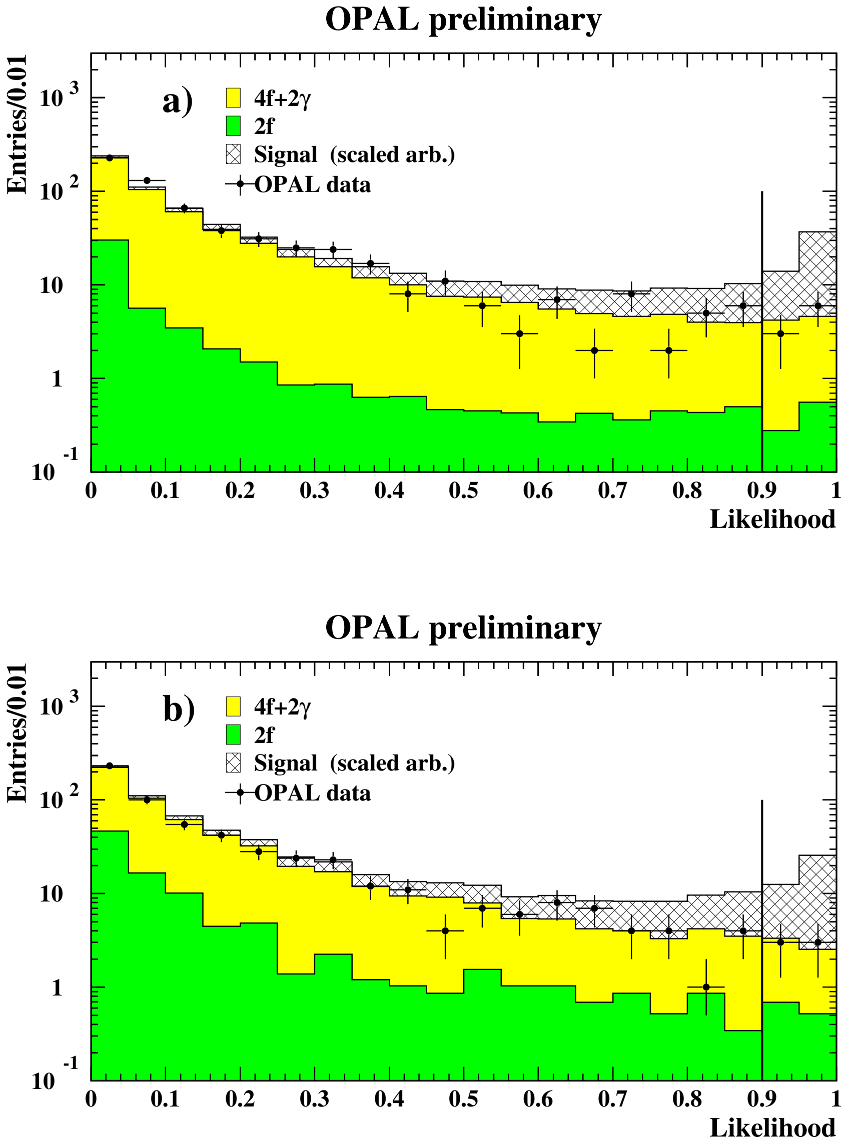

Figure 8.9: *The likelihood distribution for the tau analysis at a centre-of-mass energy of a) 192-202 GeV and b) 206 GeV. The dark shaded region is the two-fermion likelihood, the light shaded region is the four-fermion likelihood and the hatched region is the likelihood distribution expected for signal which is scaled arbitrarily. The points show the data. The vertical line shows the applied cuts.*

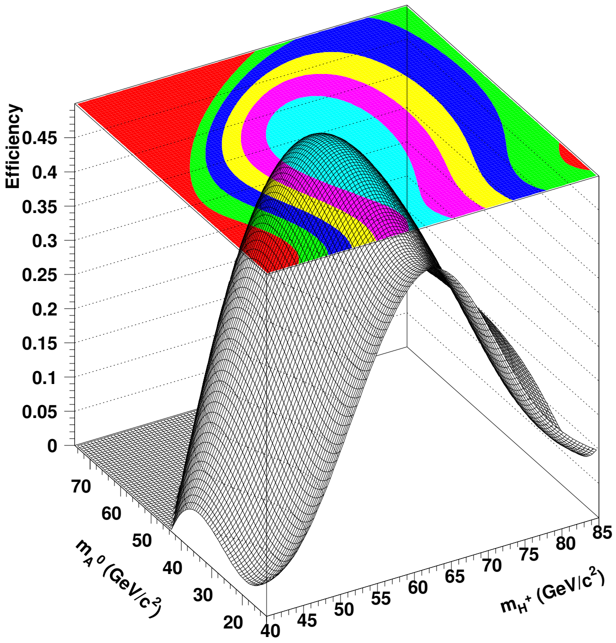

Figure 8.10: *The efficiencies of the tau signal events in the tau event selection at a centre-of-mass energy of 206 GeV against the charged and CP-odd Higgs mass. The grey bands in the top plane demonstrate qualitatively the regions of equal efficiency.*

Chapter 9

Systematics Checks

The discussion of the errors is divided into two parts. The first part discusses the statistical error of the different event samples based on the limited number of simulated events. In the second part systematic effects, like experimental resolution effects or uncertainties in the models used for the generation of the background events are discussed.

The systematic errors are estimated in the following way[1]. The reference distributions are kept from the original analyses and are used to analyse new alternative background and and in some cases signal event samples. These were generated with applied changes based on the investigated error source. A new likelihood value is then calculated for each event of the alternative sample. The difference in numbers passing the likelihood cut compared to the original numbers, are taken as the systematic uncertainties. For simplification, the uncertainty on the signal efficiency was estimated for a specific mass combination ($m_{H^{\pm}}$;m_{A^0}), per centre-of-mass energy, and this uncertainty was applied to every mass point. The systematic uncertainties for $\sqrt{s} = 192 - 206$ GeV were estimated with the 206 GeV sample[2].

9.1 Statistical Error

The uncertainty in the limited number of simulated events is estimated by the binomial error for the efficiency and for the number of background events remaining after preselection. The derived *relative errors in percent* are shown together with the other systematic errors investigated for the signal efficiency, for $m_{\mathrm{H}}{}^{\pm} = 50\ GeV/c^2; m_{\mathrm{A}}{}^{0} = 25\ GeV/c^2$ in table 9.1 for $\sqrt{s}$ =189 GeV. The numbers for the error on the background events are also shown in percent. The errors are below 10%, independent of the search channel, with $4 - 6\%$ for the signal efficiency and $4 - 8\%$ for the number of background events. Table 9.2 shows the statistical errors for $\sqrt{s} = 206\ GeV$. The errors are below 10%, with $4 - 5\%$ for the signal efficiency and $5 - 9\%$ for the background events.

9.2 Systematic Errors

9.2.1 Monte Carlo Generators

The generation of the partons and the following hadronisation of the quarks involved, is a source for systematic error effects. Especially the higher order jet resolution parameters are sensitive to the fragmentation model used. Moreover, multi-gluon radiation is only approximately contained in the models and uncertainties in the fragmentation can influence the multi-jet character.

Alternative background samples, which differ in the generation of partons and/or in the fragmentation model, were used to estimate this uncertainty (see section 4.1 for a description

---

[1] A full investigation of the possible uncertainties is not done since it would have been too time consuming.

[2] Correctly, this estimation should be done for every mass point at every centre-of-mass energy.

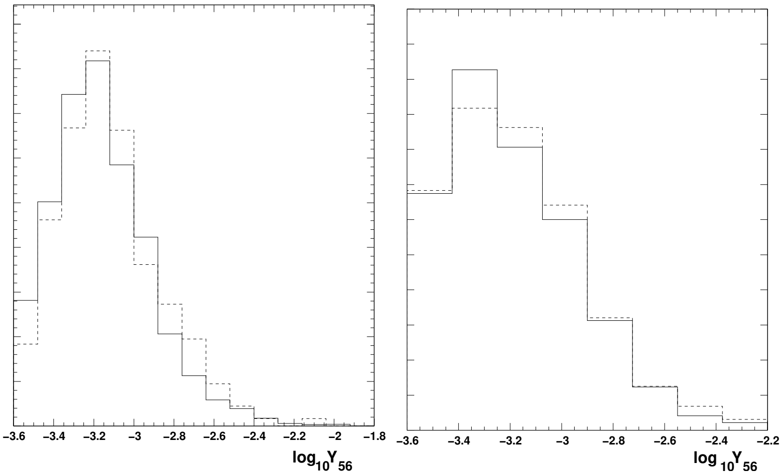

Figure 9.1: *The distribution of* $log_{10}Y_{56}$ *for two-fermion background in the hadronic analysis at* $\sqrt{s}$ *=189 GeV (left diagram) and* $\sqrt{s}$ *=206 GeV (right diagram). The solid histogram is produced with the PYTHIA event generator (for* $\sqrt{s}$ *=189 GeV) and KK2f generator (for* $\sqrt{s}$ *=206 GeV). The dashed histogram is produced with the HERWIG generator.*

of the various event generators). The background samples of the two-fermion background was originally produced with PYTHIA ($\sqrt{s} = 189$ GeV) and KK2f ($\sqrt{s} = 192 - 206$ GeV). Alternatively HERWIG was used for the two-fermion production to investigate the influence due different parton and different fragmentation model used. The simulation of the four-fermion events was originally done GRC4F. The event generator EXCALIBUR was alternatively used for the production of the four-fermion events to estimate the systematic effect of a different parton generator model used for in the production of four-fermion sample. The systematic error in the two- and four-fermion samples were investigated at the same time. The difference in numbers between the standard background sample and the alternative sample after the applied likelihood cut is taken as the systematic uncertainty on the MC generators.

As shown in table 9.1 this error source dominates all others at $\sqrt{s} = 189$ GeV reaching a maximal values of 36% (for the low mass hadronic event selection).

Figure 9.1 shows a comparison of $log_{10}(Y_{56})$ obtained with different generators, for the two fermion background at $\sqrt{s} = 189$ GeV (left diagram) and $\sqrt{s} = 206$ GeV (right diagram). The diagrams show the distribution obtained after the preselection, in the hadronic event selections. The dashed histograms are the jet resolution parameters derived with the HERWIG event generator and the solid histograms show the ones for PYTHIA and KK2F for $\sqrt{s}$ =189 GeV and $\sqrt{s}$ =206 GeV, respectively. Differences in the distributions can be seen. They are smaller at the higher centre-of-mass energy. They can affect the likelihood selections and thereby the final selected number of events, especially if more than one jet resolution parameter is used in the selection. The reduction of the number of jet resolution parameters in the analyses at the higher centre-of-energies (right diagram) therefore also lowers the systematic uncertainty of the background modelling. The uncertainty at $\sqrt{s} =$ 206 GeV is about 10% in the hadronic and leptonic search channel and about 5% in the tau search channel as illustrated in table 9.2.

9.2.2 Track Smearing

The correct simulation of the track resolution is of great importance for the classification of the events through the b-tagging algorithm, since it is based on reconstructing secondary vertices. An overestimation or underestimation of the resolution can produce wrong secondary vertices and other parameters entering the b-tagging. The effect could be a deficit or excess in data compared to background events after the final event selection. To investigate this effect the resolution of the important track parameters for the b-tagging $d0$, ϕ and $z0$ (see appendix A.1) have been varied by +5%, all at the same time. The difference in signal efficiency and expected background numbers after the likelihood cut, compared to the default selected numbers, is taken to be the systematic uncertainty for this error source.

Table 9.1 shows the results for the $\sqrt{s}$ =189 GeV analyses and table 9.2 illustrates the effects seen for the higher centre-of-mass energies (evaluated at $\sqrt{s}$ =206 GeV). These uncertainties are the second biggest error source at $\sqrt{s}$ =189 GeV with 10−18% for the background events and up to 5% for the signal efficiency, at $m_{\mathrm{H}}{}^{\pm} = 50\ GeV/c^2$ and $m_{\mathrm{A}}{}^{0} = 25\ GeV/c^2$. At $\sqrt{s}$ =192-206 GeV the errors are the biggest systematic effect for the background events with $23 - 36\%$ and $2 - 4\%$ for the signal efficiency, at $m_{\mathrm{H}}{}^{\pm} = 60\ GeV/c^2$ and $m_{\mathrm{A}}{}^{0} = 30\ GeV/c^2$.

Source		Hadronic Channel	Leptonic Channel	Tau Channel
		low-mass sel.	low-mass sel.	low-mass sel.
Background Modelling	sig. eff.	–	–	–
	N_{bkg}	36.4%	16.8%	9.8%
MC Statistics	sig. eff.	4.6%	3.7%	3.7%
	N_{bkg}	6.7%	3.7%	8.3%
Track resolution	sig. eff.	5.3%	0.4%	4.5%
	N_{bkg}	10.4%	9.0%	18.1%
B Multiplicity	sig. eff.	0.8%	0.2%	1.0%
	N_{bkg}	0.8 %	2.5%	0.0%

Table 9.1: Relative systematic effects in percent in the signal efficiencies and expected background numbers after the likelihood cut for $\sqrt{s}$ =189 GeV. The change is shown in percent for the low mass analysis in the three different channels. The signal efficiencies are stated for $m_{H^\pm} = 50$ GeV/c^2 and $m_{A^0} = 25$ GeV/c^2.

Source		Hadronic Channel	Leptonic Channel	Tau Channel
Background Modelling	sig. eff.	–	–	–
	N_{bkg}	10.2%	10.0%	5.4%
MC Statistics	sig. eff.	3.8%	4.6%	5.2%
	N_{bkg}	4.9%	5.2%	8.9%
Track smearing	sig. eff.	2.1%	4.1%	2.4%
	N_{bkg}	36.0%	26.0%	22.6%

Table 9.2: Relative systematic errors in percent for the signal efficiencies and expected background after the likelihood cut in percent for the three different channels at 206 GeV. The signal efficiencies are stated for $m_{H^\pm} = 60$ GeV/c^2 and $m_{A^0} = 30$ GeV/c^2.

9.2.3 b-Hadron charged Multiplicity

The correct simulation of the b-hadron charged multiplicity (n_B) is essential for the classification of the events in the b-tagging algorithm. Improvements in the knowledge of the b-hadron charged decay multiplicity opposed to the default value used in the MC event generation are taken into account in the analyses by reweighting the MC events [50, 60]. These reweighted numbers are used as signal efficiencies and expected background numbers for the setting of excluded regions at $\sqrt{s}$ =189 GeV. The systematic uncertainty on the b-Hadron charged multiplicity was estimated by varying the decay multiplicity within $n_B = 4.955 \pm 0.062$ [50]. The error was found to be small as shown in table 9.1. At the higher centre-of-mass energies a common error of 3% was assumed for the error on the b-Hadron charged multiplicity.

9.2.4 Summary

The error on the MC statistics is in the same range for all centre-of-mass energies as shown in tables 9.1 and 9.2. The analyses at 192-206 GeV are more stable against different generator models for the bacground samples than the 189 GeV analyses possibly due to the reduction of used jet-resolution parameters in the analyses and the reduction of correlation effects. The error on the track smearing is higher for the higher centre-of-mass energies.

For the setting of excluded mass regions with the $\sqrt{s}$ =189 GeV analyses, the errors on the number background events were added in quadrature for the combined error uncertainty on the number of background events. At $\sqrt{s}$ =192-206 GeV the errors are used separated by source. The statistical error are taken to be uncorrelated to the other error sources. The systematic errors are taken to be fully correlated between channels and centre-of-mass energies.

Chapter 10

Statistical Method

After analyzing the observed data for each channel at each centre-of-mass energy the results are interpreted. Do they favour the SM without an excess of signal events, e.g. a charged Higgs boson, or do they show hints on the existence of new physics? The statistical method used, the incorporation of systematic errors and the correct combination of different channels have to be studied. In the following an outline of the statistical method is given. For a more detailed description see [61, 62, 63].

10.1 Confidence Levels

The simplest information derived from an analysis is the number of expected background events, the signal efficiency, for a given Higgs mass, and the number of observed events which were selected by the analyses. Instead of having just this one-bin-information, e.g. the number of events after a likelihood cut, a finer binning can be chosen, ordering the candidates according to their probability of being a signal event in a distinguishing variable. In our case, the distribution of the likelihood values after the applied likelihood cut is used for the calculation of excluded mass regions. The signal and background events of the analyses assign each data candidate a certain weight, $w(\mathcal{L})$, which can be done in different ways. The fractional event counting method [61, 62] defines the weight according to

$$w(\mathcal{L}) = \frac{s(\mathcal{L})}{s(\mathcal{L}) + 2b(\mathcal{L})}, \tag{10.1}$$

where $s(\mathcal{L})$ and $b(\mathcal{L})$ are the distributions for the expected number of signal and background events binned in the likelihood distributions. An *estimator* X_{obs} is assigned to the whole data sample by summing over the weights of all candiates in the data sample[1]. The value for the estimator derived with the observed data, X_{obs}, is then compared to the distribution of the same estimator based on a large number of simulated *gedanken experiments* in which the presence of a signal is assumed, a *signal-and-background hypothesis* (s+b) and estimator based on the hypothesis of *background-only* (b) events. These distributions are shown in figure 10.1. The estimator in the plot is chosen in such a way that signal-and-background hypothesis is preferred if X_{obs} is located on the right side of the diagram and the background-only hypothesis if it is located on the left side.

A *Confidence Level* can then be derived for the whole sample from the probability density function of X, $P(X)$

$$CL = \int_0^{X_{obs}} P(X) \cdot dX. \tag{10.2}$$

---

[1] See [61, 62] for the handling of the combination of search channels.

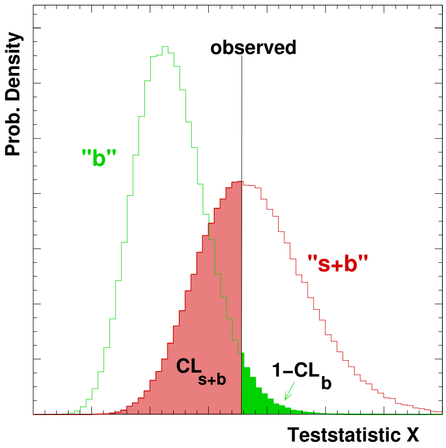

Figure 10.1: *The distribution of P_{s+b} and P_b for a certain parameter-space point and the estimator X_{obs} observed in data. The axis of the estimator is chosen in such a way, that the probability of the signal-and-background hypothesis increases with increasing X. The very dark shaded region corresponds to $1 - CL_b$ and grey shaded region to the CL_{s+b} values.*

The probability to derive $X \leq X_{obs}$ in a signal-and-background ensemble is given by

$$CL_{s+b} = P_{s+b}(X \leq X_{obs}). \tag{10.3}$$

Classical definitions exclude a point in the scanned parameter-space with $1 - CL_{s+b}$ [64]. However, equation 10.3 is not complete because one is interested in the confidence level for a signal assuming the correct behaviour of the expected background events according to the SM, both in total number and in distributions. To account for this, a probability is defined for an ensemble of background events according to

$$CL_b = P_b(X \leq X_{obs}). \tag{10.4}$$

A normalised, approximate, *signal* probability can then be defined as

$$CL_s = CL_{s+b}/CL_b. \tag{10.5}$$

By definition, CL_{s+b} is a measure for the *compatibility* of the observed data sample with the signal-and-background hypothesis while $1 - CL_b$ is a measure for the *incompatibility* with the background-only hypothesis.

The parameter space (in our case the $(m_{H^\pm}; m_{A^0})$ plane) is then scanned and a signal hypothesis is excluded with a confidence level of 95% if the scanned point yields to $CL_s < 0.05$. Regions with $CL_s > 0.05$ are allowed at a 95% CL. The point of the 5% position marks the highest excluded Higgs mass value and thus the lower mass bound.

The expectation value of the normalised signal probability $< CL_s >$ is obtained by averaging over a large number of *gedanken experiments* where the observed number of candidates is varied according o the background-only hypothesis. This value is a measure for the sensitivity of the results and the aim is to maximise it. The probabilities above can also be obtained analytically.

Note that, in the limit of high rates, the choice of the weight as defined in equation 10.1 minimises the average $< CL >$ for an arbitrary set of background experiments if analyzed in terms of signal-and-background. It also maximises the average confidence level, if signal-and-background events are analyzed in terms of background-only and thereby gives the best average separation between a background model and a signal-and-background model [62].

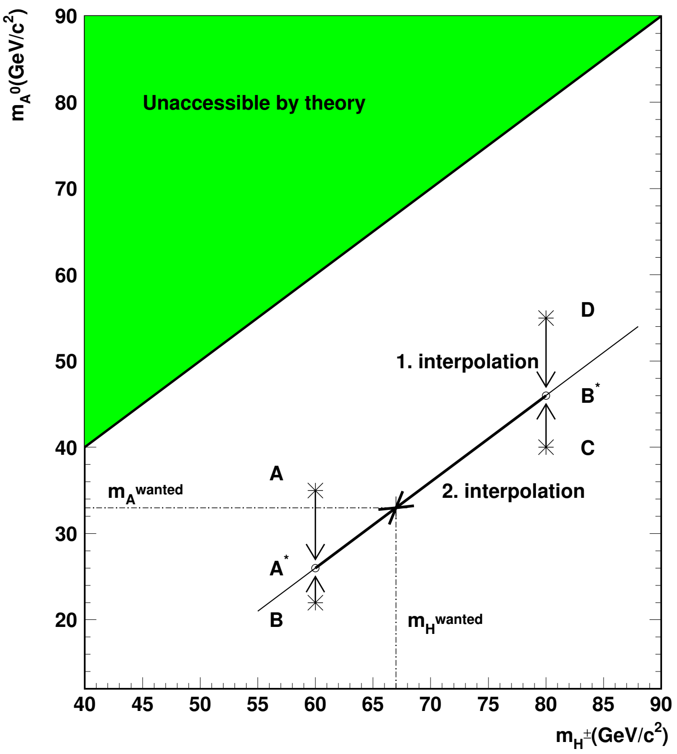

Figure 10.2: *Interpolation method for a mass point ($m_{H^\pm}^{wanted}$,$m_{A^0}^{wanted}$). The available likelihood distributions for the signal events exist for the four points marked by stars (A, B, C and D). First an interpolation to the cross-point of a line intersecting the mass point and being parallel to the function of $m_{H^\pm} - m_{A^0}$ =const. curve is done. Then a second interpolation to the actual mass point is made.*

10.2 Limit setting Procedure

An event-counting method using a one-bin distribution (the events passing the likelihood cut) is used for all three W^*-mediated channels at $\sqrt{s}$ =189 GeV. The same method is used for the W^*-mediated tau channel, for all energies.

To reach a higher sensitivity and exclusion power, the inputs to the limit calculation for the hadronic and leptonic channel, at $\sqrt{s}$ =192-206 GeV, are handled differently. The binned likelihood distributions of the events surviving the applied likelihood cut are used. A single likelihood distribution is used for the expected background and observed data for all Higgs masses, since they do not depend on the Higgs mass. However, the signal likelihood distributions dependent on the mass point ($m_{H^\pm}$;m_{A^0}). They are, however, only available for a fixed number of points at which the signal was generated. To obtain the distribution for any mass pair an interpolation method, illustrated in figure 10.2, is used.

To obtain the likelihood distribution for an arbitrary mass point ($m_{H^\pm}^{wanted}$;$m_{A^0}^{wanted}$) a function is calculated intersecting the wanted mass point and satisfying $m_{H^\pm} - m_{A^0}$ =const. A similar behaviour in the likelihood distributions is assumed for points with a constraint mass difference. The likelihood signal distributions at A and B are then interpolated to A' and the likelihood distributions at B and C are interpolated to B'. A second interpolation of the likelihood distributions at A' and B' to the actual mass point ($m_{H^\pm}^{wanted}$;$m_{A^0}^{wanted}$) is then made, weighting the two distributions with their distance to the point.

Chapter 11

Interpretation of the Results and lower Mass Bounds

Two different approaches are taken. First, a model independent interpretation is made assuming a pair of charged scalars, $e^+e^- \to S^+S^-$. Regions are excluded in the two-dimensional mass plane ($m_{S^\pm}$;m_{S^0}) at a 95% CL. The plane is scanned in steps of 200 MeV/c^2 to 1 GeV/c^2 in both masses and the limit setting procedure is performed at every mass point. As theoretical input, only the production cross-section for the production of a pair of charged scalars is used. The region above the diagonal $m_{S^0} > m_{S^\pm}$ is unaccessible due to kinematic constraints of the charged scalar decaying into the S^0 (see figure 10.2). The product of all branching-ratios leading to a final decay state is fixed to a number between 0 and 1 and the excluded regions are given only for a specific search channel. These limits are valid for any pair of charged scalars having the analysis specific characteristics, i.e. decaying into a virtual W boson and a S^0 decaying furthermore into a pair of b quarks.

In the second approach, the results are interpreted assuming the 2HDM model I. Regions are excluded in the two-dimensional mass plane ($m_{H^\pm}$;m_{A^0}) at a 95% CL for $tan\beta = 1$, 10, 100 and 1000. The expected number of signal events is calculated explicitly in the 2HDM model I for each channel and at every Higgs mass point.

11.1 Model-independent Results

The results are given in a parameter scenario for a neutral and a charged scalar, $e^+e^- \to S^+S^-$. The excluded regions are calculated based on the results of the hadronic, leptonic and tau selection separately. The expected number of signal events per mass point and centre-of-mass energy is then given by

$$s_{expect}(m_{S^0}, m_{S^\pm}) = \mathcal{L} \cdot \epsilon(m_{S^0}, m_{S^\pm}) \cdot \sigma(m_{S^\pm}) \cdot \prod BR_i, \tag{11.1}$$

where $\mathcal{L}$ is the luminosity of the data sample, σ the production cross-section for a pair of charged scalars which is computed with HZHA [35]. A function $\epsilon = \epsilon(m_{S^\pm}; m_{S^0})$ is used to estimate the expected signal efficiency for an arbitrary point in the the mass plane ($m_{S^\pm}$;m_{S^0}). These functions are created with a spline-fit method from the limited number of mass points and are shown in chapters 6 to 8 for the different channels. The charged scalars are assumed to decay according to the signal in the corresponding search channel, e.g. $S^+S^- \to W^*A^0W^*A^0 \to q\bar{q}'b\bar{b}q''\bar{q}'''b\bar{b}$, in the hadronic search channel. $\prod Br_i$, is the product of all the branching-ratios leading to a given final state which is fixed to 1.0, 0.5 and 0.4, since there is no theoretical model assumed and thus no specific information for the branching-ratios available. The 95% CL excluded regions are shown in figure 11.1 for the hadronic event selection (upper left diagram), the leptonic event selection (upper right diagram) and the tau event selection (lower diagram). The results of the analyses at $\sqrt{s}$ =192-206 GeV and those of the low mass analyses at $\sqrt{s}$ =189 GeV are used for the calculation of the excluded regions.

The hadronic event selection excludes the widest mass plane ranging above $m_{S^\pm} = 90$ GeV/c^2. The results from the leptonic search channels can exclude less parameter space due to the smaller signal efficiency in this channel. The results of the tau channel are shown in the lower diagram. The highest excluded charged scalar mass is about 82.5 GeV/c^2. The difference in shape of the latter one compared to the other two search channels arises from the use of the event-counting method for all energies for the tau search channel.

These excluded regions can be used to test alternative theoretical models. Assume a model which predicts $\prod BR_i$ =0.4 for a sample of signal events. If the signal events behave kinematically like $e^+e^- \rightarrow S^+S^- \rightarrow W^*S^0W^*S^0 \rightarrow q\bar{q}'b\bar{b}q''\bar{q}'''b\bar{b}$, the excluded regions of the hadronic search channel, as shown in upper left diagram of figure 11.1, can be used to test the predictions.

One has to be careful though, in the interpretation of the exclusion limits. There can of course be an overlap in the selections which can result in a double-counting of the chosen number of expected signal, background and observed data events. Events selected by the hadronic event selection can also be selected in the leptonic selection, for example. The correct calculation of the overlap must take into account the relative contribution of each channel in the theoretical model.

11.2 Mass Limits within the 2HDM Model I

In this section the search results are interpreted within the 2HDM model I. Again, the mass plane is scanned and at each step the limit setting procedure is repeated. The expected number of signal events is then

$$s_{expect}(m_{A^0}, m_{H^\pm}, tan\beta) = \mathcal{L} \cdot \epsilon(m_{A^0}, m_{H^\pm}) \cdot \sigma(m_{H^\pm}) \cdot \prod BR_i(m_{A^0}, m_{H^\pm}, tan\beta), \quad (11.2)$$

where s_{expect} is also dependent on $tan\beta$. $\prod BR_i(m_{A^0}, m_{H^\pm}, tan\beta)$ is calculated in the context of the 2HDM model I [17].

The search channels which contribute in the 2HDM model I are the W^*-mediated channels (as discussed in chapters 6 to 8). These nearly exhaust the full decay-width of the charged Higgs bosons for $tan\beta > 100$ and $m_{H^\pm} - m_{A^0} > 10$ GeV/c^2. For regions of $tan\beta < 10$ and near the kinematical boundary, the direct-fermionic channels[1] of the charged Higgs bosons also contribute considerably. These channels have been analyzed in the context of another work [44, 65, 6]. For the calculation of the excluded regions the direct-fermionic search results were included as input to the limit setting procedure.

11.2.1 The Overlap between the Selections

When combining the results from the different search channels, care must be taken to treat possible double-counting of the events correctly. The event sample chosen by the tau selection is essentially independent of the samples chosen by the hadronic and leptonic selections. Likewise, the overlap between the selections based on the direct-fermionic decays of the charged Higgs boson and those based on the W^*-mediated decays is negligible. The contributions of the signal events in the mass plane in the 2HDM model I is different for these samples. The direct-fermionic decays contribute mainly near $m_{H^\pm} = m_{A^0}$ and at low $tan\beta$ values, while the W^*-mediated decays are the most important ones at high $tan\beta$ values and for intermediate and high $m_{H^\pm} - m_{A^0}$.

In contrary to this, there is a large overlap between the samples chosen by the hadronic selections and leptonic selections. To assure that every event is counted only once, the

---

[1] Direct-hadronic channel: $H^+ \rightarrow c\bar{s}$, $H^- \rightarrow \bar{c}s$. Direct-semi-leptonic channel: $H^+ \rightarrow c\bar{s}$, $H^- \rightarrow \tau\nu$. Direct-leptonic channel: $H^+ \rightarrow \tau\nu$, $H^- \rightarrow \tau\nu$.

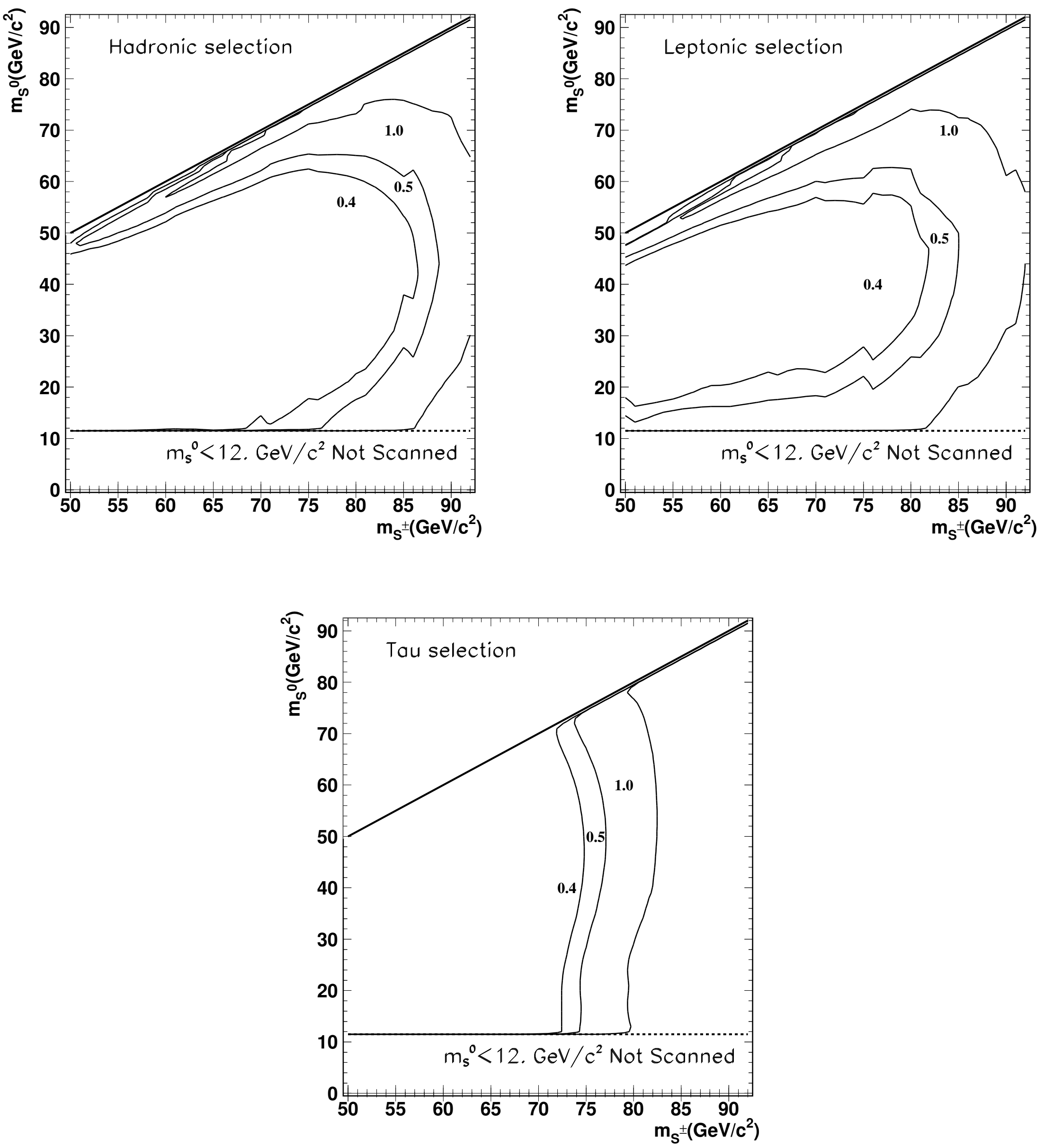

Figure 11.1: *Limits for* $\prod BR_i$ *(*$\sqrt{s} = 189 - 206$ *GeV) in the (*$m_{S^\pm}$*;*m_{S^0}*) plane for the hadronic selection (top left), leptonic selection (top right) and tau selection (bottom). The lines show the boundaries for the excluded regions at a* 95% *confidence level.*

two selections are divided into three samples. a) those events chosen only by the *hadronic selection*, b) those events chosen only by the *leptonic selection* and c) the sample of *overlap* events, i.e. events chosen by the hadronic and leptonic selection. These events were treated in the following way: If the hadronic likelihood value is larger than the leptonic one, $\mathcal{L}_{had} > \mathcal{L}_{lep}$, the hadronic likelihood was assigned to the event and the leptonic one is discarded. Likewise for the case $\mathcal{L}_{lep} > \mathcal{L}_{had}$, the leptonic likelihood was assigned to the event. Thus each event is treated exactly once.

In case of the signal events the hadronic signal events are also send through the leptonic selection and vice versa. Figure 11.2 shows the efficiencies of events selected by only the hadronic event selection (at $\sqrt{s}$ =206 GeV). The left diagram shows the hadronic signal efficiency and the right diagram the leptonic one. The corresponding efficiencies for events passing only the leptonic selection (at $\sqrt{s}$ =206 GeV) are shown in figure 11.3. As shown the efficiency of the signal events to pass only one selection is small (10% to 20%). The efficiencies obtained for an event to pass the overlap selection (at $\sqrt{s}$ =206 GeV), are shown in figure 11.4. Table 11.1 shows the number of data events for $\sqrt{s}$ =192-206 GeV selected by the hadronic, leptonic and overlap selection. As noted the overlap is substantial. The overlap was not taken into account for the results of the searches at $\sqrt{s}$ =189 GeV. These analyses showed a smaller overlap than those at $\sqrt{s}$ =192-206 GeV, probably because the number of similar likelihood variables used in the two analyses was smaller.

	Hadronic Sel.	Leptonic Sel.	Overlap
$\sqrt{s}$ =192-202 GeV	16	16	17
$\sqrt{s}$ =206 GeV (200-209 GeV)	9	8	15

Table 11.1: The number of data events passing only the hadronic, leptonic or passing both selections for the analyses at $\sqrt{s}$ =192-202 GeV (year 1999) and $\sqrt{s}$ =206 GeV (200-209 GeV; year 2000).

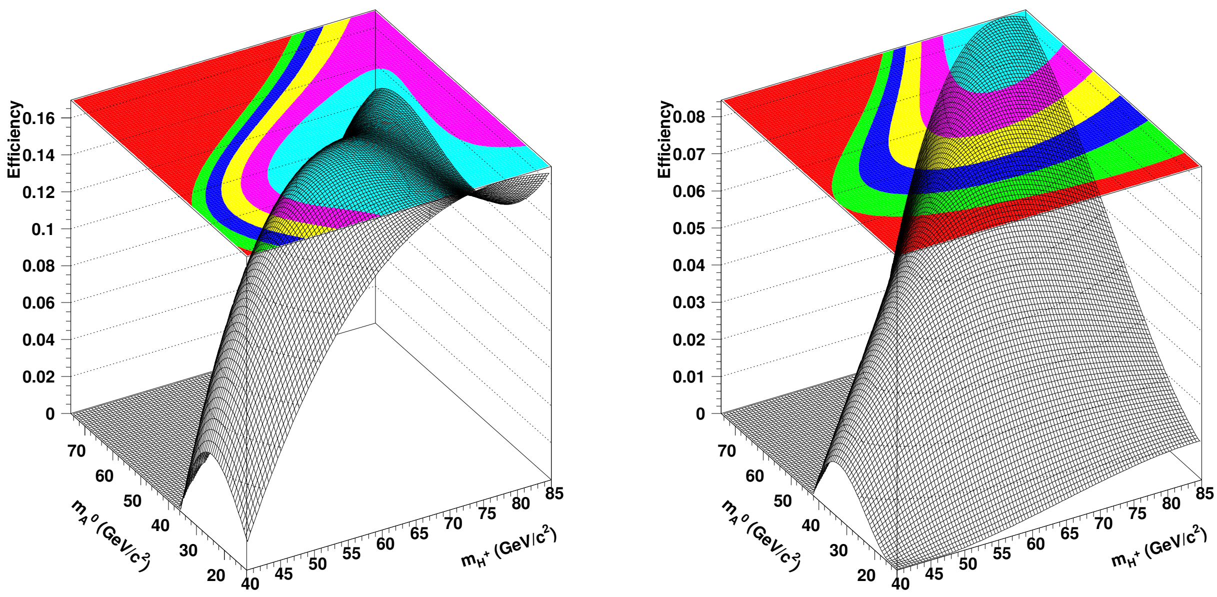

Figure 11.2: *The efficiencies of the signal passing only the hadronic event selection at a centre-of-mass energy of 206 GeV against* $m_{H^\pm}$ *and* m_{A^0}*. Left: the hadronic signal events, right: the leptonic signal events. The grey bands demonstrate qualitatively the regions of equal efficiency.*

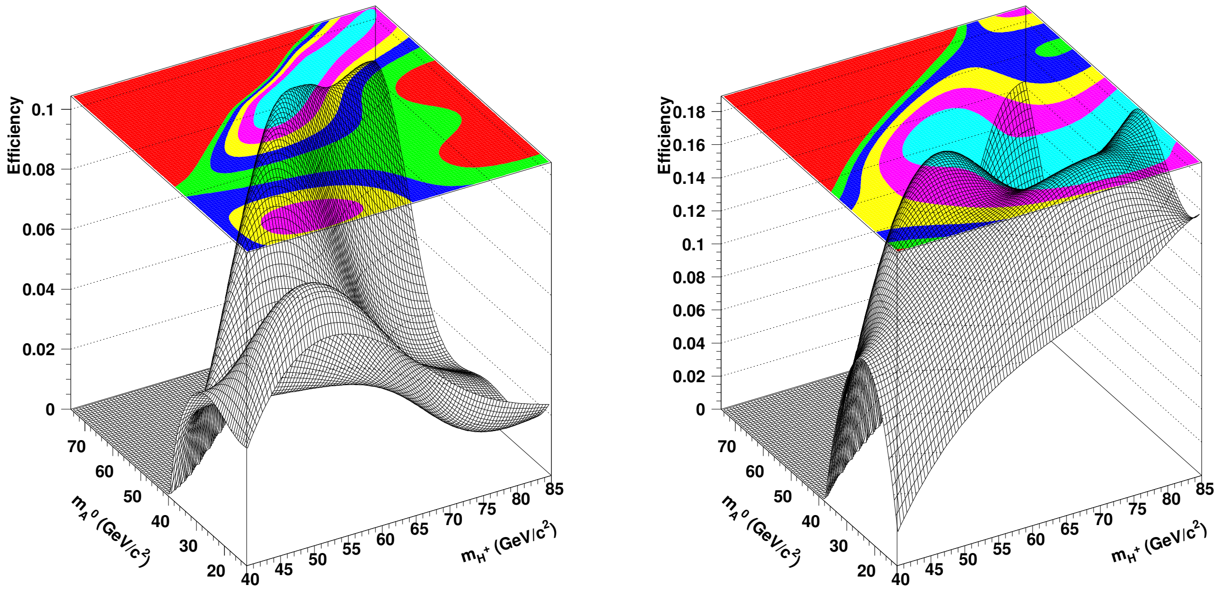

Figure 11.3: *The efficiencies of the signal passing only the leptonic event selection at a centre-of-mass energy of 206 GeV against* $m_{H^\pm}$ *and* m_{A^0}*. Left: the hadronic signal events, right: the leptonic signal events. The grey bands demonstrate qualitatively the regions of equal efficiency.*

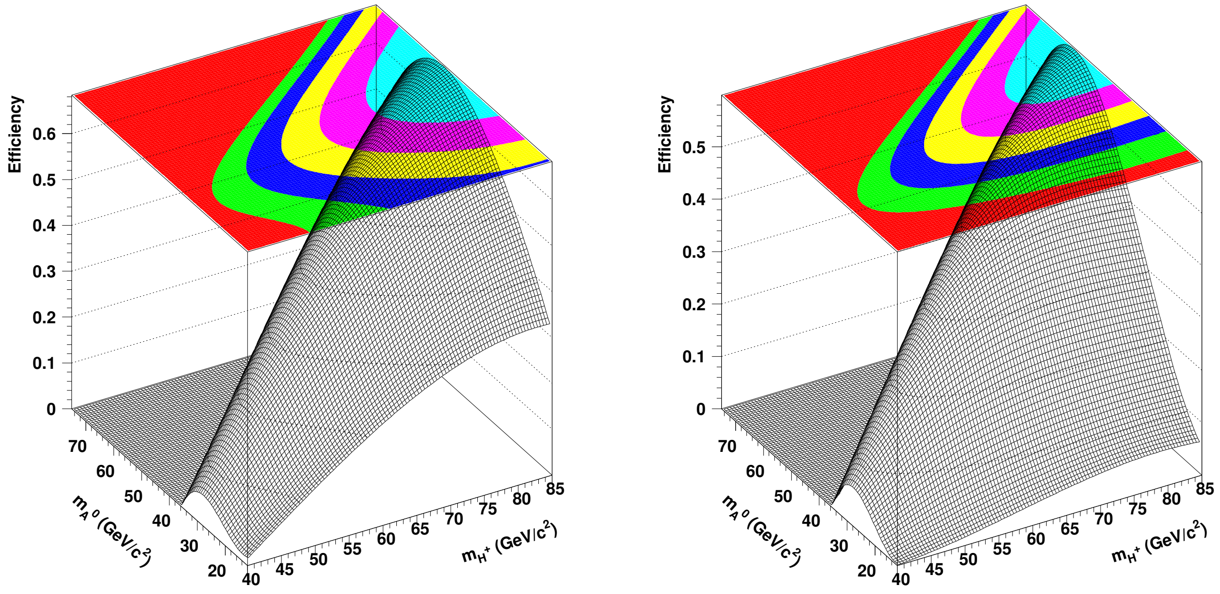

Figure 11.4: *The efficiencies of the signal passing both event selections at a centre-of-mass energy of 206 GeV against* $m_{H^\pm}$ *and* m_{A^0}*. Left: the hadronic signal events, right: the leptonic signal events. The grey bands demonstrate qualitatively the regions of equal efficiency.*

11.2.2 Mass Bounds

The excluded regions obtained for the 2HDM model I by the limit setting procedure are presented for $\sqrt{s}$ =189 GeV in figure 11.5, with systematic errors in the observed limits, and figure 11.6, without systematic errors in the observed limits[2], for $tan\beta$=1, 10, 100 and 1000 [8]. No systematic error handling is applied to the expected limits. The regions below $m_{A^0} < 12$ GeV/c^2 are not scanned due to b quark production-threshold.

At $tan\beta = 1$ (upper left diagram of figure 11.5) the mass limits reach a m_{A^0}-independent behaviour, for high m_{A^0}. The excluded regions near the kinematically boundary arise mainly from the direct-fermionic search channels, as these are the most important channels in the 2HDM model I in this region [17]. Regions with $m_{H^\pm}$ <58 GeV/c^2, are excluded independent of m_{A^0}. At intermediate $tan\beta$ values ($tan\beta = 10$; upper right diagram) no lower mass bound can be set on $m_{H^\pm}$ independent of m_{A^0}. At high $tan\beta$ values ($tan\beta = 100$; lower left diagram) a narrow excluded region near the kinematical boundary (m_{A^0}=$m_{H^\pm}$) is observed and a region excluded by the low mass analyses for $m_{H^\pm} \lesssim 50$ GeV/c^2 and 12 GeV/c^2 < m_{A^0} <32 GeV/c^2 is visible. There is only a small change in the excluded regions when going to $tan\beta$=1000 (lower right diagram).

The excluded regions without systematic errors are shown in figure 11.6. At $tan\beta$ =100 and 1000 regions excluded by the high mass analyses are now visible at 55 GeV/ $c^2 < m_{H^\pm} <$ 70 GeV/c^2. They vanish when the systematic errors are applied. At $tan\beta$ = 10 the high mass selection does not contribute in the expected region, due to a slight excess of events in data candidates [8].

In figure 11.7, the mass bounds calculated for all energies investigated are shown, i.e. for the data at 189 GeV, 192-202 GeV (year 1999), and 206 GeV (200-209 GeV; year 2000). The corresponding results from the direct-fermionic search channels of 189-209 GeV [6] are also included. The black regions are excluded at a 95% CL while the dashed lines show the

---

[2] The systematic errors were included in the observed mass limits, by reducing the number of background events by one standard deviation of their systematic error. This is a very conservative approach.

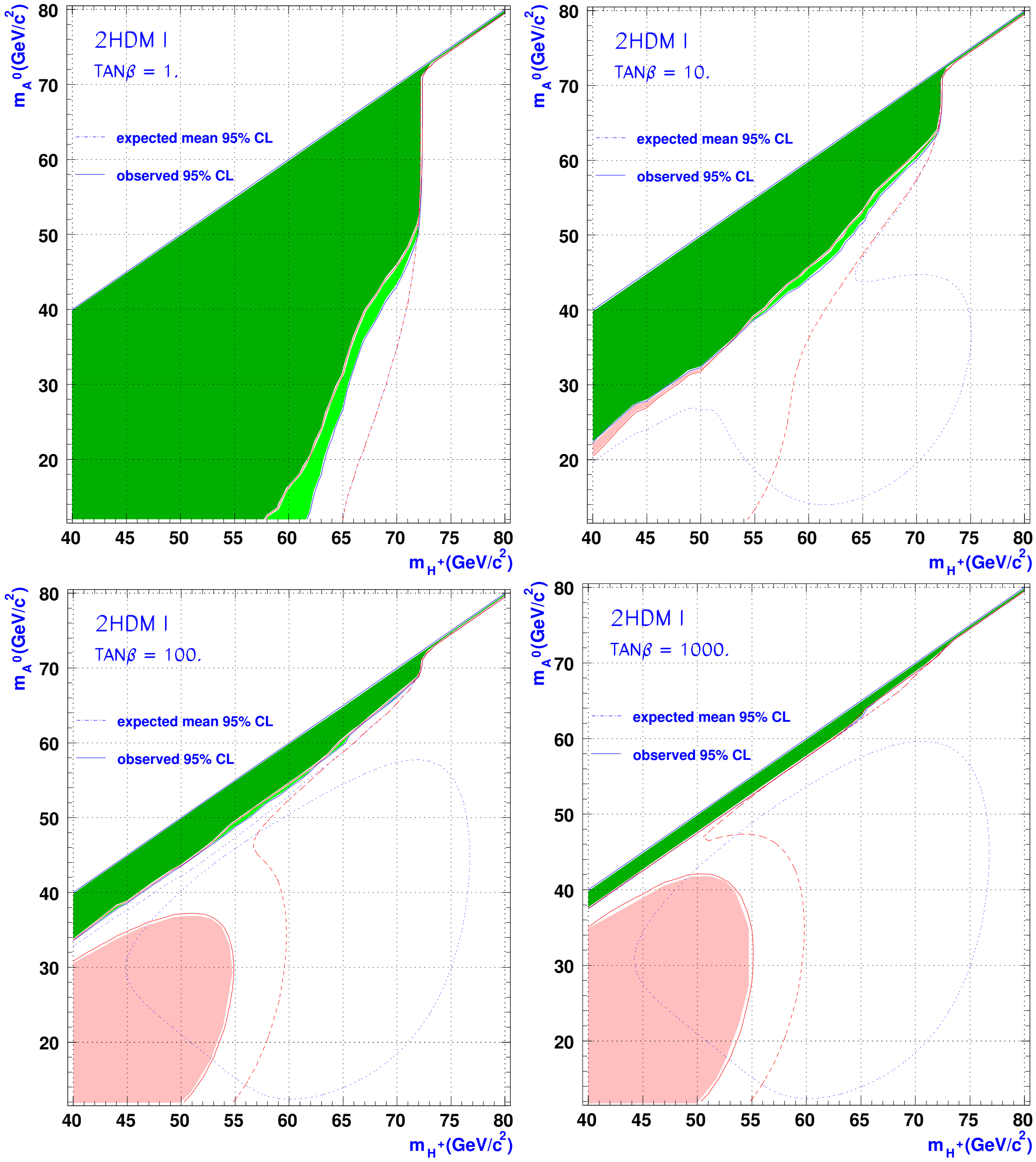

Figure 11.5: *Limits in the 2HDM model I (with systematics in the observed limits) for* $\sqrt{s} =$ 189 *GeV in the* $(m_{H^\pm}, m_{A^0})$ *plane for* $\tan\beta = 1$ *(top left),* $\tan\beta = 10$ *(top right),* $\tan\beta = 100$ *(bottom left), and* $\tan\beta = 1000$ *(bottom right). The results of the direct-fermionic decay channels (183-189 GeV [7]) are included in the calculation of the excluded regions. The very light grey shaded region (grey shaded region) is excluded at the* 95% *confidence level by the low (high) mass analysis, while the dark grey shaded region is excluded by both. The dashed (dotted) lines are the mean expected* 95% *confidence level for the low (high) mass analysis [8].*

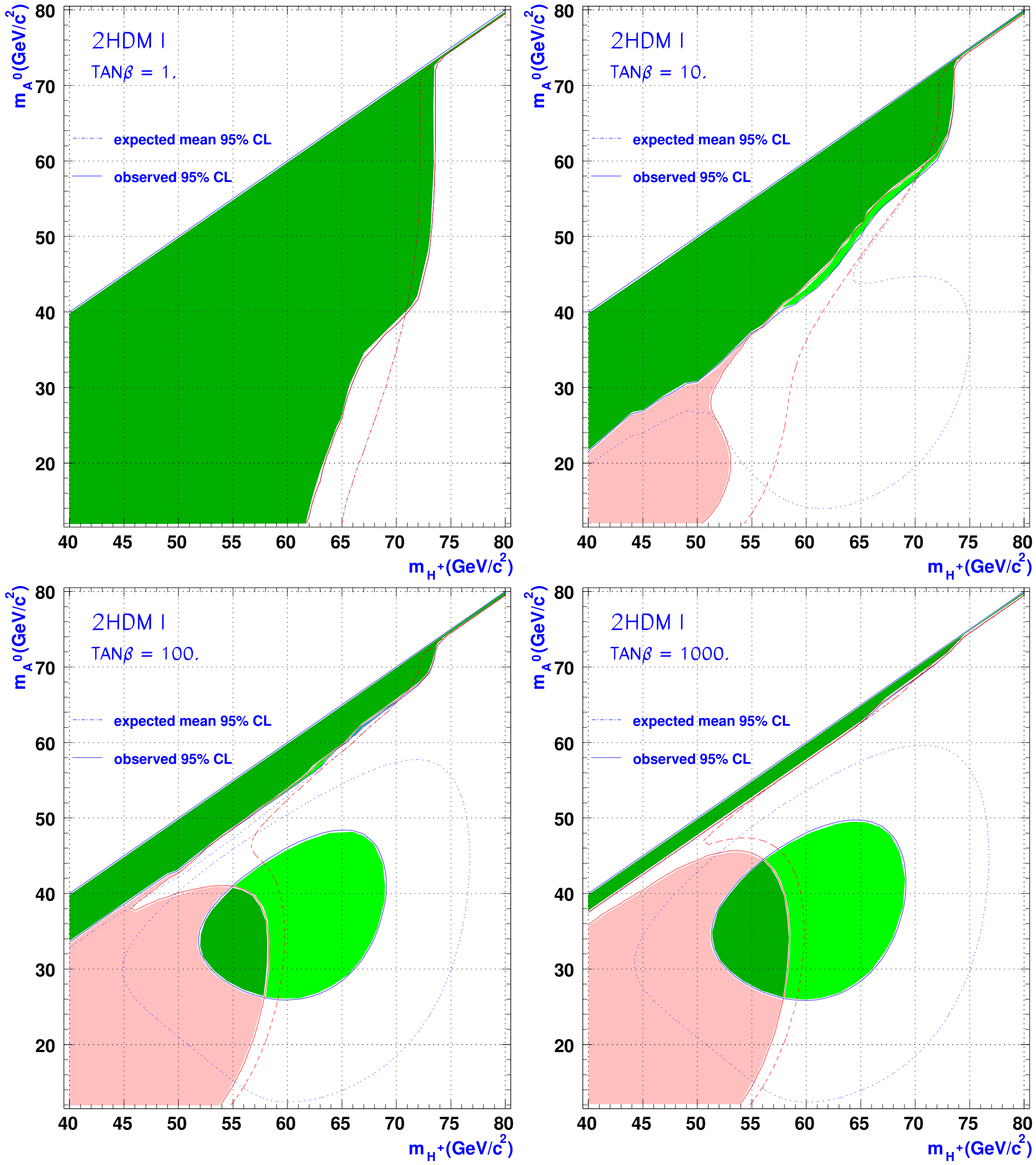

Figure 11.6: *Limits in the 2HDM model I (without systematics in the observed limits) for* $\sqrt{s} = 189$ *GeV in the* $(m_{H^\pm}, m_{A^0})$ *plane for* $\tan\beta = 1$ *(top left),* $\tan\beta = 10$ *(top right),* $\tan\beta = 100$ *(bottom left), and* $\tan\beta = 1000$ *(bottom right). The results of the direct-fermionic decay channels (183-189 GeV [7]) are included in the calculation of the excluded regions. The very light grey shaded region (grey shaded region) is excluded at the* 95% *confidence level by the low (high) mass analysis, while the dark grey shaded region is excluded by both. The dashed (dotted) lines are the mean expected* 95% *confidence level for the low (high) mass analysis [8].*

expected median confidence limits[3].

At low $tan\beta$ ($tan\beta = 1$; upper left diagram) regions with $m_{H^\pm}$ <69 GeV/c^2 are excluded independent of m_{A^0}. The highest excluded charged Higgs mass for intermediate $tan\beta$ regions ($tan\beta = 10$; upper right diagram) is $m_{H^\pm}$=89 GeV/c^2 for m_{A^0}=44 GeV/c^2. $m_{H^\pm}$=90 GeV/c^2 poses a difficult boundary to pass due to the process $\mathrm{e}^+\mathrm{e}^- \rightarrow Z^0Z^0$. Regions with $m_{H^\pm} \lesssim 70$ GeV/c^2 are excluded for nearly all m_{A^0}. There are some small gaps around m_{A^0} ≈12 GeV/c^2 and a sensitivity hole near the diagonal, which shifts to higher m_{A^0} masses for higher $tan\beta$ values ($tan\beta = 100$; lower diagram). The expected median confidence limits follow the observed confidence limits for all $tan\beta$.

The effects of the systematic errors have been investigated for a mass point near the excluded mass boundary according to the method of Cousins and Highland [66, 62][4]. Due to limitations in time, the systematic errors are not investigated in the full ($m_{H^\pm}$;m_{A^0}) plane, as it was done for 189 GeV which used a more simple treatment of systematic error handling. Instead, systematics are studied only for one point (m_{A^0} =44 GeV/c^2; $m_{H^\pm}$ =89 GeV/c^2) corresponding to the highest $m_{H^\pm}$ excluded value. The same systematic error sources were studied as for 189 GeV (see chapter 9). The mass bound is reduced by 4 GeV/c^2 from 89 GeV/c^2 to 85 GeV/c^2 when systematic errors are applied.

---

[3] $tan\beta$ =1000 is no longer calculated since there is no gain in the excluded region compared to $tan\beta = 100$.

[4] The mean value of the errors assigned to the leptonic and hadronic search channels were used for the three independent samples, while considering the overlap of the selections.

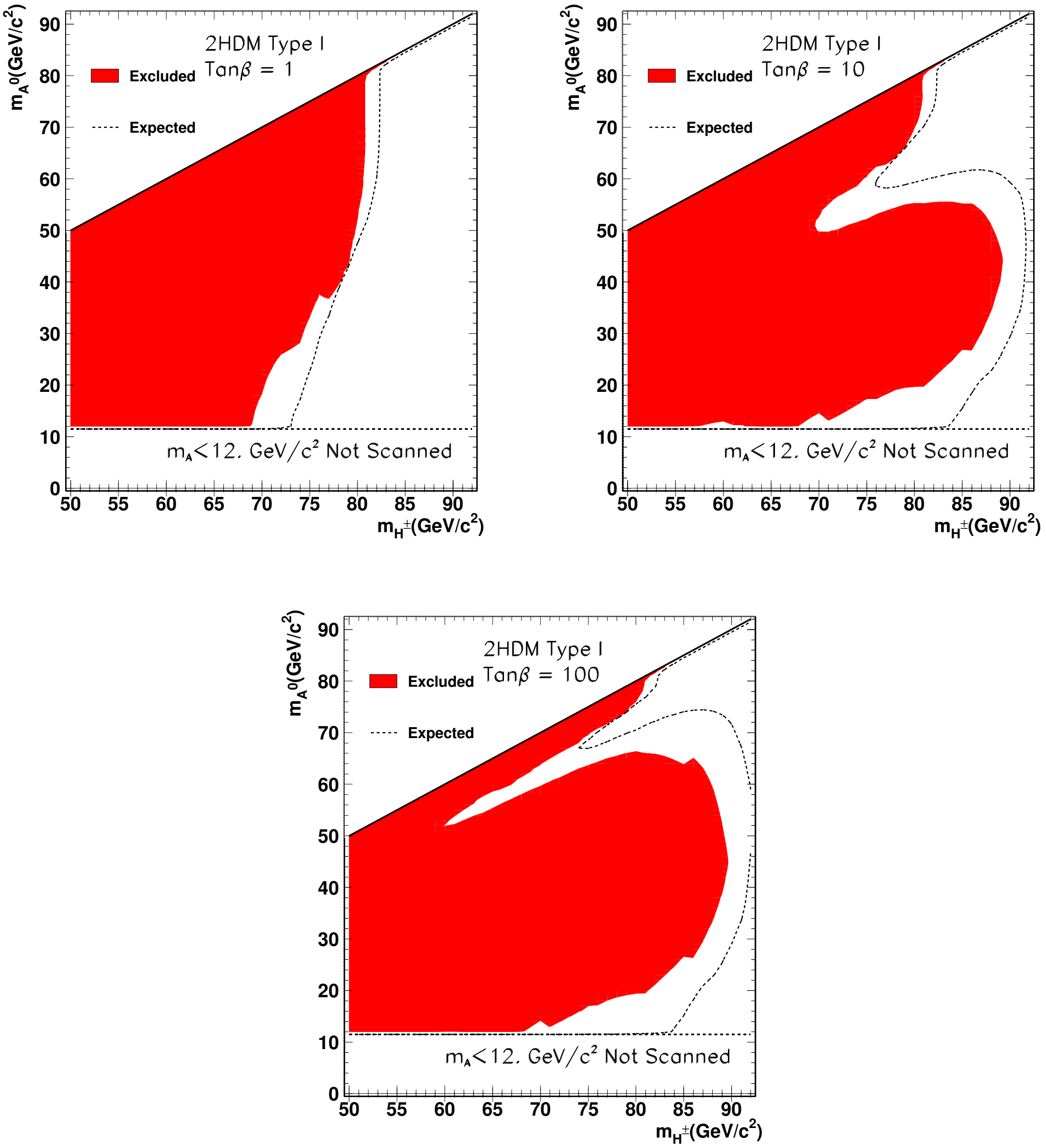

Figure 11.7: *Limits in the 2HDM model I (without systematics in the observed limits) for* $\sqrt{s}$ *=189 (low mass analyses) -206 GeV in the* $(m_{H^\pm}, m_{A^0})$ *plane for* $\tan\beta = 1$ *(top left),* $\tan\beta = 10$ *(top right) and* $\tan\beta = 100$ *(bottom). The results of the direct-fermionic decay channels (189-206 GeV [6]) are included in the calculation of the excluded regions. The grey shaded region is excluded at the* 95% *confidence level by analyses. The dashed lines are the median expected* 95% *confidence level for the analyses.*

Chapter 12

LEP Combined Results

Efforts have been made by the four LEP experiments (ALEPH, DELPHI, L3 and OPAL) to combine their results on the search for the charged Higgs boson in the context of the 2HDM models. These searches assume the direct-fermionic decays $H^+ \to c\bar{s}$ and $H^+ \to \tau\nu$ to fully exhaust the decay width of the charged Higgs boson leaving the relative branching-ratios free and assuming no specific 2HDM model or SUSY theory. The results are presented as a function of the branching ratio $\mathrm{Br}(H^+ \to \tau\nu)$. The results of the W^*-mediated search channels are not used in the combination. The predefinition of the branching-ratio $\mathrm{Br}(H^+ \to \tau\nu)$ fully determines the branching-ratios of the three possible search channels:

1. **Direct-hadronic channel**: $c\bar{s}\bar{c}s$: $H^+ \to c\bar{s}$, $H^- \to \bar{c}s$
2. **Direct-semi-leptonic-channel**: $c\bar{s}\tau\nu$: $H^+ \to c\bar{s}$, $H^- \to \tau\nu$
3. **Direct-leptonic channel**: $\tau\nu\tau\nu$: $H^+ \to \tau\nu$, $H^- \to \tau\nu$

Two different statistical approaches were used to calculate the 95% CL excluded regions in the LEP Higgs working group. They differ in the statistical procedure. The first one is based on a **likelihood ratio** approach [64]. The second one, is the **fractional event counting method** (see chapter 10 and [61, 62, 64]). Both methods have been found to be consistent with each other except in the limit of high candidate weights [62]. The likelihood ratio method is used as the standard statistical procedure for the calculation of the charged Higgs boson lower mass bounds while the fractional event counting method is used as a cross-check. The results based on the fractional event counting method were calculated in the framework of this thesis.

12.1 Individual Experiments

The number of events obtained by each experiment per search channel are shown in table 12.1. Details of the analyses can be found in [6, 67, 68, 69, 70, 7].

Experiment:	ALEPH	DELPHI	L3	OPAL
Total: Int. luminosity (pb^{-1}):	217.2	225.1	217.8	217.4
Backg. exp. / Events obs. (*)				
$(c\bar{s})(\bar{c}s)$:	997.7/968	412.8/387	883.3/961	424.2/439
$(c\bar{s})(\tau^+\nu)$:	118.0/127	190.8/173	171.8/171	203.5/224
$(\tau^+\nu)(\tau^-\bar{\nu})$:	22.0/17	23.8/ 25	49.8/44	331.7/315
Events in all channels:	1137.7/1112	627.4/585	1104.9/1176	959.4/978

Table 12.1: *Individual number of events for the* $e^+e^- \to H^+H^-$ *final states. The luminosities and numbers of events correspond to the data sets taken at energies between 200 and 209 GeV (year 2000 data). (*) The OPAL selection depends on the Higgs mass; the numbers given here correspond to* $m_{H^\pm}$ *= 80 GeV/*c^2*.*

The branching-ratio is scanned in steps of 0.05 and the charged Higgs mass is scanned in steps of 1 GeV/c^2. At each scan point the limit setting procedure is repeated. The individual results obtained with the fractional event counting method for the median expected and observed 95% CL bounds are shown in table 12.2 for Br($H^+ \to \tau\nu$)=0, Br($H^+ \to \tau\nu$)=1 and for the weakest lower mass bound. No systematic error handling is applied to the results. Table 12.3 shows the results obtained within each collaboration [6, 67, 68, 69, 70], with applied systematic error handling. There are slight differences in the lower mass bounds, between those calculated within each experiment and those shown in table 12.2. These arise from the different statistical method used. Furthermore, especially in the case of the OPAL results, the difference can also arise due to the incorporation of systematic errors.

The excluded regions are illustrated in figure 12.1 for the four experiments obtained with the fractional event counting method, corresponding to table 12.2. The results from ALEPH (top left diagram) prefer the background-only hypothesis, showing a slight deficit in data events at low branching-ratios. The observed results of the DELPHI (top right diagram) fully agree with the prediction of the background-only hypothesis. For OPAL, the observed results do not show a strong preference for the signal-and-background hypothesis, but a slight difference in the observed limit curve and the expected for the background-only hypothesis is visible. L3 has a big discrepancy between the observed limits derived from the number of data events to the expected limits derived for the background-only hypothesis. This discrepancy is based on an excess in data candidates in the direct semi-leptonic channel and direct hadronic channel, which has its maximal effect in the region of $m_{H^\pm}$=68 GeV/c^2 [69, 70].

This effect was investigated by looking at the $1-CL_b$ distributions of the experiments. It is a measure of the incompatibility of the background-only hypothesis with the observed data sample. A very small value would show that the analysis is not in favour of the background-only hypothesis but no statement is made about the nature of a possible signal. Figure 12.2 shows the $1-CL_b$ curve for Br($H^+ \to \tau\nu$)=0.1 against $m_{H^\pm}$ where the excess in L3 reaches its maximum (top diagram). As shown, the L3 results have a probability of $0.5 \cdot 10^{-4}$% (at $m_{H^\pm}$=68 GeV/c^2) to arise from the background alone. Whereas, in combination, the other three experiments show no sign of an excess. The results seen in data have a probability of 25% to arise from background events (lower diagram) and the curve lies well in the 1σ band[1]. The excess in the L3 results is still under investigation.

---

[1] For the conversion $1-CL_b$ into standard deviations (σ), a gaussian approximation is adopted [2, 71] and a *one sided* convention where $1-CL_b = 2.7 \cdot 10^{-3}$ would indicate a 3σ *evidence* and $1-CL_b = 5.7 \cdot 10^{-7}$ a 5σ *discovery*. The median expectation for the background-only hypothesis is 0.5. Values smaller or larger than 0.5 indicate a deficit or excess respectively.

Experiment:	ALEPH	DELPHI	L3	OPAL
Limit exp.(median)/ observed				
for Br($H^+ \to \tau\nu$)=0:	78.4/**81.0**	77.4/**77.8**	77.7/**77.5**	77.8/**76.7**
for Br($H^+ \to \tau\nu$)=1:	86.3/**84.1**	86.5/**85.6**	84.1/**81.9**	89.5/**89.1**
for any Br($H^+ \to \tau\nu$):	77.1/**78.9**	75.6/**76.5**	75.8/**66.5**	76.7/**75.5**

Table 12.2: *Lower mass bounds (in GeV/c^2) of the individual experiments. The observed and median expected numbers with 95% CL are shown. The fractional event counting method was used. No systematic error handling was applied.*

Experiment:	ALEPH	DELPHI	L3	OPAL
Limit exp.(median)/ observed				
for Br($H^+ \to \tau\nu$)=0:	78.1/**80.7**	77.0/**77.4**	77.1/**77.2**	77.1/**76.2**
for Br($H^+ \to \tau\nu$)=1:	86.9/**83.4**	89.3/**85.4**	82.7/**84.6**	86.5/**84.5**
for any Br($H^+ \to \tau\nu$):	76.9/**78.0**	75.4/**73.8**	75.5/**66.9**	74.5/**72.2**

Table 12.3: *Lower mass bounds (in GeV/c^2) of the individual experiments calculated within each collaboration. The observed and median expected numbers with 95% CL are shown. Systematic error handling is applied [6, 67, 68, 69, 70].*

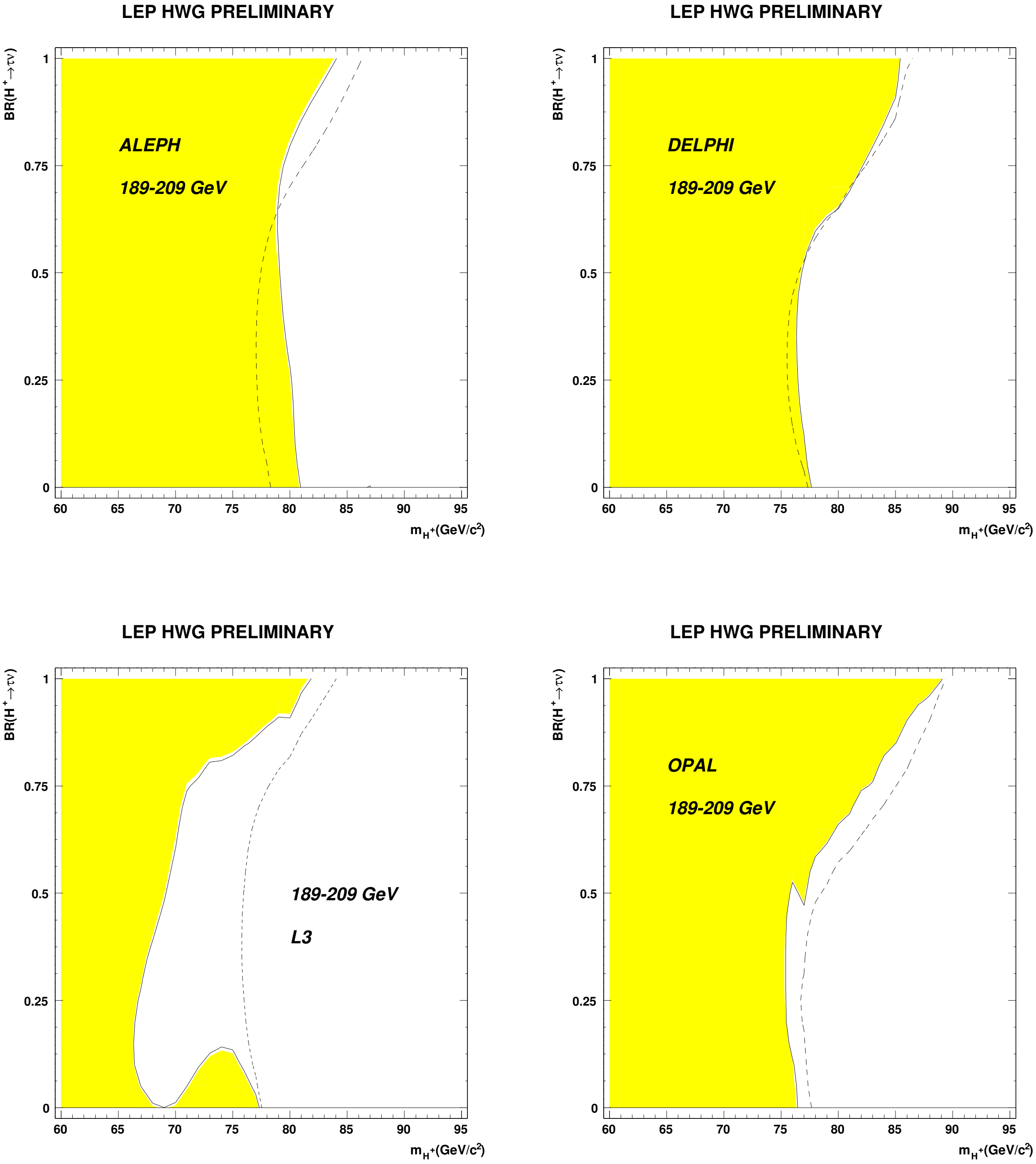

Figure 12.1: *The low mass bounds against $Br(H^+ \to \tau\nu)$ for the four LEP experiments. The fractional event counting method was used. The solid lines (and shaded areas) show the boundaries for the excluded regions at a 95% confidence level. The dashed lines show the median expected at a 95% confidence level. Top left: ALEPH; top right: DELPHI; bottom left: L3; bottom right: OPAL.*

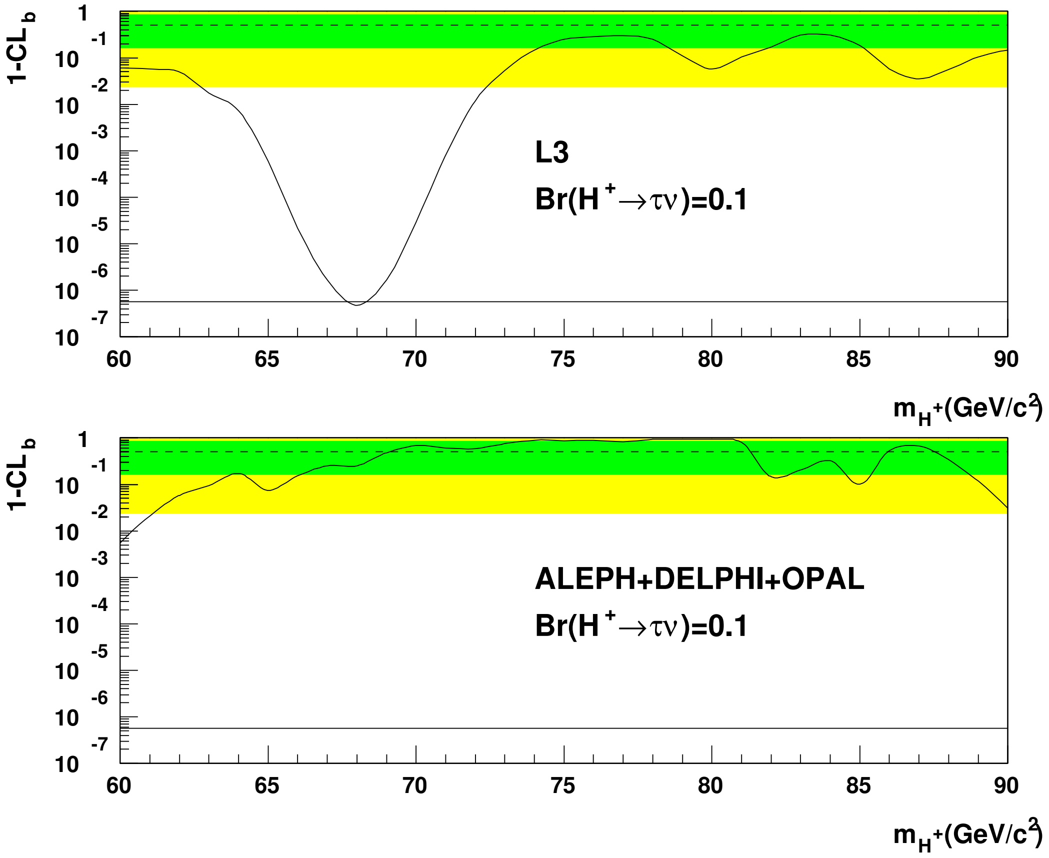

Figure 12.2: *The top: L3 only and bottom: ALEPH+DELPHI+OPAL results at a branching-ratio of Br(*$H^+ \to \tau\nu$*)=0.1. The fractional event counting method was used. The solid lines show* $1 - CL_b$*. The straight horizontal dashed lines at* 50% *and the shaded bands represent the mean and the symmetric 1*σ *and 2*σ *probability bands expected in the absence of a signal. The straight line shows the five* σ *level.*

12.2 The Combination

The LEP combined results for the median expected and observed 95% CL bounds are shown in table 12.4 for Br($H^+ \to \tau\nu$)=0, Br($H^+ \to \tau\nu$)=1 and for the weakest lower mass bound. The excluded region are illustrated in figure 12.3. At low branching-ratios Br($H^+ \to \tau\nu$)≈0 the calculation produces 'islands' around the W-peak ($e^+e^- \to W^+W^-$ background), which poses an irreducible background type for the direct-fermionic decays. The sensitivity is regained at higher charged Higgs masses. The weakest observed charged Higgs mass limit is 79.8 GeV/c^2.

The incompatibility with the background-only hypothesis ($1 - CL_b$) is shown for the LEP combination at Br($H^+ \to \tau\nu$)=0 and Br($H^+ \to \tau\nu$)=1 in figure 12.4. The L3 excess is visible at $m_{\mathrm{H}^\pm} \approx 68$ GeV/c^2. However, in the combination of the results, this mass region is excluded as illustrated in figure 12.3).

Experiment:	LEP mass limits at 95% CL
Limit exp.(median)/ observed	
for Br($H^+ \to \tau\nu$)=0:	88.0/**81.5**
for Br($H^+ \to \tau\nu$)=1:	92.7/**90.4**
for any Br($H^+ \to \tau\nu$):	80.5/**79.8**

Table 12.4: *The combined median expected and observed 95% CL lower mass limits (in GeV/c^2) calculated with the fractional event counting method. The results for fixed values of the branching-ratio Br($H^+ \to \tau\nu$) and for any Br($H^+ \to \tau\nu$) are shown. No systematic error handling is applied.*

The lower mass bound for the LEP combination has also been calculated with the likelihood ratio method [7]. Currently (September 2001) the weakest lower mass bound limit is stated to be 78.6 GeV/c^2 [7]. This shows a difference of 1.2 GeV/c^2 compared to 79.8 GeV/c^2, quoted in table 12.4. Note however, that the result of [7] incorporates a systematic error handling while the one quoted in table 12.4 does not. Investigations of the inclusion of systematic errors with the likelihood ratio method have been made. They can shift the observed mass limits down by up-to 600 MeV/c^2 [7]. Furthermore, for the evaluation of the results quoted in [7] the direct-semi-leptonic channel of OPAL was not included. This is due to an slight excess seen in certain mass regions in this channel. Investigations on this feature are still ongoing.

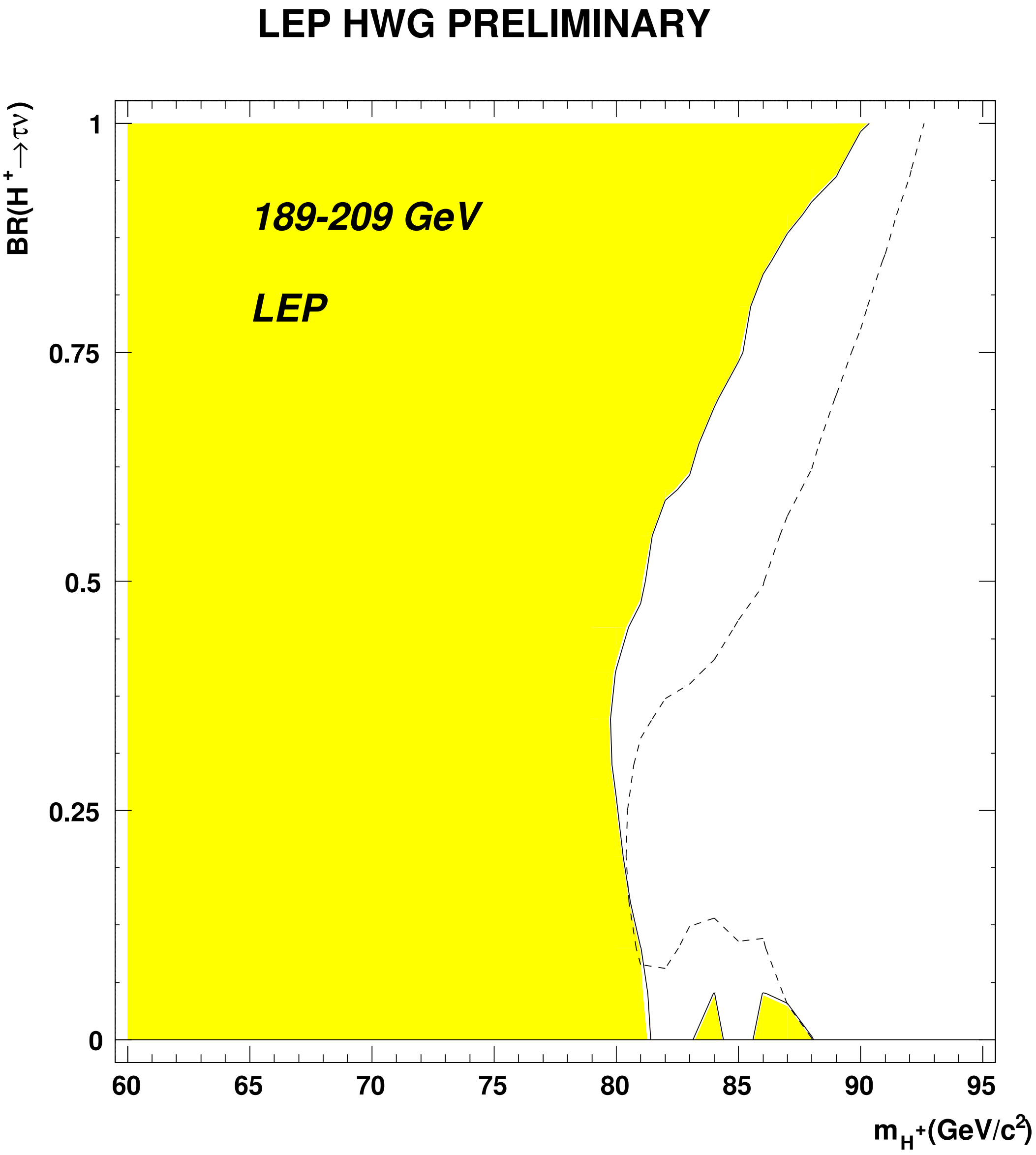

Figure 12.3: *The charged Higgs boson mass limits against the branching-ratio* $Br(H^+ \rightarrow \tau\nu)$ *for the LEP combination. The fractional event counting method was used. The solid lines (and shaded areas) show the boundaries for the excluded regions at a 95% confidence level. The dashed lines show the median expected at a 95% confidence level.*

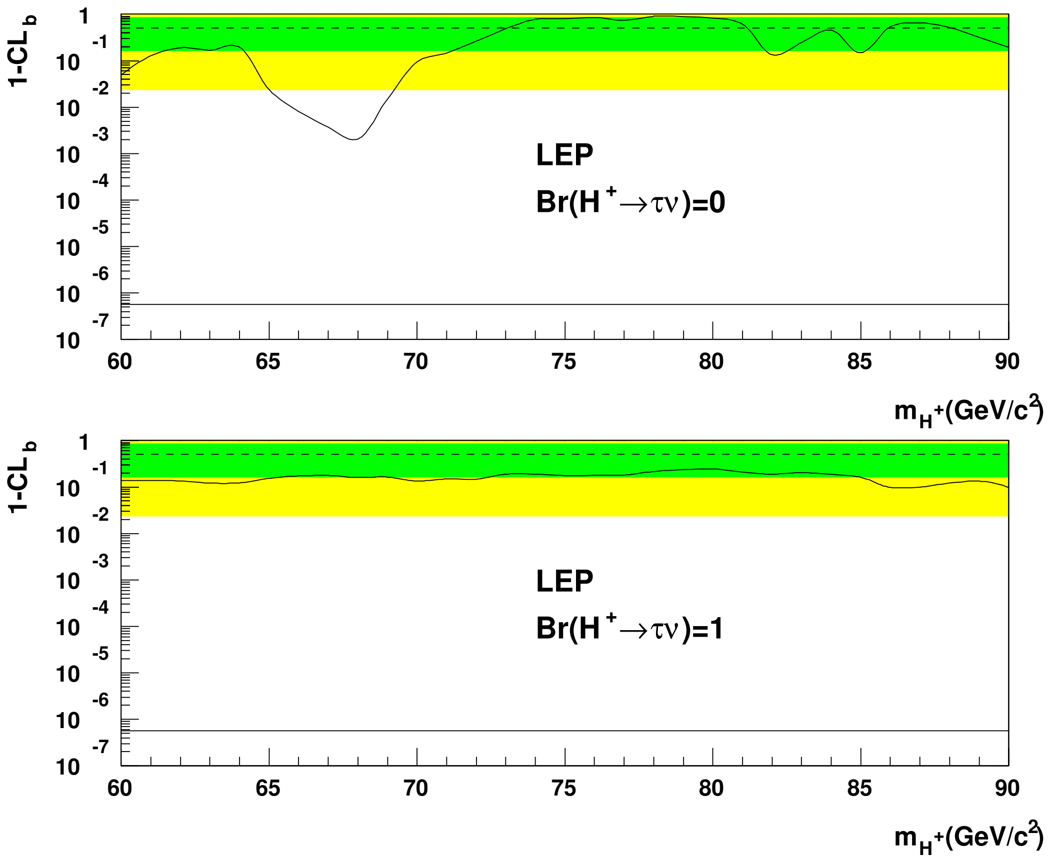

Figure 12.4: *The combined LEP results at top: a branching-ratio Br($H^+ \to \tau\nu$)=0.0 and bottom: branching-ratio of Br($H^+ \to \tau\nu$)=1.0. The fractional event counting method was used. The solid lines show* $1 - CL_b$. *The straight horizontal dashed lines at* 50% *and the shaded bands represent the mean and the symmetric 1σ and 2σ probability bands expected in the absence of a signal. The straight line shows the five σ level.*

Chapter 13

Summary

In this work searches for the charged Higgs boson were presented. No evidence for the existence of the charged Higgs boson at LEP2 energies was found. Bounds are given for the masses of pair-produced charged scalars in a model-independent interpretation. Furthermore, mass bounds are given for charged Higgs bosons in the 2HDM model I and LEP combined mass bounds without the decay $H^{\pm} \rightarrow W^{*}A^{0}$, in the general 2HDM model.

The next possibility to search for charged Higgs bosons is at Fermi National Laboratory in the USA, in $p\bar{p}$ collisions, at future linear $e^{+}e^{-}$colliders or, again at CERN, at the *Large Hadron Collider* (LHC).

Appendix A

Event selection

A.1 OPAL Track Parameters

The z-axis of the OPAL detector is defined by the flight direction of the electrons, the +x direction points to the centre of the LEP ring and the coordinate origin falls together with the center of the detector. The azimuth angle ϕ is defined with respect to the horizontal +x-direction and the polar angle θ with respect to the +z-direction.

The following track parameters are used in the OPAL collaboration:

- $\kappa = \frac{1}{2\rho}$, where ρ is radius of curvature of the track projection in the x-y plane.
- ϕ_0 is the azimuthal angle of the track tangent at the p.c.a.[1]
- d_0 is the track distance from the origin to the p.c.a.
- z_0 is the z-coordinate of the p.c.a.
- $tan(\lambda)=cot(\theta)$ where θ is the polar-angle measured from the positive z-axis.

A.2 On-line Multi-hadronic Event Selection

An event has to fulfil one of the following requirements, (A) or (B), to be accepted by the on-line selection [72, 73, 74]:

- Selection (A)
  There should be at least 5 tracks which fulfil the following quality cuts:
  - The number of hits in the Central Jet Chamber N_{CJhits} $\geq$20; and N_{CJhits} $\geq$50% of the maximum possible number of hits expected from the track geometry.
  - p_T $\geq$0.100 GeV/c; p_T being the momentum transverse to the beam direction
  - $|cos(\theta)|$ $\leq$0.966
  - $|d_0|$ $\leq$2.5 cm
  - $|z_0|$ $\leq$50.0 cm
- Selection (B)
  Following requirements have to be fulfilled
  - The electromagnetic clusters in the barrel (endcap) region should one block with at least 100 (200) MeV with a nearest neighbour of 50 (100) MeV or more.
  - $\sum E_{clusters}$ >8 GeV

---

[1] point-of-closest-approach in the r-ϕ plane.

  - $N_{clusters} \geq 6$
  - $\sum E_{clusters} > 2$ GeV in the hemisphere opposite the highest energy cluster
  - The event should pass the halo rejection cut
  - Number of clusters in the Time-of-flight counter: $N_{TOF} \geq 3$, if $\sum^{barrel} E_{clusters} > 2$ GeV and $N^{barrel}_{clusters} \geq 2$

A.3 Off-line Multi-hadronic Event Selection

The off-line multi-hadronic event selection [72, 73, 74] requires that:
There should be at least 5 tracks with the following properties

- The number of hits in the central detector should fulfil $N_{CD} \geq 20$
- The radius of the first hit along the track: $R_{1sthit} \leq 60.0$ cm
- $|d_0| \leq 2.0$ cm
- $|z_0| \leq 40.0$ cm
- $p_T \geq 0.050$ GeV/c
- $|cos(\theta)| \leq 0.995$
- The χ^2 per degree of freedom of the track in the $r-\phi$-plane: $\chi^2_{r-\phi} \leq 999$
- The χ^2 per degree of freedom of the track in the $s-z$-plane: $\chi^2_{s-z} \leq 999$

where s is the $r-\phi$ path integral from the p.c.a.

There should be at least 7 electromagnetic clusters having

- $E_{raw} \geq 0.100$ GeV in the Barrel or ≥ 0.200 GeV in the endcap
- $N_{blocks} \geq 1$ in the Barrel or ≥ 2 in the endcap

With these tracks and clusters the following variables are computed

- $R_{vis} = \frac{E_{shw}}{2{*}E_{beam}}$
- $R_{bal} = \frac{E_{bal}}{E_{shw}}$

with $E_{shw} = \sum E_{raw}$ and $E_{bal} = \sum E_{raw} * cos(\theta)$, the sum runs over all clusters.

Then, following requirements have to be passed

- $R_{vis} \geq 0.14$
- $|R_{bal}| \leq 0.75$

A.4 Track and Cluster Quality Cuts

The events that pass the on-line and off-line selections are used in the analyses. The following track and cluster definitions are then used in selections [72, 73, 74].

Good tracks must satisfy

- The number of hits in the Central Jet Chamber $N_{CJhits} \geq 20$; and $N_{CJhits} \geq 50\%$ of the maximum possible number of hits expected from the track geometry.
- $p_T \geq 0.120$ GeV/c; p_T being the momentum transverse to the beam direction.
- $p \cdot c < E_{beam} \cdot (1 + 6.0 \cdot \sqrt{0.02^2 + (0.0015 \cdot E_{beam}/GeV)^2})$, where E_{beam} is the beam energy
- $|d_0| \leq 2.0$ cm
- $|z_0| \leq 40.0$ cm
- $|cos(\theta)| \leq 0.9622$

Good clusters in the electromagnetic calorimeter have to satisfy

- The number of blocks in the barrel (endcap) region must be greater or equal 1 (2)
- The raw energy (uncorrected) E_{raw} of the clusters should be greater or equal to 100 (250) MeV in the barrel (endcap) region.

Good clusters in the hadronic calorimeter have to satisfy

- The energy measured in the towers $E_{towers} \geq 0.6$ GeV in barrel and endcap and $E_{towers} \geq 2.0$ GeV in the poletip

Good clusters in the forward region are defined as

- $E_{FD} \geq 1.5$ GeV in the forward calorimeter
- $E_{GC} \geq 5.0$ GeV in the gamma catcher
- $E_{SW} \geq 0.5$ GeV in the silicon tungsten luminometer

Bibliography

[1] O. Nachtmann, *Elementarteilchenphysik*, Vieweg, 1986.

[2] The ALEPH, DELPHI, L3 and OPAL Collaborations,
Search for the Standard Model Higgs Boson at LEP, OPAL **PN 479**, 2001.

[3] J.F. Gunion, H.E. Haber, G.L. Kane, and S. Dawson, *The Higgs Hunter's Guide*, Addison-Wesley, Reading, 1990.

[4] A. G. Akeroyd, Nucl. Phys. **B544**, 557 (1999).

[5] M. Carena *et al.*, CERN 96-01 **1**, 351 (1996).

[6] OPAL Collaboration, OPAL **PN 472** (2001).

[7] The ALEPH, DELPHI, L3 and OPAL Collaborations,
Search for Charged Higgs bosons: Preliminary Combined Results Using LEP data Collected at Energies up to 209 GeV, OPAL **TN 696**, 2001.

[8] OPAL Collaboration, OPAL **PN 445** (2000).

[9] D. Haidt and P.M. Zerwas *et al.*, Eur. Phys. J. **C3**, 1 (1998).

[10] S.Glashow, and S. Weinberg, Phys. Rev. **D15**, 1958 (1977).

[11] CLEO Collaboration, M. S. Alam *et al.*, Phys. Rev. Lett. **74**, 2885 (1995).

[12] ALEPH Collaboration, R. Barate *et al.*, Phys. Lett. **B429**, 169 (1998).

[13] M. Ciuchini, G. Degrassi, P. Gambino, and G. F. Giudice, Nucl. Phys. **B534**, 3 (1998).

[14] A. G. Akeroyd and W. J. Stirling, Nucl. Phys. **B447**, 3 (1995).

[15] A. Djouadi, J. Kalinowski and P. M. Zerwas, Z. Phys. **C70**, 435 (1996).

[16] The ALEPH, DELPHI, L3 and OPAL Collaborations,
Searches for the Neutral higgs Bosons of the MSSM: Preliminary Combined Results Using LEP Data Collected at Energies up to 209 GeV, OPAL **TN 699**, 2001.

[17] branching fractions provided by A. G. Akeroyd and A. Arhrib.

[18] A. G. Akeroyd, private communication.

[19] OPAL Collaboration, K. Ahmet *et al.*, Nucl. Instrum. Meth. **A305**, 275 (1991).

[20] OPAL Collaboration, S. Anderson *et al.*, Nucl. Instrum. Meth. **A403**, 326 (1998).

[21] OPAL Collaboration, G. Agullion *et al.*, Nucl. Instrum. Meth. **A417**, 266 (1998).

[22] OPAL Collaboration, B. E. Anderson *et al.*, IEEE Trans. Nucl. Sci. **41**, 845 (1994).

[23] OPAL Collaboration, J. Allison *et al.*, Nucl. Instrum. Meth. **A317**, 47 (1992).

[24] R. Run *et al.,* , CERN DD **78-2** (1978).

[25] T. Sjostrand, Comput. Phys. Commun. **82**, 74 (1994).

[26] G. Marchesini *et al.*, Comput. Phys. Commun. **67**, 465 (1992).

[27] J. Fujimoto *et al.*, Comput. Phys. Commun. **100**, 128 (1997).

[28] Minami-Tateya collaboration, KEK Report **92-19** (1993).

[29] F. A. Berends, R. Pittau and R. Kleiss, Comput. Phys. Commun. **85**, 437 (1995).

[30] S. Jadach, B.F.L. Ward and Z. Was, Comput. Phys. Commun. **130**, 260 (2000).

[31] S. Jadach, B.F.L. Ward, and Z. Was, Phys. Rev. **D63**, 113009 (2001).

[32] R. Engel and J. Ranft, Phys. Rev. **D54**, 4244 (1996).

[33] S. Jadach, B. F. L. Ward and Z. Was, Comput. Phys. Commun. **124**, 233 (2000).

[34] J. A. M. Vermaseren, Nucl. Phys. **B229**, 347 (1983).

[35] P. Janot, CERN 96-01 **2**, 309 (1996).

[36] OPAL Collaboration, G. Abbiendi *et al.*, Eur. Phys. J. **C18**, 447 (2001).

[37] S. Mihara and S. Yamashita, OPAL TN **575** (1998).

[38] N. Brown and W.J. Stirling, Phys. Lett. **B252**, 657 (1990).

[39] S. Bethke, Z. Kunszt, D. Soper and W.J. Stirling, Nucl. Phys. **B370**, 310 (1992).

[40] S. Catani *et al*, Phys. Lett. **B269**, 432 (1991).

[41] N. Brown and W.J. Stirling, Z. Phys. **C53**, 629 (1992).

[42] K. Ishii and S. Yamashita, OPAL TN **577** (1998).

[43] A. G. Froedesen *et al.*, *Probability and Statistics in Particle Physics*, Bergen Universitetsforlaget, Oslo, 1979.

[44] G. Pasztor, *Search for Charged Higgs Bosons and Supersymmetric Particle*, PhD thesis, Eotvos University Budapest, 1999.

[45] D. Glenzinski and A. Hocker, OPAL TN **559** (1998).

[46] OPAL Collaboration, G. Abbiendi *et al.*, Eur. Phys. J. **C7**, 407 (1999).

[47] OPAL Collaboration, G. Abbiendi *et al.*, Eur. Phys. J. **C12**, 567 (2000).

[48] S. Yamashita, I. Nakamura, OPAL TN **578** (1998).

[49] S. Yamashita, I. Nakamura, OPAL TN **576** (1998).

[50] OPAL Collaboration, G. Abbiendi *et al.*, Phys. Lett. **B499**, 38 (2001).

[51] The OPAL Collaboration, G. Alexander *et al.*, Phys. Lett. **B376**, 232 (1996).

[52] G. Parisi, Phys. Lett. **B74**, 65 (1978).

[53] J.F. Donoghue, F.E. Low, and S.Y. Pi, Phys. Rev. **D20**, 2759 (1995).

[54] A. A. Faust, OPAL TN **582** (1998).

[55] C. Bishop *et al.*, *Neural Networks for Pattern Recognition*, Oxford University Press, 1995.

[56] R. J. Barlow, *Statistics*, Wiley, 1999.

[57] D. Karlen, OPAL TN **459** (1997).

[58] D. Karlen, OPAL TN **483** (1997).

[59] Private communications, *Talk given by Kara Hoffman: Search for* $H^+ \to W^+A^0$, OPAL collaboration week, March 2000.

[60] ALEPH, DELPHI, L3 OPAL Collaborations and the LEP Electroweak Working Group and the SLD Heavy Flavour and Electroweak Groups, *A Combination of Preliminary Electroweak Measurements and Constraints on the Standard Model*, CERN-EP-2000-016, 2000, and references therein.

[61] P. Bock, *Determination of exclusion limits for particle production using different decay channels with different efficiencies, mass resolutions and backgrounds*,
to be submitted to Nucl. Instrum. Meth., 1997.

[62] P. Bock, private communication
CONFL10: A statistics program to compute confidence levels for exclusion or discovery of a signal over background, 2001.

[63] editor F. James *et al.*,*Workshop on Confidence Limits*, **CERN-2000-005**, 2000.

[64] The ALEPH, DELPHI, L3 and OPAL Collaborations,
Searches for Higgs bosons: preliminary combined results from the four LEP experiments at $\sqrt{s} \approx 189$ *GeV*, **CERN-OPEN-99-377**, 1999.

[65] The ALEPH, DELPHI, L3 and OPAL Collaborations,
Searches for Higgs bosons: Preliminary combined results using LEP data collected at energies up to 202 GeV , **CERN-EP-2000-055**, 2000.

[66] R. D. Cousins and V. L. Highland, Nucl. Instrum. Meth. **A320**, 331 (1992).

[67] ALEPH Collaboration, ALEPH **2001-016** (2001).

[68] DELPHI Collaboration, DELPHI **2001-030** (2001).

[69] L3 Collaboration, L3 **note 2686** (2001).

[70] L3 Collaboration, Phys. Lett. **B496**, 34 (2000).

[71] D. E. Groom, Eur. Phys. J. **C15**, 1 (2000).

[72] OPAL Collaboration, K. Ackerstaff *et al.*, Eur. Phys. J. **C2**, 441 (1998).

[73] OPAL Collaboration, G. Alexander *et al.*, Z. Phys. **C52**, 175 (1991).

[74] OPAL Collaboration, G. Abbiendi *et al.*, Nucl. Instrum. Meth. **A313**, 103 (1992).

Acknowledgements

I wish to thank everybody who supported me during the time of my thesis.

I would especially like to thank Prof. J. von Krogh and Prof. P. Bock for making this thesis possible, for their support, discussions and helpful advice. In particular I would like to thank Prof. P. Bock. for being able to call him at 7 am in the morning for help, if in need of it and Prof. J. von Krogh for is tremendous support in the very last days of my thesis. I would also like to thank Prof. O. Nachtmann for being my second referee.

I would like to thank Kara Hoffman who worked together with me on the analyses at $\sqrt{s}$ =189 GeV and who was the first to investigate these decay channels. I learned a lot from her.

Another word of thanks goes to the OPAL Higgs working group, especially Tom Junk and Satoru Yamashita, the LEP Higgs working group and everybody at OPAL for a wonderful time at CERN.

I would also like to thank Helge Voss, Daniel Güllich and Manuela Magin for their friendship, help and just for being very special friends.

And last but not least, a very sincere thanks goes to Dirk Wetterling. He encouraged and supported me in private and in working life.